

IMAGING SPIN TEXTURES ON CURVED MAGNETIC SURFACES

von der Fakultät für Naturwissenschaften der
Technischen Universität Chemnitz
genehmigte Dissertation zur Erlangung des akademischen Grades

doctor rerum naturalium

(Dr. rer. nat.)

vorgelegt von DIPLOM-PHYSIKER ROBERT STREUBEL
geboren am 5. Oktober 1987 in Dippoldiswalde

Eingereicht am 8.5.2015

Gutachter:

Prof. Dr. Oliver G. Schmidt

Adj.-Prof. Dr. Peter Fischer

Tag der Verteidigung: 27.8.2015

<http://nbn-resolving.de/urn:nbn:de:bsz:ch1-qucosa-178266>

To my parents

Robert Streubel

Imaging Spin Textures on Curved Magnetic Surfaces

Dissertation (in englischer Sprache)

165 Seiten, 53 Abbildungen, 3 Tabellen, 282 Literaturverweise

Keywords: 3D curved surfaces, magnetism, magnetic imaging, XMCD, XPEEM, MTXM, magnetic soft X-ray tomography, rolled-up nanotech, strain engineering

Kurzfassung

Gegenwärtige Bestrebungen materialwissenschaftlicher Forschung beschäftigen sich unter anderem mit der Überführung zweidimensionaler Elemente elektronischer, optischer, plasmonischer oder magnetischer Funktionalität in den dreidimensionalen (3D) Raum. Dieser Ansatz vermag mittels Krümmung und struktureller Topologie bereits vorhandene Eigenschaften abzuändern beziehungsweise neue Funktionalitäten bereitzustellen. Vor allem Vektoreigenschaften wie die Magnetisierung kondensierter Materie lassen sich aufgrund der Brechung der Inversionssymmetrie in gekrümmten Flächen stark beeinflussen. Neben der Entwicklung diverser Vorgänge zur Herstellung 3D magnetischer Gegenstände sind geeignete Untersuchungsmethoden wie beispielsweise tomografische Abbildungen der Magnetisierung von Nöten, die maßgeblich die physikalischen Eigenschaften bestimmen.

Die vorliegende Dissertationsschrift befasst sich mit der Abbildung von magnetischen Domänen in 3D gekrümmten Dünnschichten beruhend auf dem Effekt des zirkularen magnetischen Röntgendichroismus (XMCD). Die in diesem Zusammenhang entwickelte *magnetische Röntgentomografie (MXT)* basierend auf weicher Röntgenmikroskopie stellt eine zu Elektronenholografie und Neutronentomografie komplementäre Methodik dar, welche großes Anwendungspotential in der elementspezifischen Untersuchung magnetischer gekrümmter Flächen mit örtlicher Auflösung im Nanometerbereich aufweist. Die Schwierigkeit der Interpretation von Abbildungen magnetischer Strukturen in gekrümmten Flächen rührt von der Dreidimensionalität und der Vektoreigenschaft der Magnetisierung her. Die hierzu notwendigen Kenntnisse sind anhand von zwei topologisch verschiedenen Flächen in Form hemisphärischer Kappen und hohler Zylinder erschlossen worden. Die praktische Anwendung von MXT ist abschließend anhand der Rekonstruktion magnetischer Domänen in aufgerollten Dünnschichten mit zylindrischer Form verdeutlicht.

Abstract

One of the foci of modern materials sciences is set on expanding conventional two-dimensional electronic, photonic, plasmonic and magnetic devices into the third dimension. This approach provides means to modify conventional or to launch novel functionalities by tailoring curvature and three-dimensional (3D) shape. The degree of effect is particularly high for vector properties like the magnetization due to an emergent inversion symmetry breaking. Aside from capabilities to design and synthesize 3D magnetic architectures, proper characterization methods, such as magnetic tomographic imaging techniques, need to be developed to obtain a thorough understanding of the system's response under external stimuli.

The main objective of this thesis is to develop a visualization technique that provides nanometer spatial resolution to image the peculiarities of the magnetic domain patterns on extended 3D curved surfaces. The proposed and realized concept of *magnetic soft X-ray tomography (MXT)*, based on the X-ray magnetic circular dichroism (XMCD) effect with soft X-ray microscopies, has the potential to become a powerful tool to investigate element specifically an entirely new class of 3D magnetic objects with virtually any shape and magnetization. Imaging curved surfaces meets the challenge of three-dimensionality and requires a profound understanding of the recorded XMCD contrast. These experiences are gained by visualizing magnetic domain patterns on two distinct 3D curved surfaces, namely magnetic cap structures and rolled-up magnetic nanomembranes with cylindrical shape. The capability of MXT is demonstrated by reconstructing the magnetic domain patterns on 3D curved surfaces resembling hollow cylindrical objects.

Contents

1. Introduction	1
2. Scientific Background	5
2.1. Magnetism and Magnetic Energies	5
2.2. Magnetism on Curved Surfaces	8
2.2.1. Curvature-Driven Modifications	8
2.2.2. Magnetic Hemispherical Caps and Spherical Shells	10
2.2.3. Magnetic Cylindrical Surfaces	14
2.3. Tomographic Imaging	18
2.3.1. Magnetic Neutron Tomography	21
2.3.2. Electron-based 3D Imaging	22
3. Fabrication Methods	27
3.1. Deposition onto Curvature Template	27
3.1.1. Hemispherical Cap Structures	27
3.1.2. Non-Planar Honeycomb Lattice	29
3.2. Rolled-up Nanotech	29
3.2.1. Epitaxial Strained Films	30
3.2.2. Polycrystalline Strained Films	32
4. Characterization Methods	37
4.1. Kerr Microscopy	37
4.2. Magnetic Force Microscopy	38
4.3. Magnetic Soft X-ray Microscopy	39
4.3.1. X-ray Magnetic Circular Dichroism	41
4.3.2. Transmission Soft X-ray Microscopy	42
4.3.3. X-ray Photoemission Electron Microscopy	45
4.3.4. Transmission X-ray Photoemission Electron Microscopy	46

4.4. Magnetic Soft X-ray Tomography	48
5. Magnetic Cap Structures	51
5.1. Hemispherical Permalloy Caps	51
5.1.1. Imaging Magnetic Remanent States	52
5.1.2. Magnetization Reversal	57
5.2. Imprinted Non-Collinear Spin Textures in Hemispherical Caps	61
5.2.1. Theoretical Predictions	62
5.2.2. Experimental Observation	64
5.3. Cylindrical Permalloy Caps	68
5.3.1. Magnetization Reversal Process	69
5.3.2. Magnetic Remanent States	69
5.4. Magnetic Cap Structures in Life Sciences	72
5.5. Conclusion	73
6. Cylindrical Magnetic Architectures	75
6.1. Tailoring Magnetic Domain Patterns	75
6.1.1. Magnetic Hysteresis Loops	76
6.1.2. Magnetic Domains	78
6.1.3. Magnetoresistance Measurements	80
6.2. Imaging Inner Magnetization Textures	81
6.2.1. Tightly Wound Rolled-up Nanomembranes	82
6.2.2. Loosely Wound Rolled-up Nanomembranes	83
6.3. Conclusion	85
7. 3D Imaging of Tubular Magnetic Architectures	87
7.1. Circulating Magnetization Patterns	87
7.2. Radially Magnetized Tubular Architectures	92
7.2.1. Reconstruction Algorithm	94
7.2.2. Reconstruction of Radial Magnetization Patterns	95
7.3. Generalization of the Reconstruction Algorithm	99
7.4. Conclusion	100
8. Conclusion & Outlook	101
8.1. Conclusion	101
8.2. Outlook	103
A. Appendix	107

A.1. Versatility of Cross-Beam Workstation	107
A.2. Lithographical Patterning	108
Bibliography	111
List of Figures	139
List of Tables	143
Curriculum Vitae	149
Publications	151

Acronyms and Symbols

Acronyms

2D	two-dimensional
3D	three-dimensional
<i>ac</i>	alternating current
ALS	Advanced Light Source
AMR	anisotropic magnetoresistance
BESSY	Berliner Elektronenspeicherring-Gesellschaft für Synchrotronstrahlung
BSE	back-scattered electrons
CPD	critical point dryer
CZP	condensor zone plate
<i>dc</i>	direct current
DMI	Dzyaloshinskii-Moriya interaction
e-beam	electron beam
EBVD	electron beam vapor deposition
FIB	focused ion beam
FMR	ferromagnetic resonance spectroscopy
MBE	molecular beam epitaxy
MFM	magnetic force microscopy
ML	monolayer
MOKE	magneto-optical Kerr effect
MR	magnetoresistance
MTXM	magnetic transmission soft X-ray microscopy
MXT	magnetic soft X-ray tomography
MZP	micro zone plate
PEEM	photoemission electron microscopy

PS	polystyrene
rpm	rounds per minute
SE	secondary electrons
SEM	scanning electron microscopy
SNR	signal-to-noise ratio
SQUID	superconducting quantum interference device
T-XPEEM	transmission X-ray photoemission electron microscopy
XMCD	X-ray magnetic circular dichroism
XPEEM	X-ray photoemission electron microscopy

Symbols

α	projection/ rotation angle
\emptyset	diameter
ε	lateral strain
φ	phase shift
δ	rotation angle
μ_{\pm}	X-ray absorption coefficient
a	lattice constant
A	Heisenberg exchange constant
\mathbf{B}	magnetic induction
d	thickness
E	kinetic energy
\mathbf{H}	magnetic field
J_i	interlayer exchange coupling
K	magnetic anisotropy
\mathbf{k}	X-ray beam propagation direction
M_s	saturation magnetization
\mathbf{M}	magnetization
\mathbf{m}	magnetization normalized by M_s
\mathbf{n}	surface normal
Py	Permalloy ($\text{Ni}_{80}\text{Fe}_{20}$)
R	radius
T	temperature

1. Introduction

From Stones to Curved Surfaces

Ever since the discovery of inherent forces in magnetic stones (magnetite, Fe_3O_4 ; also 磁石, loving stone) by ancient Greek and Chinese (600 b.c.), magnetism has fascinated humanity. This intrigue ended up in the assignment of a living soul (Thales) or even god (Plato). A proper scientific explanation of magnetism was given by quantum theory in the early 20th century, describing atoms as nuclei that are surrounded by charged electrons in orbitals with discrete energies. These elementary particles possess quantized magnetic moments (spins) that usually arrange antiparallel with absent net magnetization. In certain materials, such as transition metals and rare-earth compounds, anisotropic d and f valence orbitals prefer one electron spin over the other due to spin-orbital interaction. The particular magnetization configuration is determined by the relative orientation of and the distance between electron orbitals of adjacent atoms through spin exchange. Common Heisenberg exchange favoring collinear alignment may be accompanied by an antisymmetric vector exchange, known as Dzyaloshinskii-Moriya interaction (DMI) [1, 2], which stabilizes non-collinear spin textures in non-centrosymmetric media [3–8]. These magnetization configurations are characterized by small feature sizes (< 100 nm) and high stability against external perturbations [9, 10], which makes them attractive for applications as magnetic storage (shift registers) [11, 12] and logic devices [13].

Advances in nanotechnology and thin film deposition have enabled high-quality film fabrication, offering the possibility to investigate coupling phenomena in layer stacks through spacers with large spin-orbital interaction, such as Ru, Pd or Pt, *via* RKKY [14–16] or interfaces *via e.g.* surface DMI [17–19]. While RKKY-induced antiferromagnetically coupled multilayer stacks are the basis of the prominent giant magnetoresistance (GMR) effect [20, 21] exploited in conventional magnetic hard drives, DMI-driven chirality selection of Néel walls [22–27] is an essential ingredient for coherent domain wall motion triggered by

current pulses and future magnetic storage devices. The lack of an inversion symmetry and the emergence of a corresponding DMI are also provided in bent and curved surfaces [28, 29], which potentially offer various topologies, including spheres, hollow cylinders, spirals and Möbius bands. These magnetic films possess striking properties originating from curvature-driven magnetochiral effects [30–36] and topologically induced magnetization patterns [34, 37], including unlimited domain wall velocities [38], chirality symmetry breaking [32, 33], Cherenkov-like effects for magnons [31, 35] and magnetoelectricity by toroidal magnetic moments [39].

The realization of those magnetic curved surfaces requires to advance current or to develop new approaches for fabrication and characterization. Chemical approaches relying on isotropic wetting in vapor or liquid phases imply the crystallization of many grains with a substantial surface roughness [40–44], which is particularly disadvantageous for magnetic materials due to strong pinning on defects. On the contrary, physical deposition provides high-quality layers with minimal surface roughness. The limitation to planar and curved objects with thickness gradients due to directed deposition can be overcome by engineering strain gradients [45, 46] in the deposited layers that relax upon rolling [47, 48] or wrinkling [49, 50] after selective release from the substrate.

Characterization

In contrast to planar architectures where each sample area can be observed using "top-view" microscopy, 3D curved surfaces hide substantial parts of their structure. Structural and magnetic properties may only be revealed with tomographic imaging using the information drawn from precharacterization investigations as input. In this respect, integral measurements exploiting electric current flowing through the object (magnetoresistance) or stray fields of the structure (magnetometry) are well suited to determine characteristics of the entire sample, *e.g.* preferential magnetization orientation and switching fields. State-of-the-art magnetic tomographic imaging techniques, such as magnetic neutron tomography [51, 52], electron holography [53–56] and vector field electron tomography (VFET) [57, 58], rely on the detection of the phase shift originating from interaction with magnetic fields. While magnetic neutron tomography is applied to determine the spatial distribution of magnetic domain walls in macroscopic bulky materials, electron holography and VFET allow for reconstructing magnetization vectors in nanoscopic samples with nanometer spatial resolution. As sizeable curvature-driven effects demand a film thickness of few nanometers,

magnetic neutron tomography cannot be applied. At the same time, lateral dimensions of mesoscopic sample and radii of curvature make it challenging to employ electron holography or VFET.

On the other hand, utilizing X-ray magnetic circular dichroism (XMCD) as element-specific contrast mechanism with full-field X-ray microscopies provides nanometer spatial resolution to image the peculiarities of the magnetic domain patterns on 3D curved surfaces extended over tens of micrometer. X-ray tomography is an established technique to reconstruct the 3D distributions of atomic densities in a vast of different 3D objects [51, 59–64]. Yet, *magnetic X-ray tomography (MXT)* [65] offering the possibility to reconstruct magnetization spin textures in 3D-shaped mesoscopic objects had been to be developed.

Aim and Structure of this Thesis

The scope of this thesis is to develop MXT by advancing current magnetic X-ray microscopies utilizing XMCD and to retrieve the magnetization configurations on 3D curved magnetic surfaces. Hemispherical caps and rolled-up nanomembranes resembling hollow cylinders and spirals, are chosen as representative examples of curved objects with one, two and multiple surfaces, respectively. Analyzing the XMCD contrast of these objects reveals modifications to the magnetic contrast and allows to accumulate a profound understanding of the XMCD contrast origin on 3D curved surfaces. To this end, the magnetic domain patterns on cylindrical surfaces are reconstructed with MXT. The thesis is organized as follows.

The work is put into context with state-of-the-art research activities on non-planar magnetic architectures and 3D imaging techniques (Chapter 2).

After providing insight into the fabrication methods used throughout this thesis (Chapter 3), a brief introduction to the most relevant characterization techniques with focus on emergent challenges when applied to curved magnetic surfaces is given in Chapter 4.

A first experimental study of the impact of a 3D shape on the magnetic properties and XMCD contrast is presented for hemispherical caps in Chapter 5. When illuminating a curved surface at a shallow angle in transmission microscopy a shadow contrast at the back side of the magnetic cap is observed providing means to image buried magnetic layers.

The inner magnetization texture of tightly and loosely wound rolled-up nanomembranes is imaged by recording the 2D projection of the XMCD contrast in the shadow (Chapter 6). The accumulated knowledge on the XMCD contrast interpretation in the cylindrical objects is basis of developing MXT.

In Chapter 7, the 3D spatial distribution of the magnetization in cylindrical architectures is retrieved by analyzing the evolution of the magnetic contrast with varying projection angle. Applying MXT with nanometer spatial resolution and magnetization sensitivity, remanent states of circulating and radial magnetization textures with feature sizes down to 75 nm are reconstructed. The corresponding remanent states in the 3D curved surfaces exhibit a strong dependence on both number of windings and surface angle with respect to the initially applied magnetic field.

The thesis concludes with summarizing the most relevant aspects and outlining current and future topics in view of potential applications (Chapter 8).

2. Scientific Background

This Chapter reviews the appealing fundamental properties of 3D surfaces originating from the curvature, namely magnetochiral effects and curvature-induced topological patterning. Modifications in spherical and tubular objects as well as their experimental realization are discussed in detail. An overview on current state-of-the-art characterization techniques to access the magnetization in 3D objects is given.

2.1. Magnetism and Magnetic Energies

Magnetism refers to physical phenomena associated with magnetic moments of elementary particles, such as electrons. In condensed matter, these magnetic moments (spins) arrange in a certain manner originating from a hybridization of the electron orbitals of the atoms and the Pauli exclusion principle for Fermions. The simplest hybridization of two hydrogen atoms leads to singlet and triplet states with antiparallel and parallel electron spin orientation, respectively [66]. While the helium atom does not possess a magnetic moment in the ground state, it can be excited into magnetic triplet states. Similarly, most materials do not exhibit a magnetic moment at remanence but show a paramagnetic or diamagnetic behavior upon exposure to an external magnetic field.

The origin of an ordered electron spin lattice in condensed matter is the hybridization of anisotropic d and f electron orbitals with an emergent spin-orbital interaction. The preferential magnetization textures with ferromagnetic (transition metals), ferrimagnetic (oxides, rare-earth compounds), antiferromagnetic (oxides) or helimagnetic (non-centrosymmetric compounds) arrangements [Fig. 2.1(a)] depend on the peculiar magnetic energies, including exchange, anisotropy and magnetostatic contributions. The exchange coupling between nearest electron spins \mathbf{S}_j at the j -th lattice point is described by the symmetric Heisenberg

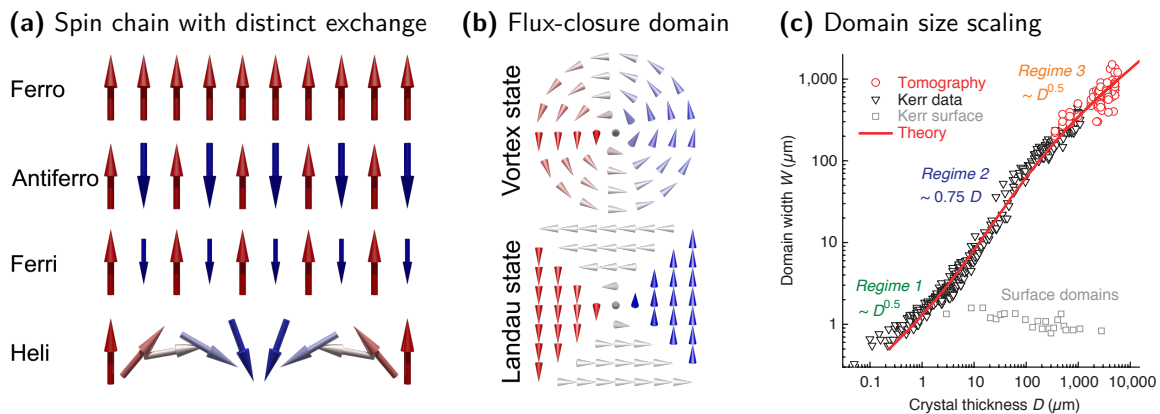


Fig. 2.1.: (a) Magnetic spin arrangements in ferromagnets, antiferromagnets, ferrimagnets and helimagnets with distinct exchange coupling. The latter configuration requires a vector exchange. (b) Flux-closure domains in soft-magnetic micropatterns with minimized stray field contributions. (c) Scaling of volume domain to reduce exchange contributions from domain walls in the bulk. Size of surface domains remain the same. (Taken from (c): [52])

term $-\sum_{(ij)} J_{ij} \mathbf{S}_i \mathbf{S}_j$ [67] and the antisymmetric Dzyaloshinskii-Moriya interaction (DMI) term $\sum_{(ij)} D_{ij} \mathbf{S}_i \times \mathbf{S}_j$ [1, 2], favoring collinear, such as ferromagnetic, ferrimagnetic and antiferromagnetic, and non-collinear, including weak ferromagnetic, helimagnetic and chiral, spin textures, respectively [Fig. 2.1(a)]. The macroscopic manifestation of the exchange energy density \mathcal{E}_{ex} reads in the framework of continuum theory [67, 68]:

$$\mathcal{E}_{ex} = A (\nabla m_i)^2 + D_{ijk} m_j \nabla_k m_i, \quad (2.1)$$

with the normalized magnetization \mathbf{m} , the exchange constant A and the antisymmetric DMI tensor D_{ijk} . The inversion symmetry breaking of the unit cell required to provide DMI is absent in most magnetic materials. Evidence of an emergent DMI has been given in single-phase materials with acentric crystal structures [3–8] or in magnetic films owing to broken inversion symmetry [17–19, 69]. The great interest into such non-collinear spin textures relies on their inertia against external stimuli and small feature sizes [9, 10] that may potentially serve as magnetic shift registers [11, 12] and magnetic logic devices [13].

While exchange interaction determines the relative orientation of adjacent spins, magnetic anisotropy determines the magnetic easy axes or planes, which refer to the preferential magnetization orientation with respect to the arrangement of atoms. Anisotropy contributions are prominent in crystals, magnetostrictive materials and out-of-plane magnetized films due to an overlap or distortion of electron orbitals [67]. In this respect, the anisotropy energy increases as the magnetization tilts away from the easy axis/ plane. Mathematic-

ally this is treated as a perturbation of spherical harmonics up to the second order in the magnetization [67, 70]:

$$\mathcal{E}_{aniso} = \lambda_j (\mathbf{m}\mathbf{n}_j)^2, \quad (2.2)$$

with the normalized anisotropy coefficients λ_j ($\lambda_j > 0$: easy-plane perpendicular to \mathbf{n} , $\lambda_j < 0$: easy-axis along \mathbf{n}).

In addition to those intrinsic properties, magnetic stray field contributions, originating from *i.e.* demagnetization fields, strongly depend on shape and saturation magnetization of the object. According to the Maxwell equation $\nabla \mathbf{B} = \mu_0 \nabla (\mathbf{H}_d + \mathbf{M}) = 0$ for the magnetic induction \mathbf{B} , each source and sink of the magnetization \mathbf{M} causes a stray field $\mathbf{H}_d = -\nabla \phi$ with a corresponding demagnetization energy $E_d = -\frac{\mu_0}{2} \int \mathbf{H}_d \mathbf{M} d^3r$ [67]:

$$\left. \begin{aligned} \phi &= \frac{1}{4\pi} \left(\int \frac{\rho(\mathbf{r}')}{|\mathbf{r} - \mathbf{r}'|} d^3r' + \oint \frac{\sigma(\mathbf{r}')}{|\mathbf{r} - \mathbf{r}'|} df' \right), \\ E_d &= \frac{\mu_0}{2} \left(\int \rho \phi d^3r + \oint \sigma \phi df \right). \end{aligned} \right\} \quad (2.3)$$

The integrations are taken over the sample volume and surface, respectively. Thus, the magnetic ground state with an energy minimum is characterized by minimized contributions of magnetostatic volume divergence $\rho = -\nabla \cdot \mathbf{M}$ and surface charge $\sigma = \mathbf{M} \cdot \mathbf{n}$ with the surface normal \mathbf{n} .

Minimizing exchange, anisotropy and demagnetization energy leads to size-dependent magnetic equilibrium states. Nanoscopic objects with dimensions smaller than ≈ 200 nm remain in uniformly magnetized (singledomain) state [67] due to large surface-to-volume ratio and a leading anisotropy contribution. The domain patterns in larger samples depend on the interplay between the magnetic energy contributions. Soft-magnetic materials like Permalloy (Py, $\text{Ni}_{80}\text{Fe}_{20}$) with vanishing anisotropy exhibit in structurally confined patterns flux-closure domains, such as vortex and Landau states [Fig. 2.1(b)] [71–73], and random almost uniformly magnetized patterns with in-plane magnetization otherwise. An unfavored normal magnetization can be set in multilayer stacks with out-of-plane magnetic anisotropy [74–76] originating from RKKY-coupling [14–16]. While few repeats cause a singledomain state at remanence, increasing number of layers leads to multidomain states with out-of-plane magnetization. Generally, the size of volume domains in macroscopic materials increases with ascending dimensions according to a square root relation [Fig. 2.1(c)] [52]. For a profound introduction to magnetic domain patterns and underlying energy contributions, I would like to refer to the book by Hubert and Schäfer [67].

2.2. Magnetism on Curved Surfaces

Advances in microstructuring technology have opened new ways to fabricate low-dimensional systems with arbitrary geometry, including high-mobility 2D electron gases in tubular structures [45, 46], flexible electronic circuits [77–81], spin-wave interference in ferromagnetic tubes [82] and magnetic cap structures [83–85]. Various efforts have been dedicated to elucidate curvature effects on charge and energy transport and localization [86–89] as well as on the behavior of vector and tensor fields [90, 91] on curved surfaces.

Analytical studies of magnetic states in shells with ellipsoidal [92, 93], cylindrical [94–96] and spherical [34] shape have revealed intriguing curvature-driven magnetochiral effects and topologically stabilized magnetization patterns, that were confirmed by micromagnetic simulations [31–33, 35, 36]. A general theoretical framework for curvature effects in thin magnetic surfaces has very recently been proposed by Gaididei *et al.* [28] that revealed an emergent DMI [68] as physical origin of the modified magnetic properties due to the non-trivial structural geometry.

2.2.1. Curvature-Driven Modifications

The magnetic energy E of a thin film with a thickness d comparable to or smaller than the exchange length ($l_{ex} = \sqrt{A/4\pi M_s^2}$ with exchange constant A and saturation magnetization M_s) is given by [28]:

$$E = d \int_{\mathcal{S}} [l_{ex} A \mathcal{E}_{ex} + \lambda (\mathbf{m}\mathbf{n})^2] df, \quad (2.4)$$

with the exchange energy density \mathcal{E}_{ex} , the normalized anisotropy coefficient λ ($\lambda > 0$: easy-surface, $\lambda < 0$: easy-normal), the magnetization \mathbf{m} and the local normal vector \mathbf{n} . The integral is taken over the surface \mathcal{S} parameterized by f . Note that magnetic stray field contributions are neglected in (2.4) and that a uniform magnetization in the direction of the surface normal is assumed resembling a 2D surface in 3D space. \mathcal{E}_{ex} written in Cartesian coordinates as $\mathcal{E}_{ex} = (\nabla m_j)^2$ splits up into three contributions when presented in the local curvilinear basis e_α [28, 29]:

$$\mathcal{E}_{ex} = (\nabla m_\alpha)^2 + K_{\alpha\beta} m_\alpha m_\beta + 2D_{\alpha\beta\gamma} m_\beta \nabla_\gamma m_\alpha. \quad (2.5)$$

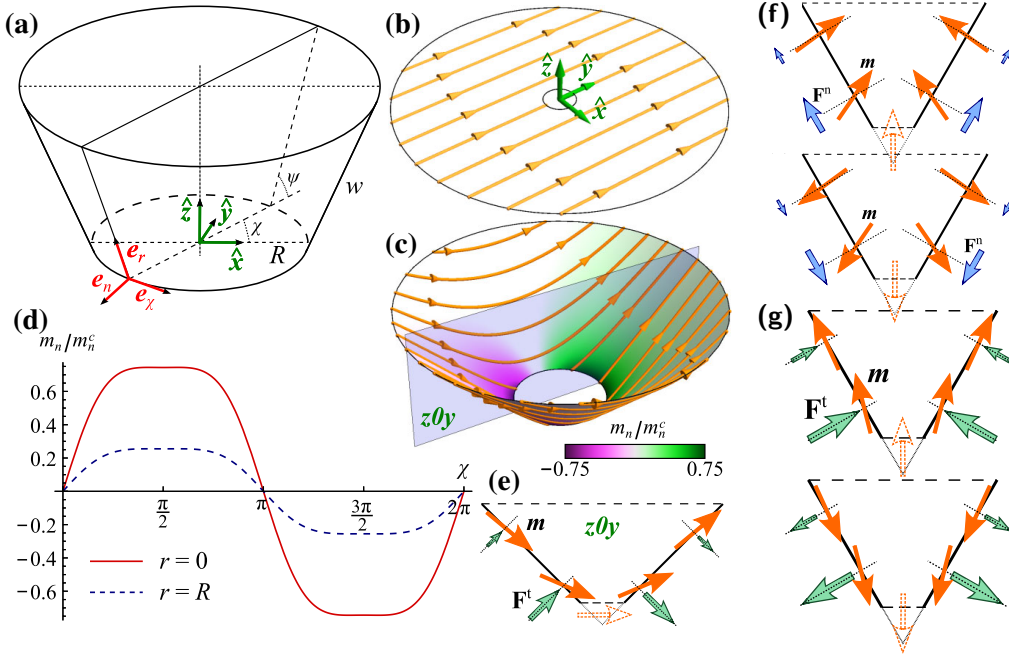


Fig. 2.2.: Curvature-induced Dzyaloshinskii-Moriya interaction in a magnetic cone. (a) Geometry. Panels (b) and (c) depict the onion state in planar and conical geometry, respectively, with in-plane and normal magnetization indicated by streamlines and color scheme, respectively. (d) Variation of the normal magnetization component with varying curvature radius. (e) Schematic distributions of magnetization and emergent fields F^t (tangential) within the cut plane $z\theta y$. (f), (g) Same for radial (easy-normal) and axial states. For each configuration, the fields, either F^t or F^n , are orthogonally to the magnetization and induce a tilt. (Taken from [28])

The tensor elements $K_{\alpha\beta} = \nabla_\gamma e_\alpha \cdot \nabla_\gamma e_\beta$ and $D_{\alpha\beta\gamma} = e_\alpha \cdot \nabla_\gamma e_\beta$ contain the derivative of the local curvilinear basis e_α describing the structural geometry [29]. While the first term has the form of the Heisenberg exchange [first term in (2.1)], the bilinear term emulates an anisotropy-like geometrical potential. The third term manifests a *curvature-driven DMI* [compare with second term in (2.1)] originating from the non-trivial geometrical structure that induces effective magnetic fields orthogonally to the preferential orientation of the magnetic anisotropy [28].

Figure 2.2 illustrates the emergent fields F^t (tangential) and F^n (normal) on the example of a conical surface [Fig. 2.2(a)]. While in planar structures no DMI is observed [Fig. 2.2(b)], the magnetization in cones experiences large field components near areas with large curvature gradient according to $D_{\alpha\beta\gamma} = e_\alpha \cdot \nabla_\gamma e_\beta$, which induce a tilt of the magnetization [purple-green colorspace in Fig. 2.2(c)]. Both DMI and field strength decrease with increasing radius [Fig. 2.2(d)]. Figures 2.2(e)–(g) sketches the emergent field components

for onion, radial (easy-normal) and axial state in a cone. For each configuration, the fields, either F^t or F^n , are orthogonally to the magnetization and induce its tilt.

The emergence of such a vector exchange interaction in curved magnetic surfaces has several implications for both theoretical and experimental studies as well as potential applications in magnetic logic [13] and storage [11, 12, 97] devices. For instance, it gives a possible explanation of the experimentally observed polarity [98, 99] and chirality [100, 101] breaking for soft-magnetic planar vortices due to an enhanced surface roughness, as well as theoretically predicted magnetochiral effects in hemispherical, spherical and cylindrical objects (Sections 2.2.2 & 2.2.3). Furthermore, it offers a new perspective to fabricate magnetic shift registers [11, 12] with 3D non-planar shape and an enlarged domain wall velocity. It may support the current approach of using an interfacial DMI in heterostructures [22–26] to delay the so-called Walker breakdown [102, 103] in in-plane [12, 103–111] and out-of-plane [22, 23, 112, 113] magnetized nanowires.

2.2.2. Magnetic Hemispherical Caps and Spherical Shells

Predicted Properties

Applying the aforementioned theory to soft-magnetic spherical shells reveals vortex states [71–73] on each pole [Fig. 2.3(a)], whose polarity and circulation are strongly dependent on each other [34]. The stabilization of vortices on each pole represents a topological patterning of the magnetization, which is known for spheres as the Hairy ball theorem [114]. The lifted degeneracy of the chirality, describing polarity with respect to the circulation, originates from the curvature-induced DMI (2.5) and is unique to curved magnetic surfaces. The two states shown in Figure 2.3(a) (as side and top view) represent the ground states with the same polarity for both vortices. Considering the depicted magnetic spin texture as a Bloch sphere of the magnetization orientation results in a full 360° rotation of the magnetization. The very same requirement has been established for magnetic skyrmionic states [4, 5, 17] that nucleate in acentric crystal structures [3–8] or in magnetic films with a broken inversion symmetry [17–19, 69]. These magnetic skyrmions are stabilized at low temperatures and in an external magnetic bias field to promote the DMI originating from an inversion symmetry breaking spin-orbital coupling [3, 4, 69]. The similarity of both physical origin and spin texture suggest to name the depicted states skyrmionic.

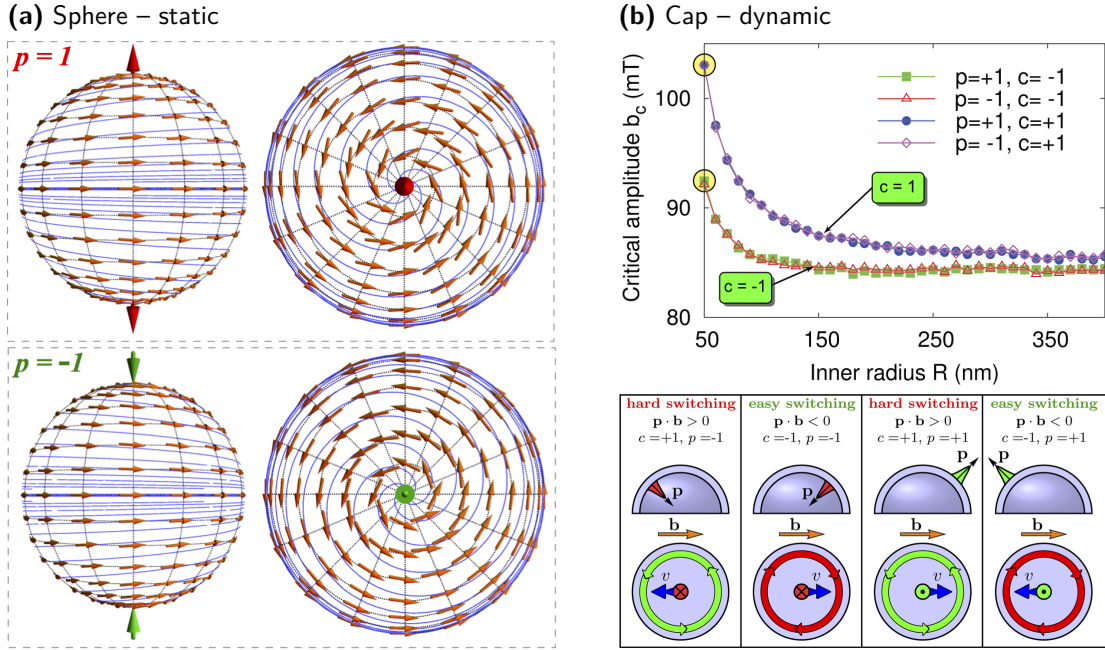


Fig. 2.3.: Magnetochiral effects in (a) nanospheres and (b) nanocaps. (a) Side and top view of the ground states in soft-magnetic spheres with two vortices at each pole possessing the same polarity. The curvature-induced DMI favors spin textures that resemble magnetic skyrmionic textures. (b) Circulation-dependent vortex core switching in magnetic cap structures. Vortex core switches at larger fields if the sign of the projection of magnetic field b onto polarity p coincides with that of circulation c and is positive. (Taken from (a): [34]; (b): [36])

Cutting the magnetic sphere along its equator results in two magnetic cap structures. The corresponding geometry stabilizes domain patterns with radial magnetization, vortex states and hybrid spin textures with tunable tilt angles of the magnetization depending on the magnetic properties of the cap [Fig. 2.4]. The curvature of the magnetic film and thus of the magnetic vortex state lifts the degeneracy of the in-plane circulation upon field pulse excitation perpendicularly [Fig. 2.3(b)] [36] or along the cap normal [116] that offers a controllable switching of the circulation in contrast to planar disks. The switching happens at larger fields if the sign of the projection of magnetic field pulse onto polarity coincides with that of the circulation and is positive [Fig. 2.3(b)]. A very similar effect occurs in tubular nanowires with longitudinal magnetization that possess a preferred and a non-preferred circulation of the domain wall with respect to their dynamic stability [Fig. 2.7]. The switching process initiated by normal magnetic field pulses is mediated by nucleation and subsequent collapse of a circularly closed domain wall [116]. The collapse of the circular domain wall can be accompanied by creation of the chain of vortex-antivortex pairs. The overall field amplitude needed to switch the circulation in hemispherical caps is more than twice smaller than that for planar disks [116].

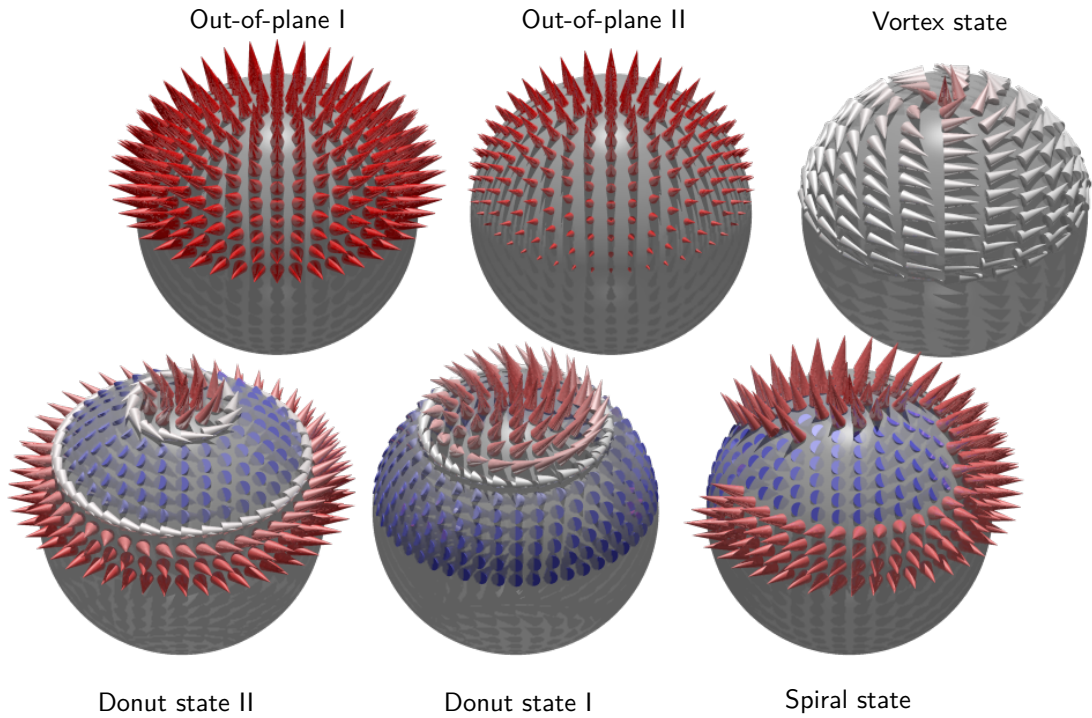


Fig. 2.4.: Schematics of magnetic spin textures in ferromagnetic hemispherical caps investigated in this thesis. Top row: Magnetization configuration in hard-magnetic and soft-magnetic films. The thickness gradient of the cap leads to a radially varying saturation magnetization (out-of-plane II) and to a minimized magnetostatic stray field during vortex core nucleation. Bottom row: Vertically stacking hard- and soft-magnetic layer systems and tailoring the interlayer exchange coupling provides means to imprint non-collinear spin textures into the hard-magnetic subsystem. Out-of-plane magnetization is shaded in red-blue colorspace. (Adapted from [115])

Realization

An elegant way to realize magnetic cap structures or shells is to directly deposit the layers onto curvature templates consisting of non-magnetic spherical particles, cylinders or other three-dimensional objects. Depending on deposition method (electro-chemical or physical deposition) and conditions, the magnetic film will either completely or partially cover the surface of the template resembling cap structures or shells, respectively. Using directed physical deposition, such as magnetron sputtering or electron beam vapor deposition, induces further local thickness variations in the cap structure due to effectively varying deposition angles that modify saturation magnetization and preferential magnetic orientations as well as magnetostatic and interlayer exchange coupling [83–85, 117–122]. As an example, Figure 2.5 shows the effect on out-of-plane magnetized Co/Pd multilayers deposited *via* sputter deposition onto spherical nanoparticles. The multilayers are uniformly

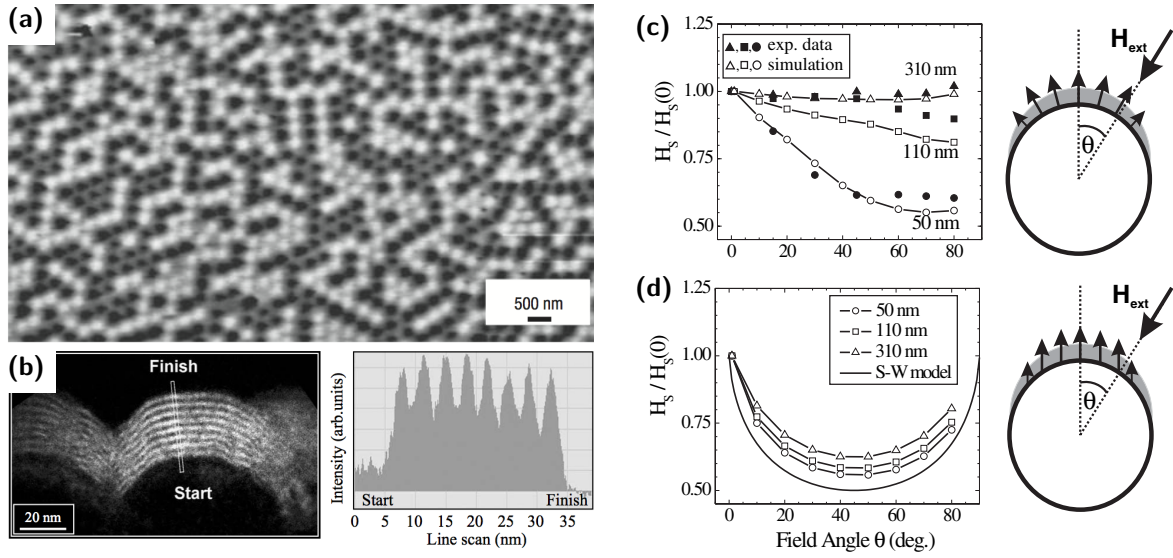


Fig. 2.5.: Magnetic cap structures with out-of-plane magnetization (Co/Pd multilayer stack) obtained by directed deposition onto hemispherical curvature templates. (a) Out-of-plane magnetization component in caps ($\varnothing = 310$ nm) visualized after ac demagnetization with magnetic force microscopy. (b) Energy filtered cross-section image reveals preserved heterostructures recorded by transmission electron microscopy. (c) Comparison between experimentally obtained and simulated angle dependence of switching fields suggest an out-of-plane (radial) magnetic easy axis instead of a single magnetization direction (d). (Taken from (a): [117]; (b): [119]; (c),(d): [118])

saturated on top of each cap [Fig. 2.5(a)] but exhibit a reduced radial magnetization component when approaching the equator [Fig. 2.4] due to structural disorder induced by the shallow angle deposition instead of stacking both materials [Fig. 2.5(b)]. The modification of magnetic properties at the nanoscale influences both magnetic equilibrium domain patterns and magnetization reversal processes [Figs. 2.5(c), 2.5(d)] in individual caps and closely packed assemblies. The impact on magnetostatic and exchange interaction can be adjusted by changing the size of curved template and thickness of the magnetic film.

Current experimental studies on cap structures have been focused on fundamental aspects relevant to applications as *e.g.* bit patterned out-of-plane magnetized media [117, 118], closely packed vortices [83–85] for vortex RAM [97, 123–127] and as self-propelled particles for fuel-free drug delivery in life sciences [128, 129]. Evidence of magnetochiral effects in curved magnetic surfaces remains to be shown due to existing experimental challenges in both sample preparation and visualization techniques.

2.2.3. Magnetic Cylindrical Surfaces

Predicted Properties

Another peculiar 3D surface is a magnetic cylinders with a structural uniaxial symmetry that is expected to reveal intriguing properties depending on the domain pattern. Throughout this thesis, hollow and solid cylinders are referred to as tubes and rods, respectively. The uniaxial symmetry of soft-magnetic nanorods with diameters $\varnothing \lesssim 50$ nm ensures a rotation of the entire transverse domain wall around the symmetry axis [Fig. 2.6(a)] preventing the undesired transformation into a vortex wall [Fig. 2.6(b)] [38] while moving upon current pulse excitation known as the Walker breakdown [102, 103]. This is particularly attractive for magnetic shift registers [11, 12], and magnetic logic devices [13] as the domain wall velocity in planar nanowires without interfacial DMI is typically limited to ≈ 300 m/s because of its biaxial symmetry [12, 103–111].

On the other hand, hollow cylindrical objects with longitudinal magnetization reveal magnetochiral effects on domain walls [Fig. 2.7(a)] that possess a curvature-induced radial magnetization component in contrast to their planar counterparts [32, 33]. The radial component of the domain wall is either increased or decreased while moving [Fig. 2.7(b)]. Thus, the degeneracy in energy of domain walls with left- and right-handed circulation known

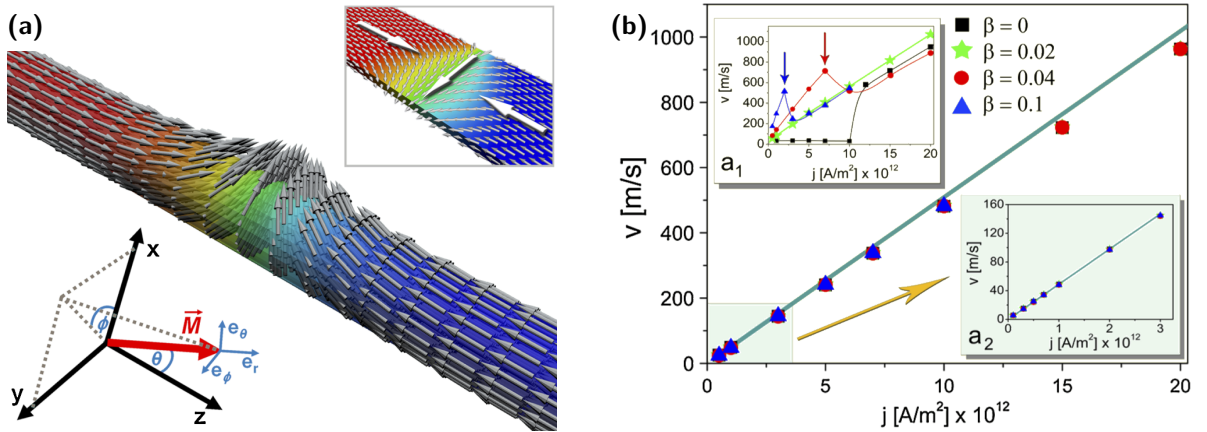


Fig. 2.6.: Domain wall motion up to 1000 m/s in soft-magnetic cylindrical nanorods. (a) Transverse domain wall rotates around the symmetry axis when moving under current pulse excitation. A transition into a vortex domain wall due to emergent normal forces as occurring in its planar counterpart does not happen. (b) No Walker breakdown (deviations from linear relation) for $\varnothing \lesssim 50$ nm is observed. (Taken from [38])

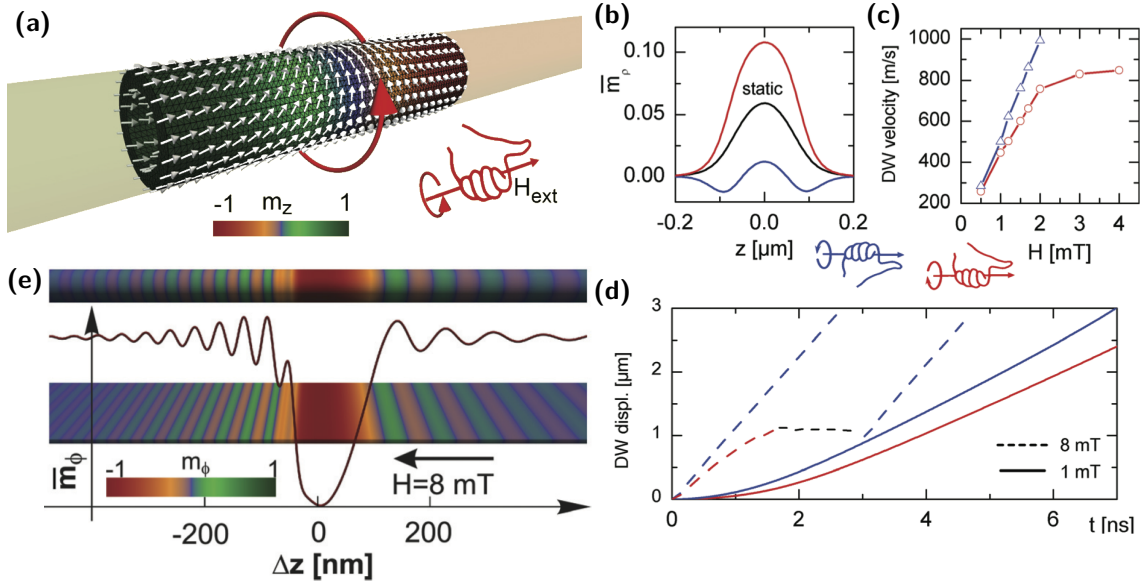


Fig. 2.7.: Magnetochiral effects in soft-magnetic nanotubes. (a) Large curvature induces a radial magnetization component of the domain wall that is absent in its planar counterpart. (b) The radial magnetization lifts the degeneracy of left- and right-handed domain walls while moving, leading to two distinct Walker breakdowns (c). (d) The non-preferred domain wall transforms at sufficiently large velocities via vortex-antivortex pair nucleation into the favorable one. (e) The domain wall with unfavorable circulation emanates while moving [black dashed line in (d)] magnons with different group velocity at front and back side. (Taken from (a)–(d): [32]; (e): [31])

from transverse domain walls in planar nanowires is lifted in magnetic tubes [Fig. 2.7(c)]. In particular, the domain wall with bad circulation (large radial moment) transforms into the favorable one by nucleating vortex-antivortex pairs each moving in opposite direction perpendicularly to the tube axis [32]. The domain wall with unfavorable circulation emanates while moving at a constant velocity (Walker breakdown) [black dashed line in Fig. 2.7(d)] magnons with different group velocity at front and back side [Fig. 2.7(e)] that is referred to as Cherenkov-like effect for magnons [31, 35].

Realization

The experimental realization of such cylindrical magnetic objects is very demanding as high-quality films with acceptable surface roughness and well-defined magnetization textures are required to avoid domain wall pinning on imperfections, such as grain boundaries and edges, that may overshadow curvature effects.

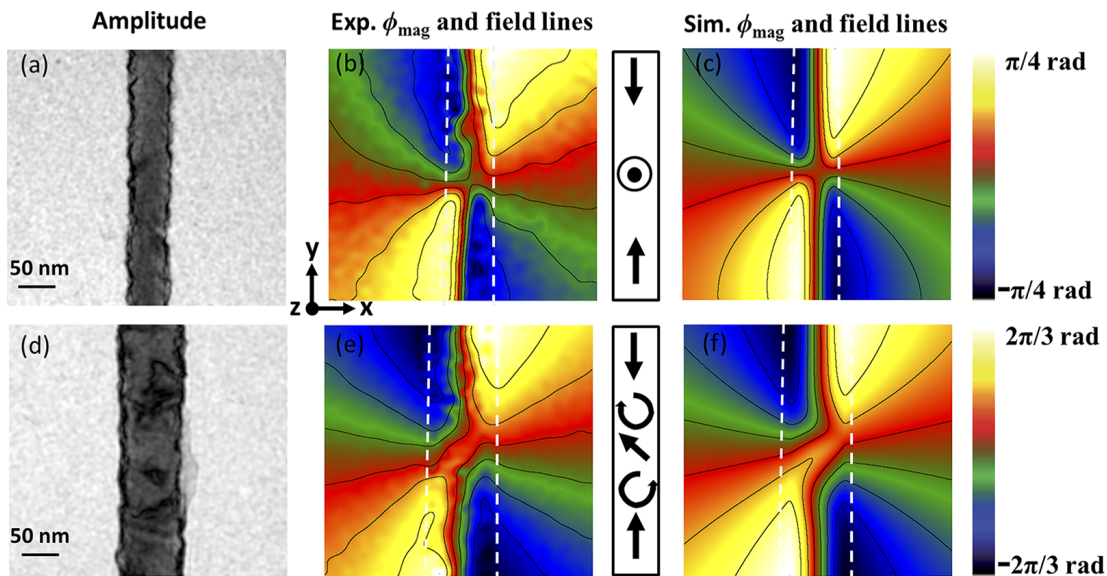


Fig. 2.8.: Magnetization configuration in soft-magnetic nanorods derived from phase shift images with electron holography. Panels (a)–(c) show transmission electron micrograph of a nanorod with $\varnothing \approx 50$ nm and corresponding experimental and simulated phase shift images, respectively, revealing a transverse domain wall. (d)–(f) Larger dimensions favor complicated spin textures like vortices. (Taken from [55])

Cylindrical structures may be fabricated by different synthesis approaches. Rods and tubes with diameters in the nanometer range can be prepared *via* electro-chemical deposition into porous alumina templates [40–44]. These objects possess, due to small dimensions, rather simple domain patterns, *e.g.* longitudinal or azimuthal magnetization, and may successfully be studied using electron holography [Fig. 2.8] [55, 56] or magnetometry [Fig. 2.9] [43, 44]. While soft-magnetic nanocylinders with diameters $\varnothing \lesssim 50$ nm favor transverse domain walls [Figs. 2.8(a)–(c)] as predicted by micromagnetic simulations [Fig. 2.6], rods with larger dimensions reveal more complicated domain walls with vortices located near structural defects [Figs. 2.8(d)–(f)], suggesting strong pinning and the disability to efficiently displace domain walls. This assumption was confirmed with cantilever magnetometry by observing various metastable states in tubes with inner and outer diameters of $\varnothing_{\text{in}} \approx 200$ nm and $\varnothing_{\text{out}} \approx 300$ nm, respectively [43]. Figure 2.9 shows the frequency shift as a function of external magnetic fields applied along the three major orientations of the tube. The magnetic states are identified by correlating the simulated frequency shift of the most likely states with the experimental data, which provides means to study the magnetization reversal process. However, the indirect access to the magnetization offers only a rough classification without particular insight into the spatial distribution and is thus limited to simple magnetic states.

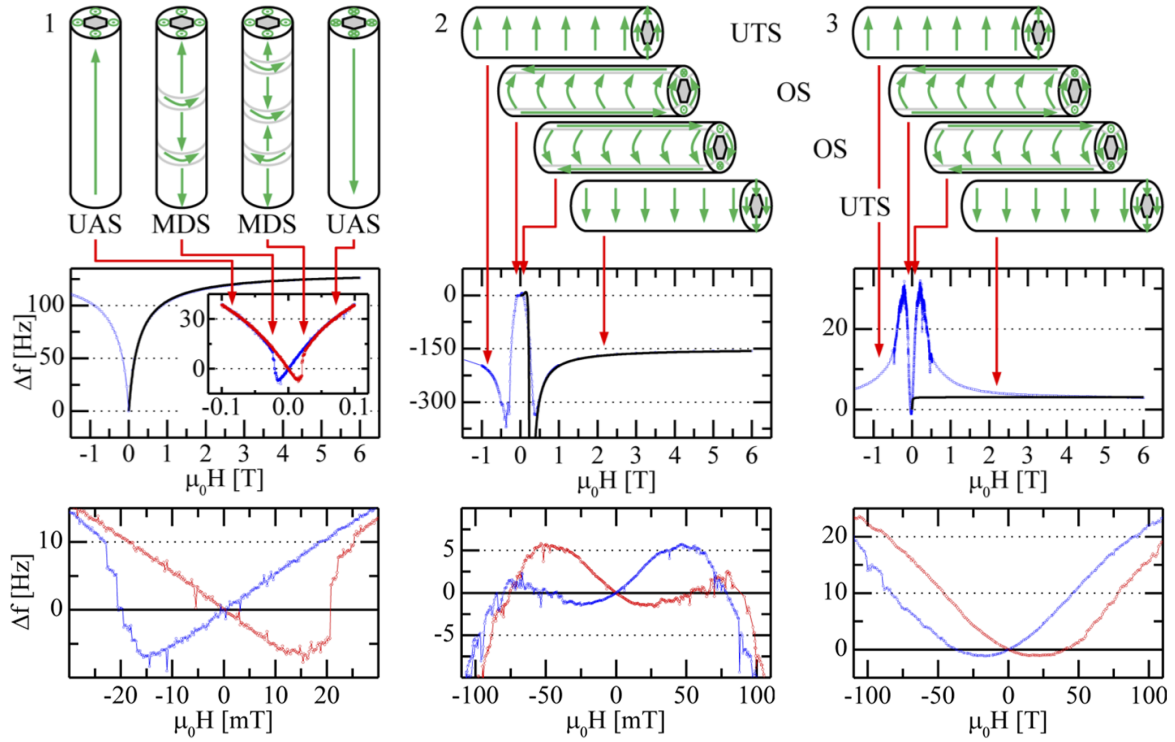


Fig. 2.9.: Stable and metastable magnetic states in magnetic nanotubes ($\varnothing_{in} \approx 200$ nm, $\varnothing_{out} \approx 300$ nm) revealed by cantilever magnetometry. The three curves plot the response along three orthogonal axes as shown in the schematics. Red arrows indicate magnetic fields corresponding to the specified state. (Taken from [43])

More complex, yet deterministic, domain patterns [Fig. 2.10] appear in tubular structures with diameters in the lower micrometer range fabricated by strain engineering rolled-up nanotech [45, 46]. 2D magnetic nanomembranes with either in- or out-of-plane anisotropy rolled up into tightly wound films with cylindrical shape offer well-defined magnetic domain patterns including homogeneous [82, 130, 131] and multidomain states [132, 133] or radial spin textures [134, 135]. It has been shown by ferromagnetic resonance spectroscopy (FMR) [82, 131, 136], magnetoresistance measurements (MR) [42, 133] and magnetic imaging [137] that rolled-up nanomembranes with cylindrical shape resemble tubes with respect to magnetic properties due to magnetostatic coupling between adjacent windings despite of an absent structural uniaxial symmetry. Consequently, magnetic tubular architectures with well-defined properties, *e.g.* azimuthal magnetization with high sensitivity relying on the giant magnetoimpedance effect [138] for magnetoencephalography [139, 140] or radial magnetization for deflecting charged particles, may be prepared in this manner.

State-of-the-art investigations relying on integral measurement techniques, such as FMR [82, 131], MR [42, 133, 141, 142] and magnetometry [43, 44], as well as on the analysis of

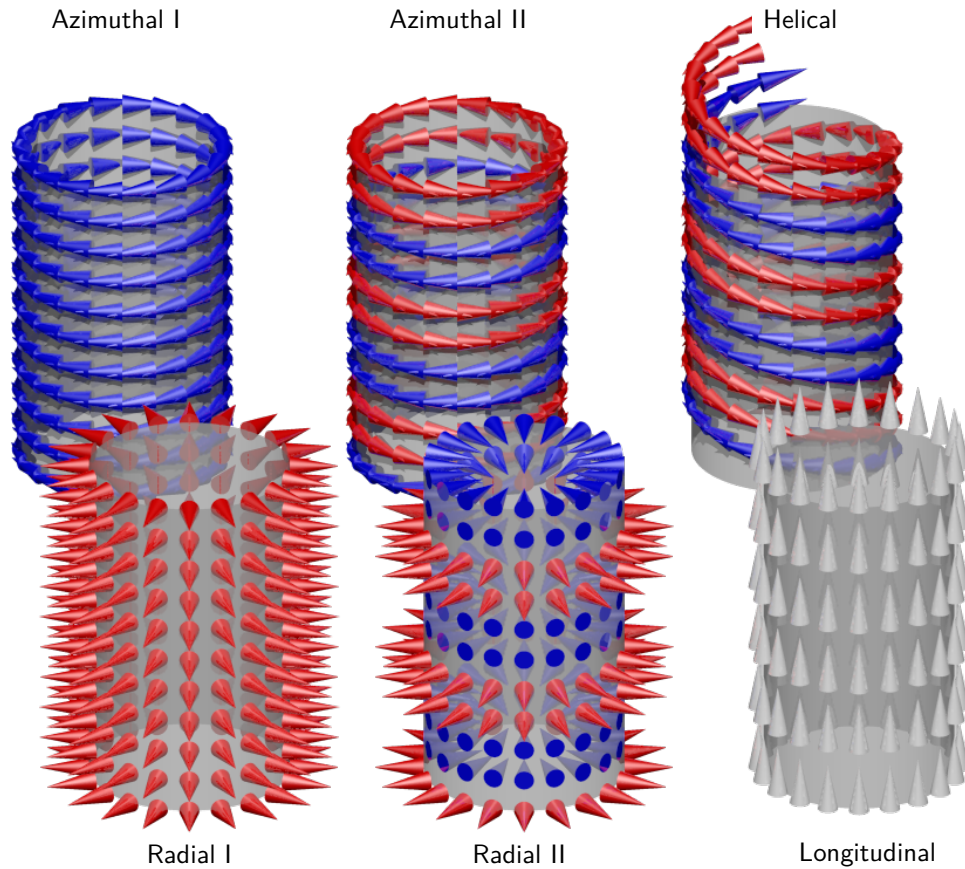


Fig. 2.10.: Schematics of magnetic domain patterns in ferromagnetic thin films resembling hollow cylinders. Top row: Circulating (in-plane) magnetization textures with without (azimuthal) and with (helical) longitudinal components. Circulation sense is indicated by red or blue. Bottom row: Radial and longitudinal magnetization configuration. State radial II illustrates multidomain states with radial magnetized domains. Each configuration possessing distinct magnetic and magnetoelectric properties can be fabricated by rolling up planar films.

2D projections of magnetization patterns recorded with Kerr [132, 133] and X-ray [137] microscopy may serve as precharacterization but do not provide means to retrieve the 3D magnetic domain pattern. A proper identification can only be accomplished by magnetic tomographic imaging and reconstruction.

2.3. Tomographic Imaging

Conventional visualization techniques, such as microscopy, record a 2D projection of a 3D attenuation field associated with the spatial distribution of atomic mass densities or

electromagnetic fields. Depending on the experimental setup working either in reflection or transmission mode, information about outermost surfaces or thickness-integrated bulk regions are obtained, respectively. In order to retrieve the 3D information from a set of 2D projections, tomographic reconstruction algorithms have been developed [143] and applied to various classes of materials.

The first work on the mathematical background of tomographic imaging traces back to Radon [144], who derived the reconstruction formula for a localized 2D function $\mu(x, y)$ whose integral values along certain directions are known. In particular, the integral value can be considered as the transmitted intensity:

$$I = I_0 \exp \left[- \int_{\mathcal{C}} \mu(x, y) dr \right], \quad (2.6)$$

with the initial intensity I_0 , the localized absorption coefficient $\mu(x, y)$, the integration path \mathcal{C} parameterized by $r = -x \sin \alpha + y \cos \alpha$ with the projection angle α . The projection

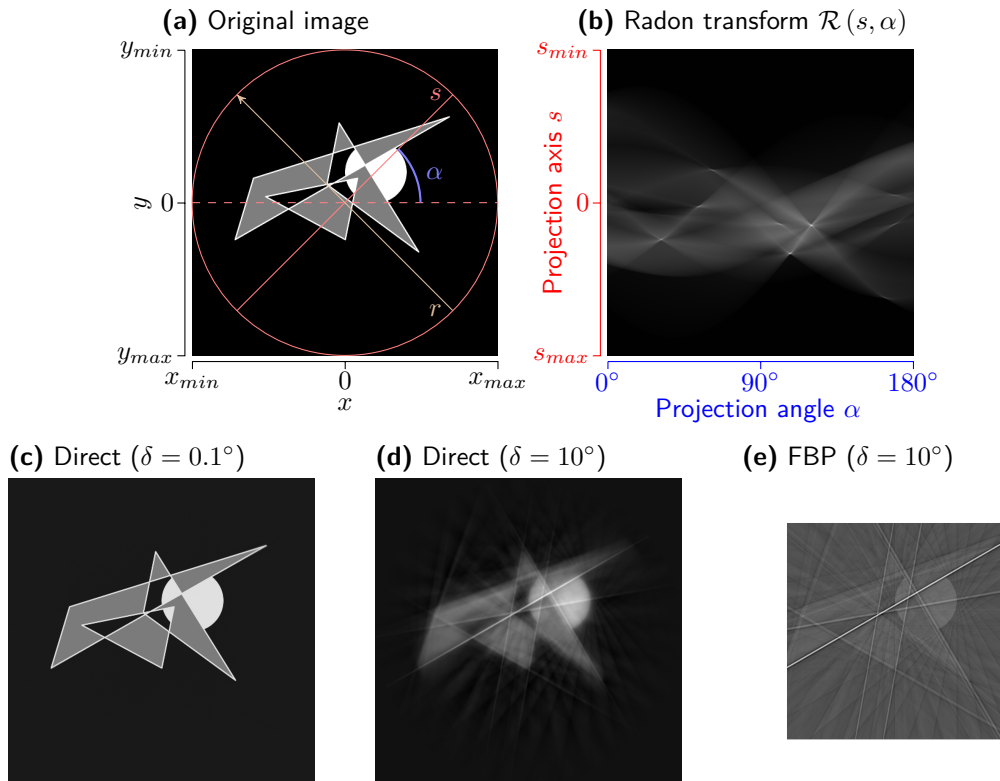


Fig. 2.11.: Schematics of Radon transformation and back projection in 2D. (a) Original image with indicated projection angle α and projection axis s . (b) Radon transform of (a). Direct iterative reconstruction with rotation step sizes (c) $\delta = 0.1^\circ$ and (d) $\delta = 10^\circ$. (e) Reconstruction with filtered back projection (FBP) and $\delta = 10^\circ$.

axis $s = -x \cos \alpha - y \sin \alpha$ is orthogonal to r [Fig. 2.11(a)]. The Radon transform $\mathcal{R}(s, \alpha)$ [Fig. 2.11(b)] is obtained after rewriting (2.6) as:

$$\mathcal{R}(s, \alpha) = \ln \left(\frac{I}{I_0} \right) = \int_{\mathcal{C}} \mu(-s \sin \alpha - r \cos \alpha, s \cos \alpha - r \sin \alpha) dr. \quad (2.7)$$

Its invariance under translation and rotation allows to perform Fourier transformations and to reconstruct μ from a set of projections using the Fourier slice theorem. Accordingly, calculating the 1D Fourier transform of \mathcal{R} with respect to s $FT_1[\mathcal{R}(s, \alpha)] = \tilde{\mathcal{R}}(S, \alpha)$, with the reciprocal space vector component S , and performing the 2D inverse Fourier transformation $(FT_2)^{-1}$ leads to the spatial distribution of the absorption coefficient μ [144]:

$$\left. \begin{aligned} \mu(x, y) &= (FT_2)^{-1} \{FT_1[\mathcal{R}(s, \alpha)]\} = (FT_2)^{-1} [\tilde{\mathcal{R}}(S, \alpha)] \\ &\simeq \int_0^\pi d\alpha \int_{\mathbb{R}} dS \cdot \tilde{\mathcal{R}}(S, \alpha) H(S) \exp[2\pi i S(-x \sin \alpha + y \cos \alpha)]. \end{aligned} \right\} \quad (2.8)$$

The filter $H(S) = |S| \left[\Theta \left(S + \frac{1}{2\Delta s} \right) - \Theta \left(S - \frac{1}{2\Delta s} \right) \right]$, with the Heaviside function Θ , the pixel size of the screen Δs and the Nyquist frequency $\frac{1}{2\Delta s}$ [145], ensures a defined integral. The filtered backprojection (2.8) is basis for almost all tomography reconstruction algorithms.

Alternatively, the inverse Radon transform can be considered as a system of linear equations [143] similarly to the Radon transform (2.6) itself, since each trajectory r passes through a small fraction of space. Applying simultaneous algebraic reconstruction techniques, such as the Kaczmarz' method [146], allows to directly reconstruct $\mu(x, y)$ without applying the Fourier slice theorem [Fig. 2.11(c)]. The avoidance of Fourier transformations provides means to reconstruct $\mu(x, y)$ from few projections [Figs. 2.11(d), 2.11(e)], to increase the spatial resolution or to address each Radon transform individually. The latter aspect is crucial to treat vector fields, such as the magnetization.

Meanwhile, tomographic imaging has become a powerful technique that reveals internal structures in complex organic [53, 62–64, 147, 148] and inorganic [51, 52, 54–61] objects by exploiting high penetrability and short wavelengths (high spatial resolution) of various kinds of radiation sources, including electron, neutron and X-rays. Among others, conditions during formation of minerals [59] and ceramics [61] as well as functioning and interplay of biological cells at subcellular level [62, 147] have been identified. Magnetic objects with macroscopic and nanoscopic expansions have been investigated using magnetic

neutron tomography [51, 52] and electron-based techniques, including electron holography [53–56, 148] and vector field electron tomography [57, 58], respectively.

2.3.1. Magnetic Neutron Tomography

The capability to characterize 3D spatial distributions of magnetic domains has been demonstrated by magnetic neutron tomography [51, 52] with a spatial resolution of $\approx 50 \mu\text{m}$ [Fig. 2.12]. Neutron tomography relies on the detection of the phase shift, namely intensity difference, due to local variations in the refractive index originating from domain walls aligned parallel to the neutron propagation direction [149]. In particular, the refractive index with the spin-dependent term $\varphi = \pm \frac{1}{2} \mu_n B / E_n$ (magnetic moment of the neutron μ_n , and neutron kinetic energy E_n) [52] causes a distinct momentum transfer for parallel and anti-parallel neutron spin orientations with respect to the magnetic induction

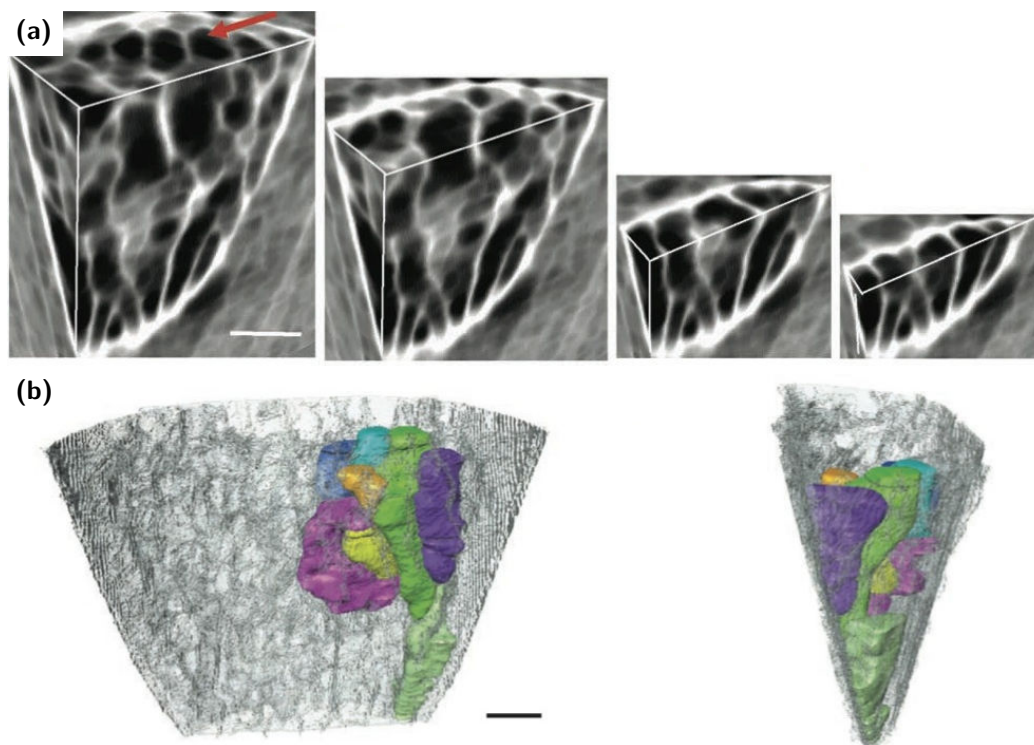


Fig. 2.12.: (a) Magnetic neutron tomography of a macroscopic FeSi wedge reveals the 3D spatial distribution of magnetic domain walls (bright) with a spatial resolution of about $100 \mu\text{m}$. (b) Reconstructed domain distribution. Each color refers to a different domain. Information about surface domains and the magnetization itself cannot be retrieved with this approach. The scale bar is 1 mm. (Taken from [52])

B . Hence, neutrons penetrating the media close to a domain wall experience a phase shift that is not compensated by subtracting intensities recorded for neutron beams with parallel and antiparallel spin orientation. The 3D spatial distribution of the domain walls is obtained from a set of projections [Fig. 2.12] *via* direct iterative reconstruction without applying the Fourier slice theorem [150] analogously to [146]. The treatment of individual projections provides the basis for capturing the angle-dependent phase shift contributions. Accordingly, an evaluation of the domain morphology can be given by identifying regions with dark contrast as volume domains.

The weak interaction between neutrons and induction B requires an accumulation of the phase shift over $\approx 100 \mu\text{m}$. Thus, domain walls smaller than $100 \mu\text{m}$ or tilted against the neutron propagation direction cannot be resolved. On the other hand, an absorption coefficient of $\mu \approx 10^{-3}/\mu\text{m}$ for transition metals and hot neutrons (three orders smaller than those of X-rays) allows to investigate bulky materials, *e.g.* single crystals, alloys and their modifications due to encapsulation or degradation relevant for industry. Constant phase shift and unaffected trajectory of neutrons when exposed to an homogeneous magnetic field provide further means to study magnetization reversal processes based on the evolution of the volume domain walls as no information about the magnetization itself or surface domains are accessible.

2.3.2. Electron-based 3D Imaging

First successful attempts to access magnetic properties in 3D space with nanometer resolution have been accomplished in uniformly magnetized nanoparticles [54, 148], nanorods/nanospirals [55, 56] and magnetotactic bacteria [53, 148] with spatial expansions $< 100 \text{ nm}$ by phase shift reconstruction with electron holography [151, 152] or Lorentz electron microscopy and employing the transport-of-intensity equation (TIE) [153, 154]. More recently, the capability of vector field electron tomography (VFET) [155, 156] was demonstrated by reconstructing magnetic vortex cores in soft-magnetic disks [57, 58].

Phase Shift Reconstruction

These approaches are based on the knowledge of the electron's phase shift traveling through a 3D space with an electrostatic potential $V(\mathbf{r})$ and a magnetic vector potential $\mathbf{A}(\mathbf{r})$

[157]:

$$\left. \begin{aligned}
 \varphi(\mathbf{r}_\perp) &= \varphi_e(\mathbf{r}_\perp) + \varphi_m(\mathbf{r}_\perp) \\
 &= C_e \bar{\varphi}_e(\mathbf{r}_\perp) + C_m \bar{\varphi}_m(\mathbf{r}_\perp) \\
 &= C_e \int_{\mathcal{C}} V(\mathbf{r}_\perp + l\boldsymbol{\omega}) dl - C_m \int_{\mathcal{C}} \boldsymbol{\omega} \cdot \mathbf{A}(\mathbf{r}_\perp + l\boldsymbol{\omega}) dl.
 \end{aligned} \right\} \quad (2.9)$$

Similarly to the original formula (2.7), the thickness-integrated information (2.9) constitutes line integrals along the trajectory \mathcal{C} , parameterized by l , in the direction of $\boldsymbol{\omega}$. In fact, $\bar{\varphi}_e(\mathbf{r}_\perp)$ is the representation of (2.7) in 3D. The 2D position vector \mathbf{r}_\perp lies in the projection plane so that $\boldsymbol{\omega} \cdot \mathbf{r}_\perp = 0$. Further are $C_e = e\pi/\lambda E_e$ and $C_m = e/\hbar$, with the electron wave length λ and the electron kinetic energy E_e .

Accordingly, the phase shifts of coherent electron beams reflect the thickness-integrated interaction with a magnetic induction $\mathbf{B}_\perp = (\nabla \times \mathbf{A})_\perp$ perpendicular to the e-beam propagation direction. In particular, isophase lines coincide with the magnetic field lines/magnetization components lying in the projection plane. Thus, phase shift reconstructions performed with projections taken at the same angle may only be applied by correlation with simulations [Fig. 2.8] to reveal simple magnetization textures as occurring in *e.g.* uniformly magnetized nanoparticles [54, 148], nanorods [55, 56] or assemblies of those [53, 148]. An example of chains of superparamagnetic nanoparticles in magnetotactic bacteria is given in Figure 2.13 recorded with electron holography [151, 152] that visualizes the phase shift

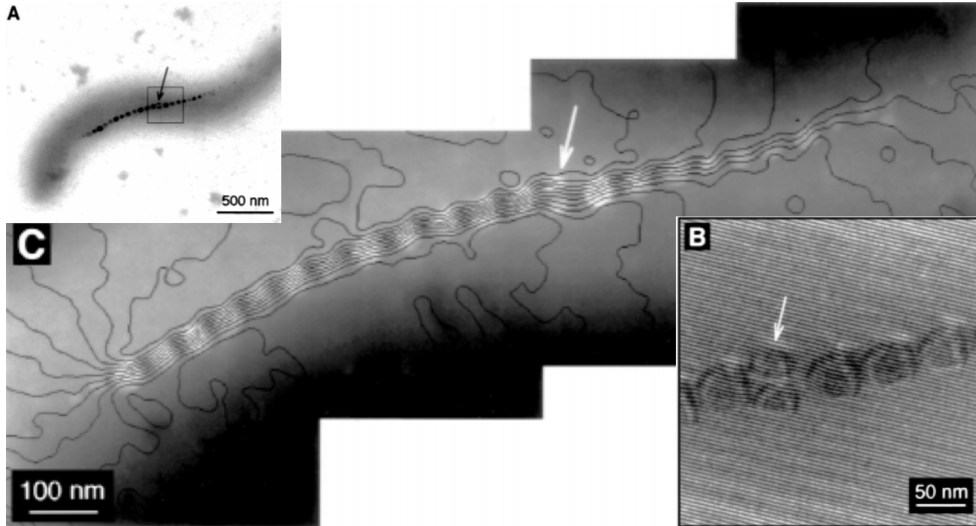


Fig. 2.13.: *Electron holography of the magnetic induction of a chain of superparamagnetic nanoparticles in magnetotactic bacteria. (a) Transmission micrograph to identify strongly absorbing metal regions. (b) Recorded phase shift due to interaction with magnetic induction. (c) Reconstructed thickness-integrated field lines of the magnetic induction reveal magnetization vectors aligned along the chain. (Taken from [53])*

between reference beam $\psi_1 = e^{i\mathbf{k}_1\mathbf{r}}$ and probe beam $\psi_2 = \xi(\mathbf{r})e^{i\mathbf{k}_2\mathbf{r}+i\varphi(\mathbf{r})}$ by coherent interference on the CCD screen using an electron biprism [158]. Both amplitude $\xi(\mathbf{r})$ and phase $\varphi(\mathbf{r})$ originating from interaction with electromagnetic fields of the sample are captured in the recorded intensity pattern according to:

$$\left. \begin{aligned} I(x) &= |\psi_1 + \psi_2|^2 \\ &= 1 + \xi^2(\mathbf{r}) + \kappa\xi(\mathbf{r}) \cos[(\mathbf{k}_1 - \mathbf{k}_2)\mathbf{r} - \varphi(\mathbf{r})] . \end{aligned} \right\} \quad (2.10)$$

The contrast is reduced by the coefficient κ that takes into account temporal and spatial coherence of the electron beam. In contrast, Lorentz microscopy with TIE omits the use of a reference beam by accumulating a through-focus series of images that reveals the thickness-integrated magnetic induction components perpendicular to the e-beam propagation direction according to $\nabla\varphi = C_m\mathbf{B}_\perp d$ with the sample thickness d [154]. Varying focus changes the size of the probing area and thus the amount of enclosed flux lines that is reflected by the gradient of the phase shift. Nevertheless, both approaches only provide a thickness-integrated information of the magnetic induction of the nanoscopic sample along on e-beam projection direction.

Vector Field Electron Tomography

The loss of local information about the phase shift can be avoided by acquiring projections at different angles while rotating/tilting the sample around at least two axes. Calculating the 1D Fourier transform of $\bar{\varphi}_e(\mathbf{r}_\perp)$ and $\bar{\varphi}_m(\mathbf{r}_\perp)$ with respect to reciprocal space vector \mathbf{S} and applying the Fourier slice theorem (2.8) with the 1D Fourier transformation FT_1 and the inverse 2D Fourier transformation $(FT_2)^{-1}$, one obtains the mathematical basis of VFET [156]:

$$V(\mathbf{r}) = (FT_2)^{-1} \{FT_1[\bar{\varphi}_e(\mathbf{r}_\perp)]\} = (FT_2)^{-1} [\tilde{\varphi}_e(S_y, \alpha)] , \quad (2.11)$$

$$B_x(\mathbf{r}) = (FT_2)^{-1} \{iS_y \cdot FT_1[\bar{\varphi}_m(\mathbf{r}_\perp)]\} = (FT_2)^{-1} [iS_y \cdot \tilde{\varphi}_m(S_y, \alpha)] , \quad (2.12)$$

$$B_y(\mathbf{r}) = (FT_2)^{-1} \{iS_x \cdot FT_1[\bar{\varphi}_m(\mathbf{r}_\perp)]\} = (FT_2)^{-1} [iS_y \cdot \tilde{\varphi}_m(S_x, \alpha)] . \quad (2.13)$$

Equations (2.11) and (2.12) describe the angular dependence for rotations around the x -axis, while (2.13) considers rotations around y . The phase shift is accumulated along the trajectory \mathcal{C} at the projection angle α . Note that α is determined by \mathbf{r}_\perp in real space. Using the Maxwell equation $\nabla\mathbf{B} = 0$ allows to reconstruct the magnetic induction \mathbf{B} from

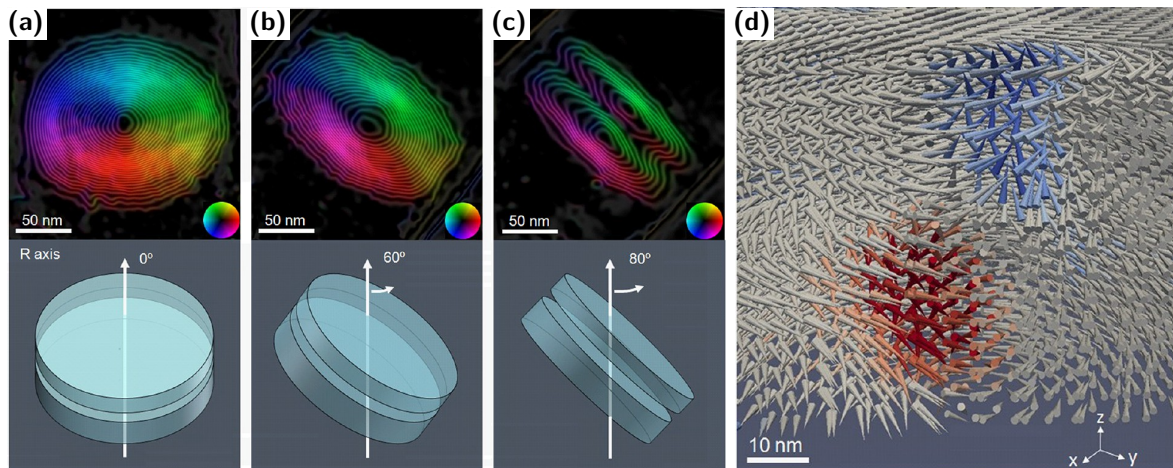


Fig. 2.14.: *Vortex core interaction in vertically stacked soft-magnetic disks revealed by vector field electron tomography with transmission electron microscopy. (a)–(c) Acquiring phase shifts at various projection angles around at least two rotation axes allows to reconstruct the 3D spatial distribution of the magnetization at the nanoscale (d). (Taken from [58])*

a set of projections around at least two rotation axes. Electrostatic contributions $\bar{\varphi}_e(\mathbf{r}_\perp)$ can be compensated by subtracting projections along opposite trajectories.

An experimental demonstration of the capability of VFET was very recently given by reconstructing the spin configuration in two vertically stacked planar soft-magnetic disks with a spatial resolution of few nanometers using a 1 MV holography electron microscope [58]. However, facilitating electrons as a probe is disadvantageous for in-field measurements on mesoscopic samples due to their electric charge and strong absorption coefficients, nor do they provide an element specificity. These highly demanded features can be offered by X-ray magnetic circular dichroism-based 3D imaging techniques (Section 4.3).

3. Fabrication Methods

This chapter provides a detailed overview of the preparation methods and sample architectures used within this thesis. Magnetic cap structures with one single curved surface at the top are fabricated by deposition onto non-magnetic curvature templates.* Strained nanomembranes with magnetic layers are rolled up into cylindrical objects with two or more surfaces, referring to the number of magnetic layers in radial direction.

3.1. Deposition onto Curvature Template

Exploiting the shape of a non-magnetic 3D object that acts as a curvature template during deposition is one of the most elegant ways to obtain curved magnetic films. Depending on the directionality of the deposition, the magnetic film covers either completely or partially the surface of the template. The resulting shell or cap structure may further possess local thickness variations that modify magnetostatic and interlayer exchange coupling [83–85, 117–121].

3.1.1. Hemispherical Cap Structures

Using monolayers of self-assembled closely packed spherical particles [159–161] as curvature template offers both high symmetry of the resulting cap structure and the possibility to prepare highly ordered cap arrays (Sections 5.1 & 5.2). Depending on the purpose either silica or polystyrene (both Bangs Laboratories) spheres with a diameter \varnothing in the range from 50 nm to 5 μ m are used. The colloidal solution containing the particles is drop-casted onto a slightly tilted naturally oxidized Si wafer that was exposed for 10 s to

*All samples were prepared at the Institute for Integrative Nanosciences, IFW Dresden.

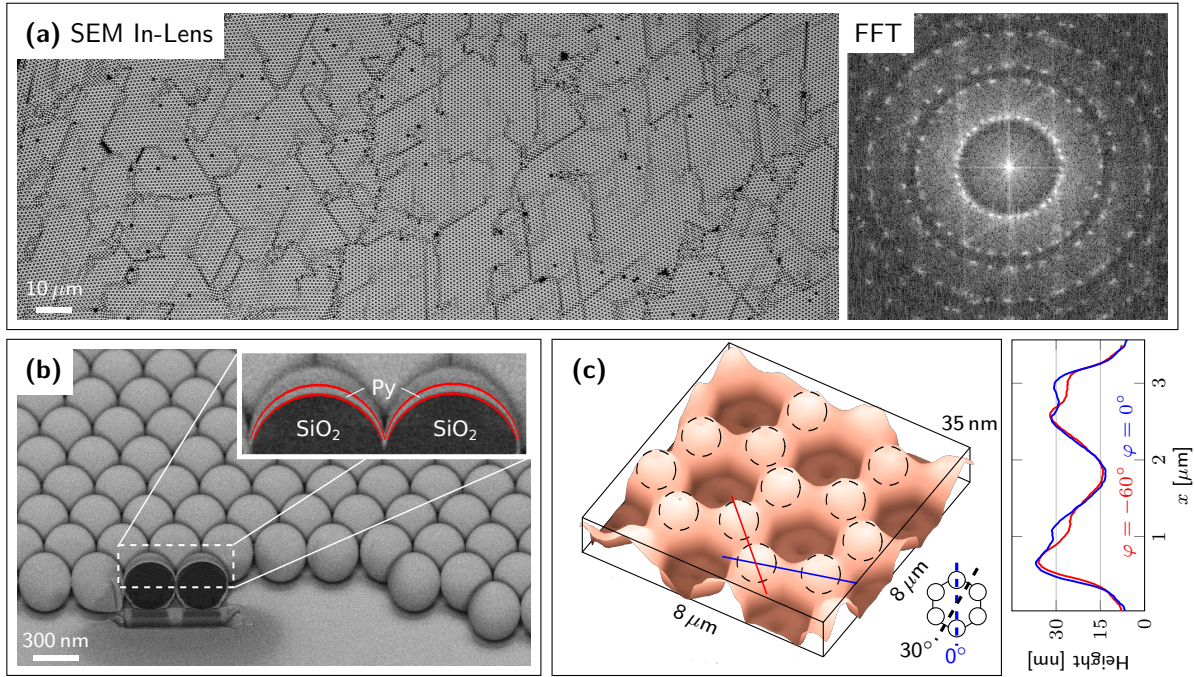


Fig. 3.1.: Self-assembled particle monolayers serving as curvature templates and lithography masks for non-planar architectures. (a) Scanning electron micrograph of silica monolayers self-assembled into structural domains with approximately one thousand spheres. The lattice orientation of each domain is slightly rotated against adjacent specimens. Inset shows FFT of the assemblies. (b) Self-assembled silica monolayer capped with 40 nm-thick Permalloy. The cross-section prepared by focused ion beam etching reveals a thickness gradient with a minimum at the equator. (c) Upon removal of the monolayer a non-planar honeycomb lattice is observed by atomic force microscopy. The emergent height asymmetry of the vertices can be tuned during deposition. (Taken from (b): [?]; (c): [163])

an oxygen plasma to enhance adhesion. While the droplet does not spread out without plasma treatment, long surface activation leads to droplet breathing and self-assembling of low structural quality. The drop-cast approach provides means to assemble spherical particles into monolayers at the wafer scale [162]. In this thesis, cap arrays consisting of approximately one thousand unit cells are used, which is in case of $\varnothing = 3 \mu\text{m}$ equal to a structural domain size of $(90 \times 90) \mu\text{m}^2$. Each structural domain possesses a slightly rotated lattice orientation [Fig. 3.1(a)], which makes the approach very attractive for orientation-dependent microscopy investigations.

The metal stack is deposited onto the particle monolayers *via* magnetron sputtering (DCA Instruments) at room temperature (base pressure: 7×10^{-8} mbar; Ar pressure: 10^{-3} mbar; deposition rate: ≈ 0.3 ML/s) through an aperture to ensure a directed deposition. The resulting curvature-driven thickness gradient exhibits the nominal thickness at the very

center of the cap and a persistently decreasing thickness towards the equator [Fig. 3.1(b)].

3.1.2. Non-Planar Honeycomb Lattice

The propagation vector distribution within the sputter plasma assures deposition both through the interstitials of mono-, bi- and trilayers and under the particles [164, 165]. Upon removal of the particle monolayers using ultrasonication, a non-planar honeycomb lattice with periodically alternating thickness is obtained [Fig. 3.1(c)] [164]. Lattice periodicity, thickness and width of the interconnects can be adjusted by changing particle size, thickness of deposited materials and plasma etching of PS particles before metal deposition, respectively [163–165]. Engineering a height asymmetry into the honeycomb lattice is achieved by positioning the sample under the aperture with a radial offset.

3.2. Rolled-up Nanotech

Rolled-up nanotechnology [45, 46] is a versatile approach to fabricate rolled-up nanomembranes with cylindrical shape out of any thin film by strain-engineering and selective release of the sacrificial layer. Using conventional thin film deposition techniques, such as molecular beam epitaxy (MBE), electron beam vapor deposition (EBVD) or sputter deposition, ensures both high quality of the deposited film and on-chip integrability [166–169]. In particular, it provides means to prepare magnetic tubular architectures with tunable magnetization configuration, such as longitudinal, circulating or out-of-plane magnetization, which is not feasible to achieve by any other state-of-the-art method such as electrochemical deposition into porous alumina templates.

The physical origin of the rolling process is the strain release upon curving the nanomembrane. However, if the initial strain gradient is too small to initiate a bending and thus a rolling of the nanomembrane, the film will instead wrinkle perpendicularly to the expected rolling direction [Fig. 3.2] [49, 50]. The equilibrium curvature due to strain relaxation can be calculated in the framework of continuum mechanics [170]. Assuming similar Young's moduli of both layers and complete strain relaxation at the free surfaces, the tube diameter

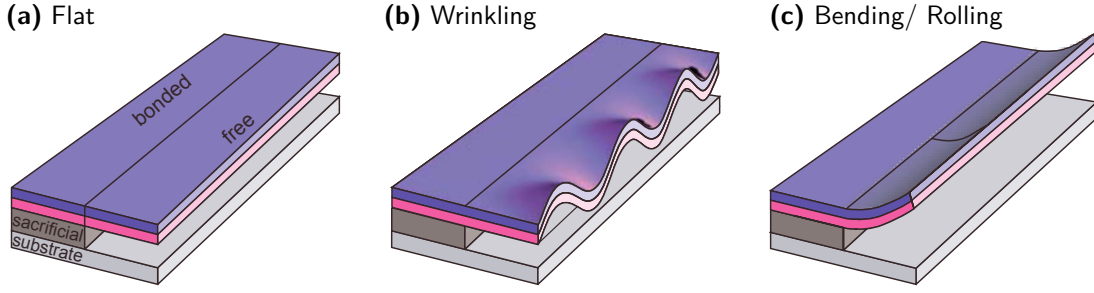


Fig. 3.2.: *Wrinkling and rolling of strained free-standing nanomembranes for strain relaxation. Depending on the strain gradient normal to the surface the selectively released layer will (a) stay flat, (b) wrinkle along the free-standing edge or (c) bend and roll perpendicularly to this edge. The latter case is preferred for large strain gradients. (Taken from [49])*

\varnothing reads [47]:

$$\varnothing = \frac{1}{3\varepsilon} \frac{(d_1 + d_2)^3}{d_1 d_2}, \quad (3.1)$$

with the lateral strain ε normal to the surface and the film thicknesses d_1 and d_2 of layer 1 and 2, respectively. The resulting tube dimension is linear in thickness and in reciprocal of the strain. For a given strain, the smallest tube is obtained for bilayers with same thickness.

3.2.1. Epitaxial Strained Films

The concept of rolled-up nanotech was originally proposed for epitaxially strained semiconducting bilayer systems with potentially large strain gradients [45, 46] and tube diameters down to $\varnothing \lesssim 50$ nm [Fig. 3.3] [47]. The lattice constant of one layer may be altered by varying doping concentration [45] or changing composition [47] of the bilayers, which accordingly affects the lateral strain normal to the surface inside the bilayers.

The tubular semiconductor architectures used as curvature templates in Section 5.3 and as strained non-magnetic layers in Section 6.2 are prepared (in collaboration with Dr. D.J. Thurmer) by rolling up $\text{In}_{33}\text{Ga}_{67}\text{As}/\text{GaAs}$ nanomembranes with various thicknesses [Fig. 3.4(a)]. The strained bilayer stack is epitaxially grown at $T = 550^\circ\text{C}$ (base pressure: 7×10^{-8} mbar; deposition rate: ≈ 0.3 ML/s) by solid-source molecular beam epitaxy (MBE, Omicron) onto a 20 nm-thick AlAs sacrificial layer, which is on top of semi-insulating single-crystal GaAs(001) wafers. The epitaxial growth is monitored by reflection high energy electron diffraction (RHEED) analysis to ensure high-quality crystal growth and smooth

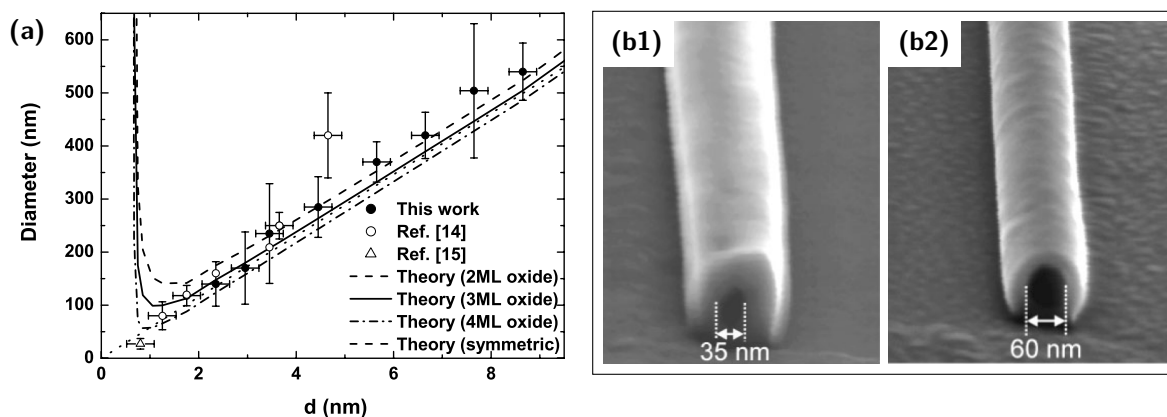


Fig. 3.3.: Rolled-up epitaxially grown nanomembranes with submicrometer diameter. (a) Down-scaling of the tube diameter formed with symmetric $\text{In}_{33}\text{Ga}_{67}\text{As}/\text{GaAs}$ bilayers. Panels (b1) and (b2) depict the smallest rolled-up nanomembranes made of 1.4 ML $\text{In}_{33}\text{Ga}_{67}\text{As}/1.4$ ML GaAs and 1.4 ML $\text{InAs}/1.4$ ML GaAs , respectively. (Taken from [47])

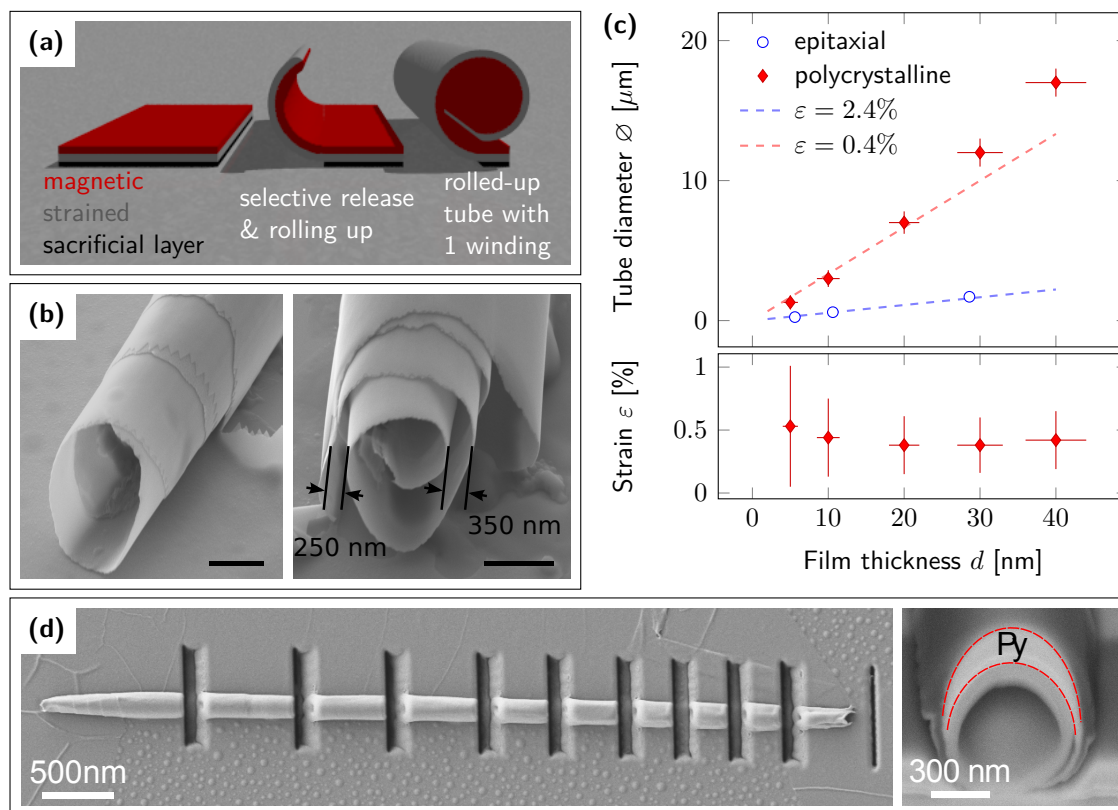


Fig. 3.4.: Fabrication of rolled-up nanomembranes with cylindrical shape. (a) Magnetic layer is deposited onto a strained nanomembrane that can be selectively released. (b) Structural geometry (loosely or tightly wound) can be varied by adjusting process parameters. Scalar bars indicate 1 μm . (c) Relation between film thickness and tube diameter in epitaxial and polycrystalline films for the same deposition parameters. (d) Segmenting of cylindrical curvature templates using focused ion beam etching. Inset shows thickness gradient of a nominal 100 nm thick Py film. (Taken from (a), (b): [137]; (d): [84]; adapted from (c): [133])

Tab. 3.1.: *Structural parameters of rolled-up nanomembranes consisting of strained epitaxial semiconductor bilayers ($\text{GaAs}(d_2)/\text{In}_{33}\text{Ga}_{67}\text{As}(d_1)$, $\varepsilon = 2.4\%$). Experimental and calculated tube diameter using (3.1) show excellent agreement.*

Thickness d_1 [nm]	Thickness d_2 [nm]	Diameter $\varnothing_{\text{theo}}$ [μm]	Diameter \varnothing_{exp} [μm]
2.0	2.6	0.26	0.25 ± 0.01
5.0	5.6	0.59	0.60 ± 0.04
14.0	14.6	1.59	1.7 ± 0.1

layers. Deep trenches are mechanically scratched into the surface to determine the initial edge of selective release from the substrate. Afterwards, the sample is exposed for 15s to 5% wt. hydrofluoric acid (HF), which shows a large selectivity for etching AlAs over GaAs [171]. Upon selective release, the free surface layer of $\text{In}_{33}\text{Ga}_{67}\text{As}$ expands from $a_{\text{GaAs}} = 5.66 \text{ \AA}$ to $a_{\text{In}_{33}\text{Ga}_{67}\text{As}} = 5.80 \text{ \AA}$, equal to a strain of $\varepsilon = 2.4\%$, and induce a rolling up of the entire bilayer system. The lattice constant of $\text{In}_{33}\text{Ga}_{67}\text{As}$ is linearly interpolated between $a_{\text{GaAs}} = 5.66 \text{ \AA}$ and $a_{\text{InAs}} = 6.06 \text{ \AA}$ [172]. The rolled-up nanomembranes are rinsed in isopropanol and dried using a nitrogen gun resulting in loosely wound (spirals) or tightly wound (tubes) surfaces depending on process parameters [Fig. 3.4(b)].

The film thicknesses of GaAs and $\text{In}_{33}\text{Ga}_{67}\text{As}$ are adjusted according to (3.1) to obtain the desired tube diameter [Fig. 3.4(c), also Tab. 3.1]. The excellent agreement between experimental and analytical values illustrates reliability of the approach.

According to the purpose of acting as either curvature template or strained layer, the magnetic film is sputter-deposited after or before the rolling up process. The segmentation of the cylindrical curvature template is accomplished by focused ion beam etching (Section A.1) before metal deposition [Fig. 3.4(d)]. The load of the additional unstrained 15 nm-thick magnetic layer on top of the strained bilayer increases the resulting tube diameter by a factor of 5 to approximately $3 \mu\text{m}$. Smaller thicknesses of the magnetic layer could not be used due to the effect of HF on the magnetic properties.

3.2.2. Polycrystalline Strained Films

The crucial requirement to roll up nanomembranes, namely a lateral strain gradient normal to the surface, is not limited to epitaxially grown systems, and can also be provided in polycrystalline films deposited on sacrificial polymeric or inorganic layers [48]. Adjusting

Tab. 3.2.: *Structural parameters of rolled-up single-layer nickel nanomembranes prepared by electron beam vapor deposition with rapidly increasing deposition rate from $0.4 \text{ \AA}/s$ (d_1) to $1.5 \text{ \AA}/s$ (d_2). The strain is calculated via (3.1) assuming a homogeneous distributions.*

Thickness d_1 [nm]	Thickness d_2 [nm]	Diameter \varnothing_{exp} [μm]	Strain ε
2 ± 0.25	3 ± 0.25	1.3 ± 0.5	$(0.53 \pm 0.48)\%$
5 ± 0.5	5 ± 0.5	3 ± 0.6	$(0.44 \pm 0.31)\%$
10 ± 1.0	10 ± 1.0	7 ± 0.8	$(0.38 \pm 0.23)\%$
10 ± 1.0	20 ± 2.0	12 ± 1.0	$(0.38 \pm 0.22)\%$
10 ± 1.0	30 ± 3.0	17 ± 1.0	$(0.42 \pm 0.23)\%$

deposition rates and angles allows for engineering differential strain in polycrystalline films prepared by commonly used thermal evaporation, EBVD or sputter-deposition. In general, tube diameters in the lower micrometer range are obtained. The stack may consist of a single layer or a heterostructure with multiple functional layers, including *e.g.* magnetic, insulating and organic functionality.

Strained Magnetic Layers

Using strained magnetostrictive layers, *e.g.* Ni, Fe or Py, offers the possibility to simultaneously set tube diameter and in-plane magnetic easy axis of the tube. The rolled-up single-layer ferromagnetic nanomembranes investigated in Section 6.1 are fabricated by oblique EBVD (Plassys) onto a prepatterned rectangular sacrificial layer. The sacrificial layer can be for instance polycrystalline Ge or photoresist that are selectively dissolvable by a chemical (3% wt. H_2O_2 or NMP) not harmful to the magnetic properties of the system. The essential requirement for rolling is a rapidly increasing deposition rate to induce a strain gradient into the film with components both normal to the surface and along the incidence direction. Strain and tube diameter depend on deposition rate [$(0.4 \div 1.5) \text{ \AA}/s$], deposition angle (60° with respect to the surface normal) and thickness, and allow therefore a material independent optimization. For these conditions, an effective strain of $\varepsilon = (0.40 \pm 0.25)\%$ is derived from the relation between tube diameter and film thickness using (3.1) [Fig. 3.4(c), also Tab. 3.2]. The dashed curve plots the smallest possible tube diameter for equi-thick systems ($d_1 = d_2$). The deviations of the experimental data for large thicknesses is due to the fact that only the first 10 nm ($d_1^{max} = 10 \text{ nm}$) are deposited at low rate. Using a piezoactor to adjust the deposition rate leads to an increase of the uncertainty in thickness. The overall tendency reveals a strain (tube diameter) five

times smaller (larger) than that in epitaxial $\text{In}_{33}\text{Ga}_{67}\text{As}/\text{GaAs}$.

Strained Non-Magnetic Layers

Multilayer stacks with out-of-plane magnetic easy axis, *e.g.* Co/Pd and Co/Pt, are required to realize radially magnetized tubes (Section 7). For this sake, multilayers deposited onto strongly strained layers are rolled up into cylindrical objects. It has to be noted that even if each of the two strained films roll up well, their combination does not have to as the strain gradient can be compensated or even reversed. For instance, separately optimized Ni and Ti layers roll along the deposition direction [Fig. 3.5(a)] due to existing strain gradients in this direction. In contrast, a Ni/Ti bilayer rolls perpendicularly to the incidence direction [Fig. 3.5(b)]. With respect to strain gradients, titanium is unique as it grows under a compressive strain that transforms into tensile one after roughly 10 nm [173]. The strain is almost independent of the deposition conditions. Thus, it can be deposited in one run with Co/Pd or Co/Pt multilayer stacks *via* magnetron sputtering onto any kind of sacrificial layer. In fact, the diameters of rolled-up nanomembranes with a strained Ti layer are similar to those obtained by epitaxial strain and much smaller when rolling thick unstrained layers on top. This is due to the release of epitaxial strain in thick films by dislocation formation and the decreased efficiency for asymmetric thicknesses [see (3.1)].

To prevent collapsing of the tubes upon solvent evaporation, the rolled-up nanomembranes are loaded into a critical point dryer (CPD) filled with acetone. Liquid CO_2 is introduced at 10°C into the chamber replacing the solvent and heated up to 42°C . The CO_2 is gassed

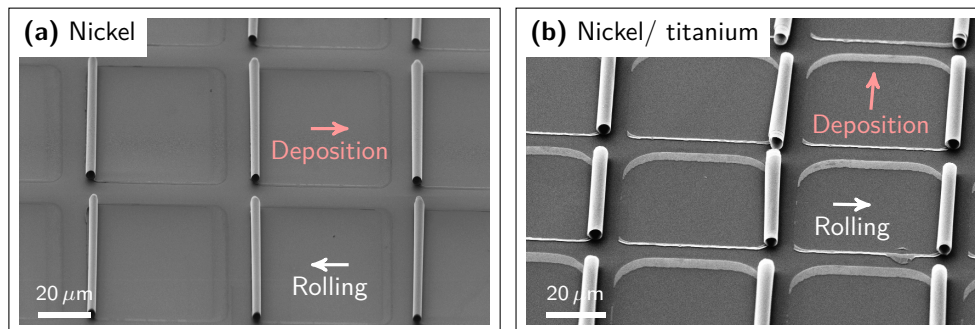


Fig. 3.5.: Altering rolling directions due to strain compensation in heterostructures. (a) Single-layer strained films, such as nickel nanomembranes, deposited under an oblique angle of 60° roll along the deposition direction. (b) Bilayers, *e.g.* nickel/ titanium, with separately optimized strain may roll perpendicularly to the deposition direction due to strain compensation at their mutual interface.

out leaving the dried tubular architectures behind. While the tube diameter is defined by the film thickness, shape, length and number of windings of the tubular structure are predetermined by lithographically patterning strained and sacrificial layers (see Appendix A.2). A lateral offset between sacrificial and strained layer provides further an anchor to the rolled-up nanomembrane. On the other hand, perfectly matching layers ensure minimal attachment to the substrate that is highly demanded for lifting tubes *via* a micromanipulator as required for magnetic tomography (Section 7).

4. Characterization Methods

In this chapter, a brief introduction to the most important characterization techniques is provided. Peculiar attention is given to emergent challenges with applying conventional methods to curved magnetic architectures. To this end, the chapter concludes with presenting the conceptual approach of magnetic soft X-ray tomography.

4.1. Kerr Microscopy

Kerr microscopy is a magnetic imaging technique based on the magneto-optical Kerr effect (MOKE), which describes the phenomenon that the polarization of electromagnetic waves is rotated by an angle θ when deflected from a magnetic media [67]. Both sign and amplitude of the rotation angle θ depend for a given material on the orientation of the magnetization with respect to the polarization of the electric field. Consequently, it provides means to sense transverse, longitudinal or out-of-plane magnetization components. A perfect disentanglement can in general not be given due to non-vanishing contributions from other components [174]. The rotation angle θ can be converted into an intensity when using two almost crossed polarizers before and after deflection from the magnetic sample, respectively. Sweeping an external magnetic field allows for recording the magnetic hysteresis curve and determining the magnetization reversal process (MOKE magnetometry). An additional objective provides means to visualize magnetic domains and their switching behavior at the microscale (Kerr microscopy, evico magnetics) [67].

The use of visible light has several implications, such as a limited spatial resolution of about 400 nm [67] and a penetration/ information depth of ≈ 20 nm for transition metals [175]. Two additional aspects have to be considered when dealing with curved magnetic architectures: a limited depth of focus and a significant loss of intensity due to large diffuse scattering from the curved surface [Fig. 4.1]. The experimental limitation of Kerr microscopy

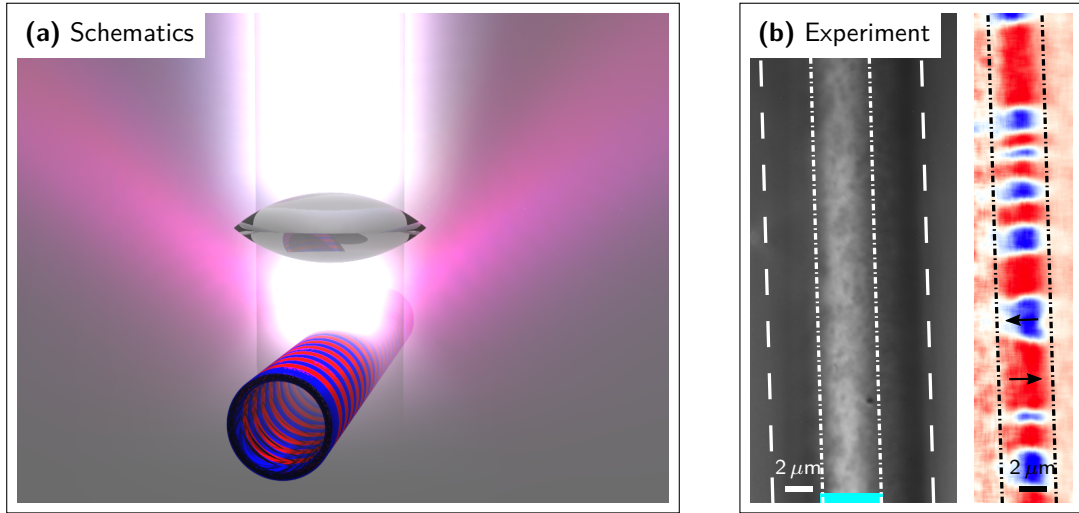


Fig. 4.1.: *Imaging of non-planar architectures in reflection geometry, such as with Kerr microscopy, meets the challenge of strongly curved surfaces and a significant amount of diffuse scattered light that cannot entirely be collected by the objective (a). (b) The magnetization in cylindrical objects with a diameter $\varnothing \approx 12 \mu\text{m}$ can only be visualized in an approximately $5 \mu\text{m}$ -wide strip on the very top.*

is demonstrated in Figure 4.1(b) using a magnetic cylindrical object with circulating magnetization [Fig. 2.10]. The magnetic contrast is confined to a narrow $\approx 5 \mu\text{m}$ -wide stripe at the very top of the tube with $\varnothing \approx 12 \mu\text{m}$. Moreover, curved free-standing nanomembranes exposed to an *ac* magnetic field as done with magnetometry are mechanically excited inducing oscillatory fluctuations in the magnetic hysteresis curves due to varying intensity of backscattered light. Although remaining an essential tool for precharacterization, MOKE magnetometry and Kerr microscopy cannot be applied to determine magnetic domain patterns in 3D objects due to the lack of information about the magnetization at the edge, the bottom or of inner regions.

4.2. Magnetic Force Microscopy

Magnetic force microscopy (MFM) [176] is a special non-contact mode of atomic force microscopy (AFM) that is sensitive to the magnetization by probing the first and second derivative of the local magnetic stray field when using magnetic monopole [177] and conventional tips (HR-MFM ML3, Team Nanotec), respectively. Operating at constant height ($z_0 \approx 20 \text{ nm}$) avoids interactions with magnetic domain patterns, such as lateral displacement of domain walls and vortex cores, and local switching. In this thesis, a

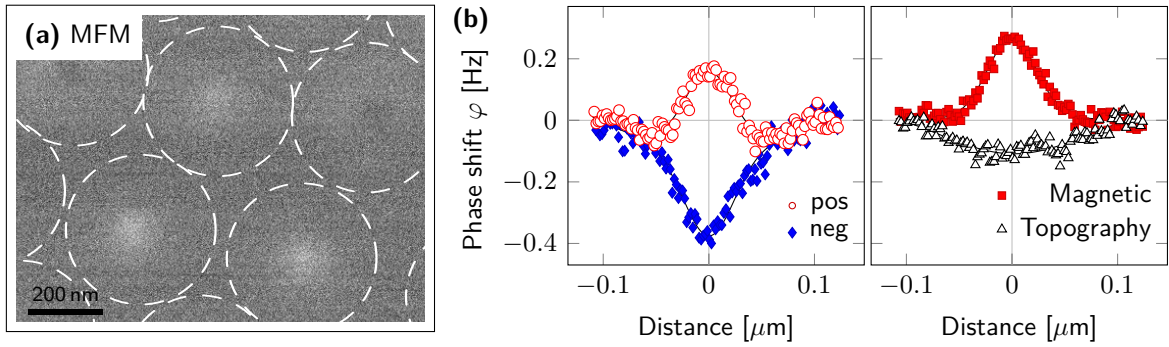


Fig. 4.2.: *Magnetic force microscopy of vortex states in hemispherical caps. (a) Bright and dark contrast in the center of the cap (indicated by white dashed circle) refers to the vortex core polarity that is randomly distributed throughout the cap array. (b) Line profiles for positive and negative polarity contain residual electrostatic contributions that are eliminated by subtraction. (Taken from [?])*

frequency-modulated MFM (HR-MFM, NanoScan) operating at high vacuum (base pressure: 10^{-6} mbar) is used. The cantilever is excited close to its normal resonance frequency while the beam deflection from the cantilever onto a 4-quadrant photodiode is acquired. The detected frequency ω of the top-minus-bottom signal deviates from the driving frequency ω_0 and in turn induces a phase shift $\varphi \approx -\frac{Q}{c} \partial_z F(z_0)$ [176] if a local force $F(z)$ is acting on the cantilever (spring constant c of the cantilever, the quality factor Q and the vertical axis z). Thus, only stray field gradients in vertical direction originating from out-of-plane magnetization and domain walls are detectable by conventional MFM. Attractive forces cause a positive phase shift (bright contrast). However, an inversion of the contrast may occur if attraction and repulsion are too strong. In order to minimize contributions from electrostatic interaction between tip and sample, an electric bias (≈ 300 V) is applied to the tip. This is particularly important when investigating curved magnetic architectures. The topography cross-talk can be minimized but not completely eliminated as exemplarily demonstrated in Figure 4.2 for magnetic vortices in hemispherical caps [Fig. 2.4].

4.3. Magnetic Soft X-ray Microscopy

Development and use of different magnetic imaging techniques are driven by the demand for measuring certain properties. In this respect, Kerr microscopy and scanning electron microscopy with polarization analyzer (SEMPA) [72, 178] visualize magnetic surface domains at the micro- and nanoscale, respectively; Spin-polarized low-energy electron micro-

scopy (SPLEEM) [179, 180] and spin-polarized scanning tunneling microscopy (SP-STM) [73, 181, 182] provide means to resolve inner structures of domain walls [24, 25, 27] and to study antiferromagnets [183, 184] and skyrmions [17–19] at an atomistic level, respectively. The enhanced spatial resolution of the latter two microscopies comes with the limitation to *in situ* characterization in ultra high vacuum and very clean (epitaxial) surfaces. Alternatively, recent advances in generating vortex electron beams with orbital angular momenta [185] pave the way towards magnetization-sensitive electron probes utilizing energy loss magnetic chiral dichroism (EMCD) [186] with electron holography (Section 2.3.2). These vortex beams are obtained as higher-order diffraction patterns after penetrating dislocation apertures [187], magnetic monopoles [188] or samples with magnetic fields aligned along the trajectory *via* the Aharonov-Bohm effect [189].

The analog of magneto-optical Kerr microscopy in the X-ray regime is magnetic X-ray microscopy that exploits the X-ray magnetic circular dichroism (XMCD, Section 4.3.1) offering elemental and chemical state specificity at the nanoscale, variable probing depth and means to follow processes at the picosecond timescale. The magnetization in antiferromagnetic media can be further monitored by utilizing X-ray magnetic linear dichroism (XMLD) [190]. The family of magnetic soft X-ray imaging consists of four techniques, *i.e.* scanning transmission X-ray microscopy (STXM) [191], full-field transmission X-ray microscopy (TXM) [192–196], X-ray photoemission electron microscopy (XPEEM) [197–200] and of lensless imaging with X-ray holography [201, 202]. The latter technique relies on coherent scattering of X-rays on domain walls and does not provide the elemental specificity known from XMCD-based approaches but offers the possibility to record ultrafast magnetization dynamics with a diffraction-limited spatial resolution (≈ 1 nm). On the other hand, TXM and XPEEM combine advantages of utilizing XMCD and recording magnetization patterns at an instance. In fact, imaging field of views of about $20 \mu\text{m}$ with a spatial resolution of ≈ 20 nm as required for magnetic X-ray tomography (MXT) (Section 4.4) is accomplished within seconds, while taking two orders longer with STXM [203].

While high-order harmonic generation (HHG) [204, 205] of X-ray beams *via* femtosecond laser pulsing of ionized atoms is a rapidly evolving field with applications to magnetic systems [206, 207], commonly used synchrotron radiation sources [208] offer convenient access to brilliant and tunable X-ray radiation with adjustable polarization. Data for this thesis were collected at the Advanced Light Source (ALS), Lawrence Berkeley National Laboratory (LBNL), in collaboration with Dr. P. Fischer using XM-1 (beamline 6.1.2) and at the Berliner Elektronenspeicherring-Gesellschaft für Synchrotronstrahlung (BESSY) II,

Helmholtz-Zentrum Berlin (HZB), in collaboration with Dr. F. Kronast using SPEEM (beamline UE49-PGM). These set-ups allow for imaging remanent states and magnetization reversal processes as well as stroboscopic laser-, field- or current-driven magnetization dynamics at the sub-nanosecond timescale. The latter one demands reversible dynamics from the state and a few-bunch (single-bunch, two-bunch or hybrid) mode with an enlarged photon intensity due to orbital quenching from the synchrotron.

4.3.1. X-ray Magnetic Circular Dichroism

Magnetic contrast in X-ray microscopies is provided by X-ray magnetic circular dichroism (XMCD). It describes the magnetization-dependent absorption of a circularly polarized X-ray beam penetrating a magnetic media [194, 209–212]. When tuning the photon energy to a prominent resonance, such as the L_3 ($2p_{3/2} \rightarrow 3d$ electric transition) and L_2 ($2p_{1/2} \rightarrow 3d$ electric transition) edges in transition metals (Ni, Fe or Co), the X-ray absorption (electron excitation) strongly depends on the relative alignment of magnetization and X-ray propagation direction (photon angular momentum/ helicity) with a maximum for collinearity [Fig. 4.3] due to Stoner split valence bands; Magnetization components perpendicular to the X-ray propagation direction are not distinguishable. It is common use to eliminate non-magnetic contributions by calculating the difference in the X-ray absorption for left- and right-circularly polarized light. Normalized by the sum of both absorptions, the XMCD signal becomes:

$$I_{\text{XMCD}} = \frac{I_{\uparrow\downarrow} - I_{\uparrow\uparrow}}{I_{\uparrow\downarrow} + I_{\uparrow\uparrow}} = \frac{I_- - I_+}{I_- + I_+}. \quad (4.1)$$

Here, $I_{\uparrow\uparrow}(I_+)$ and $I_{\uparrow\downarrow}(I_-)$ refer to absorption intensities with parallel and antiparallel alignment of magnetization and photon helicity, respectively. It is odd in magnetization and photon helicity, and reverses its sign upon switching either of them. The corresponding magnitude may reach 20% at the $L_{2,3}$ edges for transition metals due to large spin-orbit coupling [190], which is ten times larger than that of the magneto-optical Kerr effect.

The large XMCD effect at the $L_{2,3}$ edges originates from two fundamental properties [210, 211], namely conservation of angular momentum during photoelectron excitation and conservation of spin momentum during interband transition. In particular, the angular momentum of the photon is transferred to the excited photoelectron that is spin-polarized due to spin-orbit coupling. The opposite coupling for $2p_{3/2}$ ($l + s$) and $2p_{1/2}$ ($l - s$)

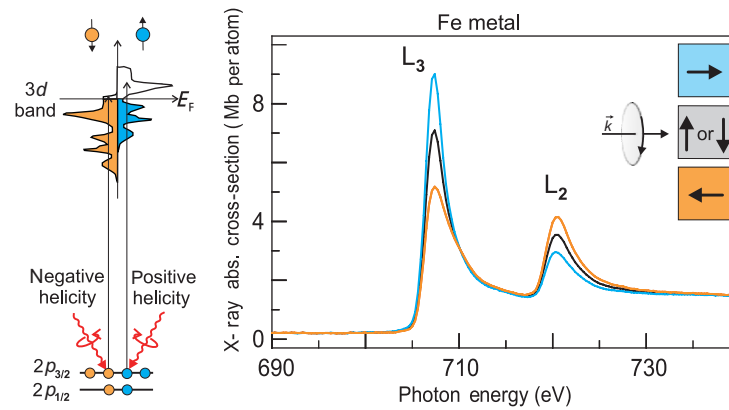


Fig. 4.3.: *The number of free valence holes in the exchange-split 3d band determines the transition probability and thus white line intensity upon resonant X-ray absorption. Using circularly polarized light allows for selectively exciting electron with minority or majority spins as reflected by the absorption spectra. Due to angular momentum transfer of the incidence photon to the excited electron, merely magnetization components along the X-ray propagation direction are distinguishable. (Taken from [190])*

causes the opposite spin polarization. The transition probability and thus the white line intensity is determined by the number of valence holes in the exchange-split 3d band. Consequently, the electron excitation with a minority spin is pronounced due to spin momentum conservation leading to an XMCD signal with opposite sign at the L_3 and L_2 edges [Fig. 4.3]. Remarkably, the difference in absorption for left- and right-circularly polarized light (or opposite magnetization directions) at the L_3 and the L_2 edge provides further means to quantitatively determine element specifically spin and orbital momenta at a local scale [210, 211] as experimentally confirmed in the pioneering work by Chen *et al.* [213].

4.3.2. Transmission Soft X-ray Microscopy

In this thesis, the full-field transmission soft X-ray microscope XM-1 at beamline 6.1.2 (ALS) [196] is used to visualize magnetic domain patterns in transparent magnetic nanomembranes. For this sake, the X-ray beam is diffracted while passing through a Fresnel condenser zone plate (CZP) and collimated after interacting with the transparent sample by an image-forming Fresnel micro zone plate (MZP) [Fig. 4.4(a)], usually consisting of circular patterns with radially alternating refraction indices and decreasing separation towards the edge [214–216]. Width of the outermost zone of the CZP, size and position of the pinhole define the energy resolution ($\lesssim 0.5$ eV), while the lateral spatial resolution ($\lesssim 20$ nm) is de-

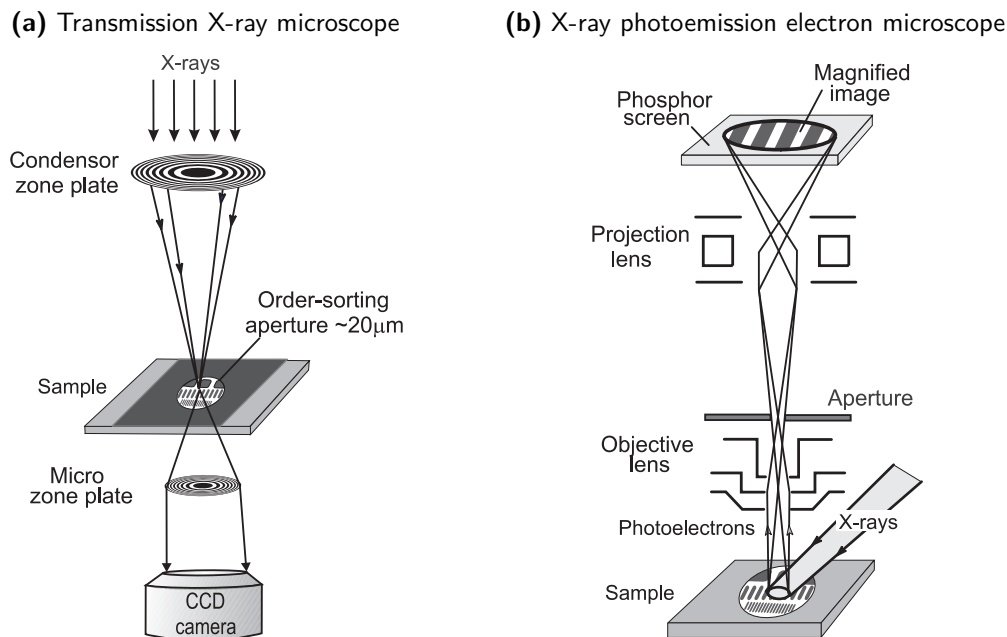


Fig. 4.4.: Schematics of (a) TXM and (b) XPEEM. (a) The incidence X-ray beam is deflected at a condenser zone plate (CZP), consisting of circular patterns with radially alternating diffraction indices and decreasing separation towards the edge. The X-ray energy is selected by adjusting the separation between CZP and sample according to the energy-dependent diffraction angle. After penetrating the transparent sample, the beam is collimated by the micro zone plate (MZP) that projects the sample onto the CCD camera. Spatial and energy resolution are determined by CZP and MZP. (b) A monochromatic X-ray beam excites secondary photoelectrons at a shallow incidence angle that are focused and collected by a PEEM. While the energy resolution is determined by the undulator, the spatial resolution is limited by the electron optics of the PEEM, size of the aperture and operation voltage. (Taken from [190])

terminated by the outermost zone width of the MZP [190, 191]. The photon energy is tuned to a prominent resonance by varying the distance between CZP/ MZP and sample due to a wavelength-dependent diffraction angle/ focal length. Thus, ordinary bending magnets with high photon yield but broad energy spectra (with respect to undulators) can be used when inserting a slit before the CZP to select the photon helicity (circular polarization) [196]. The depth of focus is about $1\mu\text{m}$. Hence, magnetic domains distributed $\lesssim 1\mu\text{m}$ along the X-ray beam propagation direction are in focus; Their contributions cannot be disentangled. Contributions originating from areas separated by more than $1\mu\text{m}$ while one region is in focus can be discriminated due to varying sharpness of domain walls and overall XMCD signal. However, this implies knowledge about the magnetic properties of the local magnetization.

The sample is mounted onto a holder at ambient conditions. Out-of-plane and in-plane

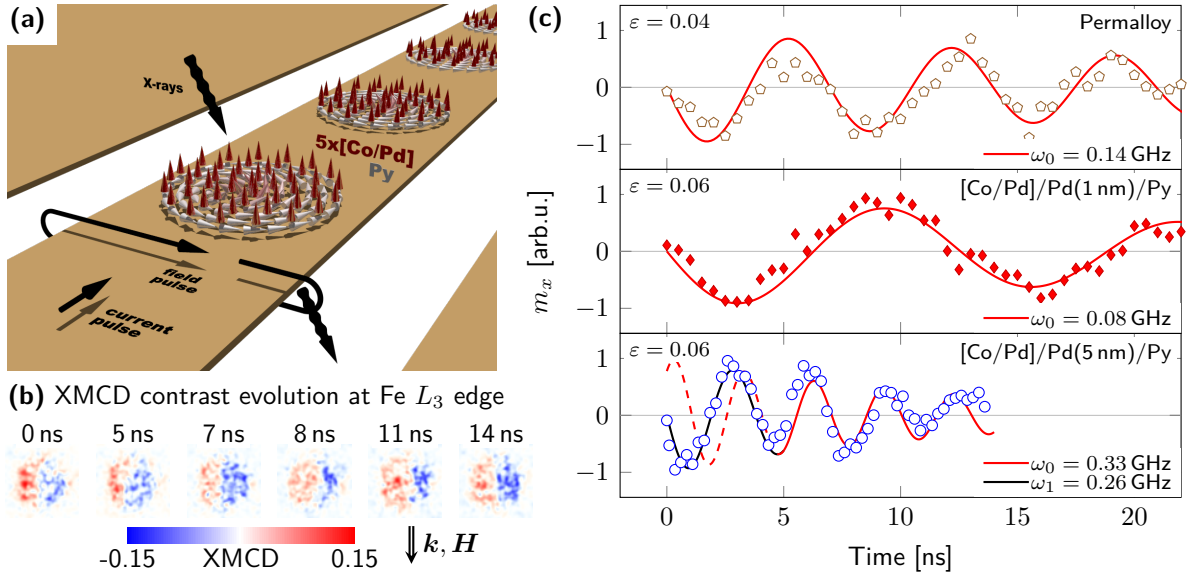


Fig. 4.5.: Stroboscopic relaxation dynamics in non-collinear spin textures visualized with MTXM. (a) Vertically stacked soft- and hard-magnetic disks prepared onto a coplanar waveguide are excited with current pulses. (b) XMCD contrast at the Fe L_3 absorption edge for various delay times after field pulse excitation. (c) Harmonic oscillation of in-plane magnetization components for pure Py(40 nm), and strongly and moderately coupled [Co/Pd]/Pd(d)/Py systems. (Taken from [217])

magnetization sensitivity is provided using sample holders with a surface normal tilted by 0° and 30° with respect to the X-ray beam propagation direction, respectively. Films are prepared on $2.5\text{ mm} \times 2.5\text{ mm}$ Si_3N_4 nanomembranes (Silson) with a thickness $d \approx 200\text{ nm}$ and a transmission $\approx 70\%$ for X-ray energies in the range $(700 \div 900)\text{ eV}$. For tomographic imaging, the complete angle range is investigated by mounting the sample with a glass capillary onto a rotation stage. For demagnetization or hysteresis measurements, magnetic fields up to $H = \pm 200\text{ kA/m}$ can be applied normal to or in the surface. Field- and current-driven magnetization dynamics can be stroboscopically studied *via* current pulse excitation using pulse generator and impedance-matched coplanar wave guides [Fig. 4.5(a)]. Figure 4.5 shows exemplarily relaxation dynamics of imprinted non-collinear spin textures [Fig. 2.4] consisting of Pd(2)/[Co(0.4)/Pd(0.7)]₅/Pd(d)/Ni₈₀Fe₂₀(40)/Pd(2) with units in nm recorded at the Fe L_3 absorption edge. Altering the interlayer exchange coupling through the Pd spacer provides means to tailor the magnetic state, including core size and corresponding mass, and thus its gyro frequency [Fig. 4.5(c)] [217]. The transition geometry implies an XMCD signal averaged over the magnetic sample along the X-ray propagation direction with a minimum and maximum magnetic film thickness to be penetrated of 2 nm and 100 nm, respectively, considering the $1/e$ X-ray absorption length of $(15 \div 20)\text{ nm}$ for

transition metals at their L_3 edge [212].

4.3.3. X-ray Photoemission Electron Microscopy

Magnetization textures in very thin films ($d \approx 2$ nm) are visualized by the surface sensitive XPEEM at beamline UE49-PGM (BESSY II) [200]. The set-up consists of a commercial spin-polarized PEEM (PEEM III with analyzer, Elmitec) with a spatial resolution of ≈ 30 nm and a variable field of view in the range ($3 \div 50$) μm . As the incidence angle of the X-rays is fixed to 74° with respect to surface normal, only one magnetization component can be accessed. Photoelectrons are resonantly excited while exposing the sample to a linearly or circularly polarized X-ray beam generated by an undulator with an energy resolution $\lesssim 0.2$ eV [Fig. 4.4(b)]. The number of emanating photoelectrons, *i.e.* secondary electrons, is directly proportional to the X-ray absorption at the L_3 or L_2 edge [218] and may analogously serve to visualize the magnetization based on XMCD. The normalization to the intensity of absorbed X-rays is particularly attractive for very thin films as much larger signal-to-noise ratios compared to MTXM can be obtained. The penetration/ information depth is determined by screening effects due to Auger electrons created after core excitation (secondary electron emanation) and is limited to ($5 \div 10$) nm at resonance in transition metals [212]. Small variations in the secondary electron momentum normal to the surface, originating from local modifications of the work function, electrostatic charging or topography, are accessible by tuning the start voltage. This means that contributions from regions with different surface normal as occurring on curved surfaces can be pronounced or compensated by adjusting the start voltage.

The sample, floating at ($5 \div 20$) kV to accelerate the photoelectrons, is mounted onto a rotation stage that is in contact with a thermal bath of variable temperature $T = (50 \div 400)$ K. External magnetic fields up to $H = \pm 40$ kA/m may be applied parallel or normal to the sample surface allowing for in-field measurements. Recording images while applying a magnetic field requires to readjust alignments at each measurement point, since the photoelectrons are deflected due to the Lorentz force. Studies of global and local ground states by thermal demagnetization [163], coupling between plasmons and magnetization [219, 220] as well as all-optical switching processes in transition metal-rare earth compounds [221, 222] can be carried out by applying femtosecond laser pulses with variable polarization.

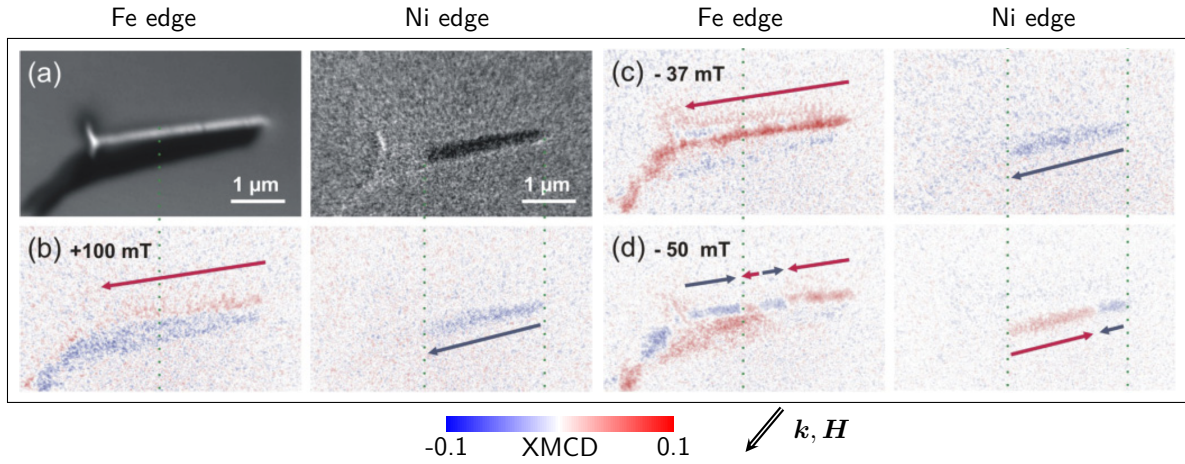


Fig. 4.6.: Magnetization configurations in core-shell wires consisting of Ni (core) and Fe_3O_4 (shell) recorded with XPEEM in transmission geometry. (a) PEEM contrasts taken at the Ni and Fe L_3 edge, respectively. No direct contrast is observed from the inner Ni core. (b)–(d) Remanent states after applying an in-plane magnetic field along the X-ray propagation direction. Red and blue arrows indicate the magnetization component along the wire. (Taken from [223])

4.3.4. Transmission X-ray Photoemission Electron Microscopy

The shallow incidence angle of the X-ray beam provides further means to investigate transparent 3D magnetic nanostructure in transmission geometry (T-XPEEM) with an enhanced lateral resolution along the X-ray propagation direction [65, 85, 137, 223, 224]. An early work using T-XPEEM to resolve the magnetization configuration in magnetic core-shell nanowires consisting of Ni (core) and Fe_3O_4 (shell) is shown in Figure 4.6. While neither elemental nor XMCD contrast is directly observed from the inner Ni structure, information may be extracted from the shadow region.

The XMCD signal is retrieved from the projected pattern in the shadow region on top of planar substrate, which serves as a detecting screen [Fig. 4.7]. In this respect, magnetization textures in on-chip magnetic devices for sensing or storage applications may be visualized without the need to prepare them on or transfer them to Si_3N_4 nanomembranes as required for MTXM investigations. The vertical lift of the magnetic architecture is achieved for planar patterns by underetching and pillow formation [Fig. 4.7(a)] or naturally provided by 3D curved magnetic architectures, such as magnetic cap structures [Fig. 4.7(b)] or magnetic tubes [Fig. 4.7(c)]. While penetrating the nanostructure, the circularly polarized X-ray beam is attenuated according to magnetization and XMCD effect.

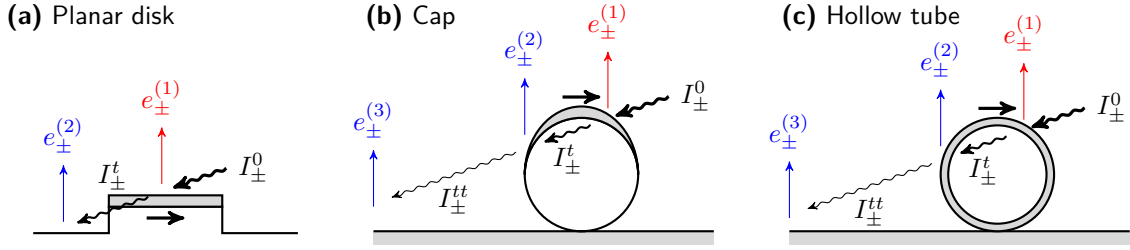


Fig. 4.7.: *Illumination at a shallow incidence angle allows for imaging magnetic domain patterns in transmission geometry with XPEEM. (a) Planar patterns have to be prepared on top of a pillow. 3D magnetic architectures, such as (b) cap structures and (c) cylindrical objects, possess intrinsically the required vertical shift. At the first penetration, left- and right-circularly polarized X-ray beams are attenuated according to the XMCD effect leading to the emanation of photoelectrons $e_{\pm}^{(1)}$. The intensity difference between the two X-ray beams induce at the back side of the architectures a shadow contrast that with a modified XMCD signal ($e_{\pm}^{(2)}$, $e_{\pm}^{(3)}$). The degree of modification depends on the thickness of the first penetration event and may reduce, compensate or even invert the XMCD contrast. (Taken from [85])*

Photoelectrons are excited and detected in a conventional way with XPEEM:

$$e_{\pm}^{(1)} \propto I_{\pm}^{(1)} = I_{\pm}^0 \left[1 - \exp\left(-\mu_{\pm}^{(1)} d^{(1)}\right) \right]. \quad (4.2)$$

Here, $\mu_{\pm}^{(j)}$ and $d^{(j)}$ are X-ray absorption coefficient and thickness of the assumed uniformly magnetized film, respectively. Note that the detected photoelectron intensity $e_{\pm}^{(1)}$ is proportional, not equal, to the X-ray absorption intensity $I_{\pm}^{(1)}$. The intensity of the transmitting X-ray beam is reduced by the X-ray absorption intensity. Consequently, a further resonant excitation leads for the same magnetization to a different XMCD signal, which may be reduced, compensated or even reversed according to the thickness $d^{(1)}$ of the magnetic layer according to:

$$e_{\pm}^{(2)} \propto I_{\pm}^{(2)} = I_{\pm}^0 \exp\left(-\mu_{\pm}^{(1)} d^{(1)}\right) \cdot \left[1 - \exp\left(-\mu_{\pm}^{(2)} d^{(2)}\right) \right]. \quad (4.3)$$

For instance, a magnetic film with a thickness $d^{(1)} \approx 20$ nm shows a reversed magnetic contrast at the back side of the cap [83, 85], while a 2 nm-thick magnetic film does not reveal an obvious contrast change [115].

Following this approach, inner magnetization textures, including domain walls [223, 224] and domain patterns [65, 137] in magnetic rods and rolled-up magnetic nanomembranes with cylindrical shape, respectively, were revealed. The expansion of the application field of XPEEM provided by T-XPEEM from planar 2D surface magnetization patterns to 3D objects and magnetic domains hidden to conventional XPEEM due to surface-sensitivity is

not only attractive with respect to fundamental research, but also for application-relevant performance checks of on-chip devices.

4.4. Magnetic Soft X-ray Tomography

The possibility to perform magnetization-sensitive transmission experiments with MTXM and T-XPEEM paves the way towards the development of magnetic soft X-ray tomography (MXT) [65]. Tomographic imaging is based on two steps: (i) recording the 2D projections of beam attenuation while penetrating the sample at various rotation angles; and (ii) reconstructing the 3D spatial distribution from the set of 2D projections [144]. Figure 4.8 illustrates by comparison with conventional scalar tomography [Fig. 4.8(a)] challenges with developing MXT [Fig. 4.8(b)] originating from different contrast mechanisms. X-ray tomography generates a map of the X-ray absorption in the 2D projection images due to the interaction with charges, *i.e.* a scalar density distribution. A scalar density distribution at a certain location contributes by the same amount for each projection angle [Fig. 4.8(c)]. Inhomogeneous density distributions may be considered as assemblies of homogeneous elements and reconstructed accordingly.

Applying conventional scalar tomography reconstruction algorithms to retrieve the three-dimensional magnetization meets the fundamental challenge of canceling out the XMCD signal. This is because the XMCD signal contains information about the projection of the magnetization vector onto the X-ray beam propagation direction, which leads to an angle-dependent signal contribution of the same magnetization vector [Fig. 4.8(d)]. Red and blue contrast refer to magnetization vectors with the same amplitude but opposite direction. The absence of a net XMCD contrast is indicated by white. In case of a nonuniform magnetization distribution, the vector property-induced non-additivity of the XMCD signal causes a complex ambiguous projection of the 3D magnetization. Considering the simplest case of two identical macrospins aligned antiparallel to each other *e.g.* at the front and back side of a radially magnetized thin tube [134], reflects the problem of non-additivity of the XMCD contrast as follow [Figs. 4.8(e), 4.8(f)]: The projections along and perpendicular to the magnetization vector become zero due to net moment compensation and zero projection onto the X-ray propagation direction, respectively. Merely an illumination at *e.g.* $\sim 45^\circ$ results in a nonzero signal that constitutes of a reddish and bluish contribution with an angle-dependent order. Accordingly, two macrospins point-

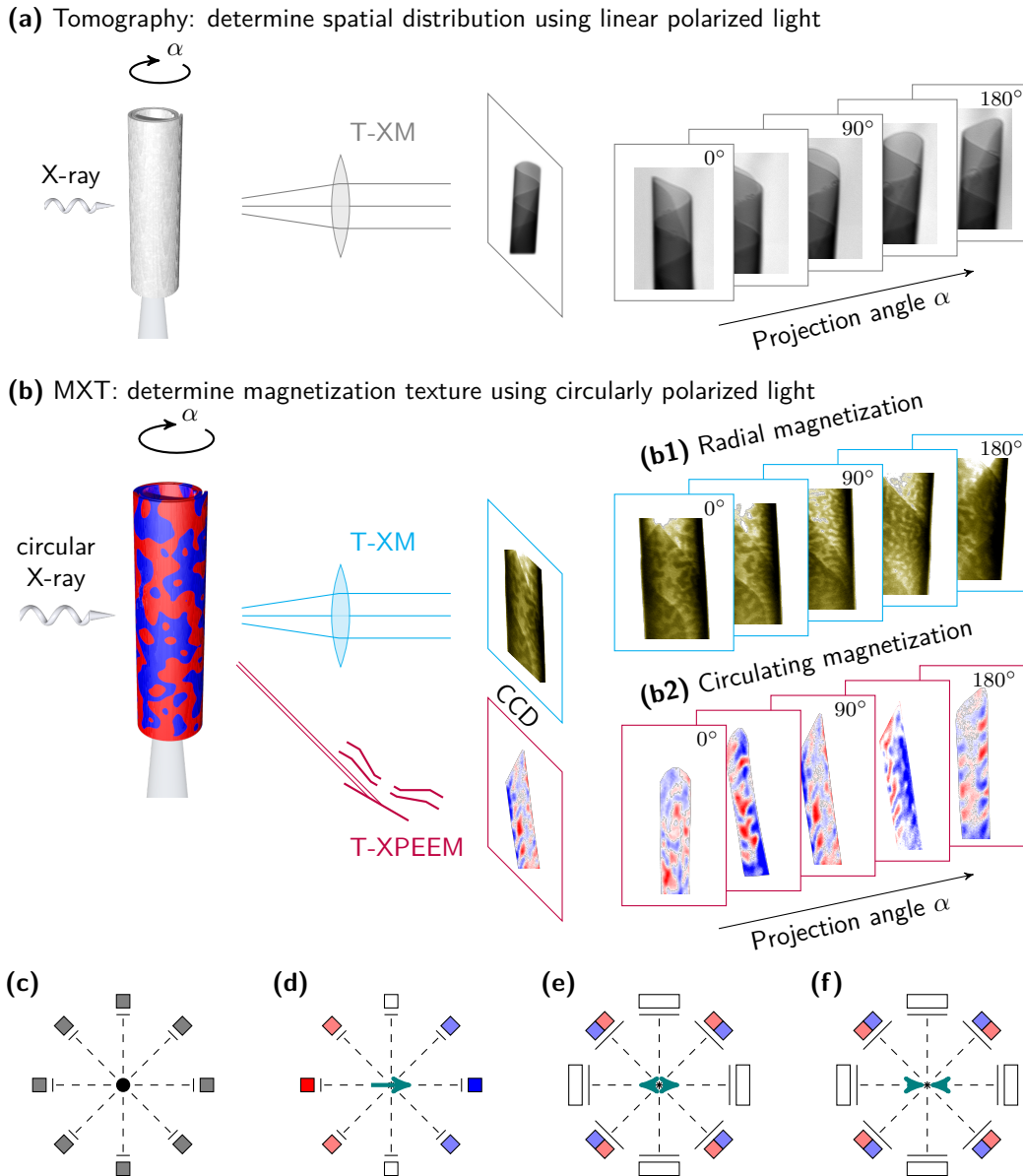


Fig. 4.8.: Comparison of the conceptual difference between (a) conventional scalar tomography and (b) magnetic X-ray tomography (MXT). (a) Light is attenuated when penetrating an object, e.g. tubular magnetic nanomembrane, according to its atomic mass distribution and angle-independently (c). The spatial distribution in 3D space is obtained from a set of 2D projections ranging from 0° to 180° . (b) Utilizing XMCD, the magnetization component along the beam propagation direction is visualized in (b1) radially and (b2) in-plane magnetized tubular architectures. (d) The XMCD signal shows an angular dependence that even reverses its sign for space-inverted X-ray propagation (red to blue, vice versa). White refers to a vanishing net XMCD signal. The corresponding underdetermined system of projections leads to an ambiguity of possible reconstruction when considering arrangements of two or more macrospins (e), (f) that may only be released by analyzing their evolution with varying projection angle. Determining all magnetization vector components requires to record projections around several rotation axes. Tubular surfaces with either radial or in-plane magnetization allow for retrieving the magnetization textures from one set of projections taken around a rotation axis that coincides with the symmetry axis. (Taken from [65])

ing away from or towards each other can be disentangled. The same projections are also obtained when considering the reversed by 90° rotated case [compare Figs. 4.8(f), 4.8(i) and 4.8(g), 4.8(h)]. The angle dependence of these pairs in the range from *e.g.* 0° to 45° is different and could be used for discrimination. Analyzing the contrast evolution with varying projection angle constitutes the idea of MXT. Note that a complete and consistent identification of the magnetization texture requires to record the XMCD contrast around several projection axes and to determine the contrast change, which refers to the derivative of the magnetization vector with respect to the rotation. In contrast to vector field electron tomography, it is generally not sufficient to consider only two projection axes when dealing with nonuniform states due to a possible XMCD contrast compensation and locally varying saturation magnetization.

In extended samples with a rotation axis not coinciding with the local direction of the magnetization vector, the X-ray beam interacts at each projection angle with another pair of macrospins. This ambiguity requires (i) to derive valid restriction conditions, such as a spatial confinement of the magnetization vector field by locating the magnetic material using conventional scalar X-ray tomography, (ii) to retrieve additional information on the preferential magnetization orientation, which can be derived *e.g.* from the integral magnetic character and (iii) to analyze the evolution of the XMCD signal as a function of the projection angle. A profound understanding of the generated XMCD signal including the identification of measurement artifacts and the support of XMCD contrast simulations are essential ingredients to perform MXT.

5. Magnetic Cap Structures

Magnetic cap structures are 2D curved surfaces with rotation (hemispherical) or mirror (cylindrical) symmetry and represent the simplest class of 3D objects discussed in this thesis. The curvature-driven thickness gradient modifies magnetostatic contributions that in turn improve the stabilization of magnetic vortices in soft-magnetic closely packed caps providing means to imprint non-collinear spin textures. Both individual cap structures and closely packed cap arrays are investigated for the sake of exploring vortices in curved surfaces, designing magnetic self-propelled Janus particles for drug delivery and investigating coupling phenomena. Successful imaging and proper contrast interpretation of magnetic domains in these curved systems are essential requirements for characterization and further application to more complex systems. *Results shown in this chapter are summarized in References [83–85, 115, 128, 129, 217?].*

5.1. Hemispherical Permalloy Caps

The soft-magnetic cap structures with hemispherical geometry are prepared by sputter-depositing Permalloy (Py, Ni₈₀Fe₂₀) sandwiched by Ta capping (2 nm) and buffer (5 nm) layers onto assemblies of non-magnetic spherical particles. Following the procedure presented in Section 3.1, various arrangements of cap structures are obtained, including individual caps, pairs and closely packed cap arrays with hexagonal symmetry. Py film thickness and sphere diameter are varied in the range $d = (10 \div 40)$ nm and $\varnothing = (50 \div 800)$ nm, respectively. The notation used to address caps with a film thickness d and a diameter \varnothing is Py(d/\varnothing) with units in nm. The film possesses a thickness gradient due to an effectively varying deposition angle induced by the curvature [Fig. 3.1(b)]; The given parameter refers to the thickness at the very center of the cap. Depending on sphere diameter and film thickness, magnetic layers in closely packed cap arrays are either modulated in thick-

ness or even separated, which in turn provides means to tailor magnetic exchange and magnetostatic interactions.

5.1.1. Imaging Magnetic Remanent States

The magnetic domain patterns are visualized utilizing X-ray magnetic circular dichroism (XMCD, Section 4.3.1) with transmission X-ray photoemission electron microscopy (TXPEEM, Section 4.3.4). For this sake, left- and right-circularly polarized X-rays with an energy equal to the nickel L_3 absorption edge illuminate the sample at an angle of 74° with respect to the surface normal. The shallow incidence angle causes for transparent thin films with a vertical offset a shadow contrast at the back side of the structure [Fig. 4.7]. This effect is firstly demonstrated on a 20 nm-thick planar Py disk with a diameter $\varnothing = (300 \pm 10)$ nm patterned by electron beam lithography (in collaboration with Dr. J.I. Mönch). Using reactive ion etching (RIE), both surrounding films and parts of the Si substrate were smoothly removed. The XMCD signal of the resulting disk on a pillow (indicated by dashed circle) reveals the dipolar contrast of a magnetic vortex state in the disk [225] and an inverted XMCD contrast in the shadow region [Fig. 5.1(a)]. The contrast inversion in the shadow region originates from the attenuation of the X-ray beams while penetrating the disk according to the XMCD effect and different photoelectron excitation intensities on the substrate (Section 4.3.4). The lateral dimensions of direct and XMCD shadow contrast are similar as the disk is parallel to the substrate.

Individual Caps

The XMCD contrast of 3D magnetic objects is more complex than that of planar architectures due to multiple interactions with various magnetization orientations. In other words, the detected XMCD signal represents a net value with an enhanced, reduced, compensated or even inverted contrast (Section 4.3.4). For instance, the XMCD signal of magnetic caps with a film thickness $d = 20$ nm and a diameter down to 100 nm (indicated by dashed circles) exhibits a quadrupole-like pattern accompanied by an inverted shadow contrast [Fig. 5.1(b)] [85]. The origin of the quadrupole XMCD contrast is of the same nature as the shadow contrast, namely a photoelectron excitation with circularly polarized light with distinct intensities. The XMCD contrast at the back side of the cap is weaker than

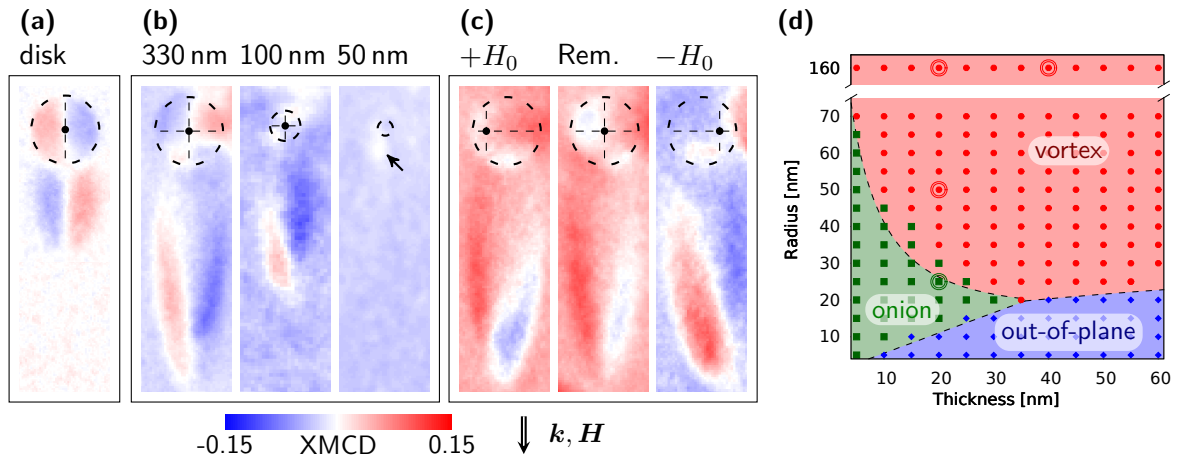


Fig. 5.1.: *Magnetic domain patterns in individual hemispherical Py caps visualized by T-XPEEM. (a) Magnetic vortex in a planar disk on top of a pillow causes a dipolar XMCD contrast in the disk and an inverted shadow contrast at the back side. (b) The curvature of the cap leads to a quadrupole-like contrast due to interactions with front and back side and an extended shadow contrast. The shadow contrast can be used (b) to identify magnetic states below the spatial resolution limit or (c) to observe core displacements ($H_0 = 12$ kA/m) and even dynamics. (d) Numerically determined phase diagram of magnetic equilibrium states in caps (symbols) and disks (shaded areas) with inserted experimental data (double circle). (Taken from [85])*

that of the front side due to competing contributions. It is not compensated because of a significantly larger X-ray absorption during the first penetration due to thickness gradient and incidence angle. A non-zero background contrast is apparent as the surrounding planar substrate is also covered with the magnetic film. The peculiar fingerprint of magnetic vortices in cap structures is proven by applying an external magnetic field parallel to the X-ray propagation direction and recording the displacement of the vortex core perpendicular to the field direction [Fig. 5.1(c)]. In this respect, the unlikely event of an antivortex stabilization in cap structures possessing a similar quadrupole-like contrast in planar geometry can be excluded. The shallow angle illumination in T-XPEEM enlarges the XMCD signal of the cap structures along the X-ray propagation direction by a factor of ≈ 3.5 ($= \tan 16^\circ$). Additionally, the shadow contrast suffers less from local field distortions caused by the cap itself and can be used to determine the vortex core location or to identify magnetic states in caps below the resolution limit as exemplarily shown for caps with a diameter $\varnothing = 50$ nm [Fig. 5.1(b)]. Although no signal was detected from the cap structure, the monochrome shadow contrast (pointing arrow) provided information about the onion state [83]. Note that the contrast analysis of such simple spin textures, *i.e.* vortex state, onion state, *et cetera*, is carried out without performing XMCD contrast simulations as required for more complex magnetization textures (Sections 6.2 & 7.1).

The accordingly retrieved magnetic remanent states are checked against the phase diagram calculated for an extruded hemisphere with an inner and outer radius R and a constant thickness d using OOMMF [226] (in collaboration with Dr. V.P. Kravchuk) and typical material parameters of Py (exchange constant $A = 13$ pJ/m, saturation magnetization $M_S = 860$ kA/m, damping constant $\eta = 0.01$) [85]. Simulating the remanent states with initial onion, vortex and out-of-plane magnetization and calculating the corresponding energy minima provided means to determine the ground state with the lowest energy minimum [Fig. 5.1(d)]. The experimental data is indicated by double circles (red: vortex state, green: onion state), which agree well with the theory. The importance of exploring the XMCD shadow contrast is obvious, since otherwise no information could have been found about the boundary region. Overlaying the obtained phase diagram of a cap with that of planar disks (dashed boundary lines) [227] demonstrates a similar dependence for individual specimen. However, magnetization texture and thus magnetostatic interaction are distinct particularly for the onion state due to a modified geometry [85].

Closely Packed Cap Arrays

Keeping the peculiar XMCD contrast of magnetic vortices in mind, magnetic domain patterns in closely packed cap arrays with hexagonal symmetry are visualized and analyzed in a similar manner. In this case, the shadow contrast depends on both magnetic state and lattice orientation (orientation of the structural domain) with respect to the X-ray propagation direction. Figures 5.2(a) and (b) depict the remanent states of closely packed Py(40/330) cap arrays initially saturated by an in-plane magnetic field oriented 4° and -20° with respect to the lattice orientation, respectively. Each cap exhibiting a quadrupole XMCD contrast is indicated by red and green circles referring to clockwise and counterclockwise circulation, respectively. The vortex circulation assemble to characteristic patterns, such as straights and steps, depending only on the lattice orientation as the magnetic properties of individual caps are isotropic. Analyzing its distribution for the two given lattice orientations, reveals a majority of straights and steps for alignments close to 0° and 30° , respectively [Figs. 5.2(a), 5.2(b)]. As the occurrence of such circulation patterns relies on the tailored magnetostatic interaction between adjacent caps, a periodic alternation at the local scale is observed. Both arrangements represent the ground state with four nearest neighbors having opposite circulation for the corresponding array orientation [Fig. 5.2(c)]. Contrary to honeycomb lattices, three-fold arrangement are less favored in closely packed hexagonal arrays, though sometimes observed, because

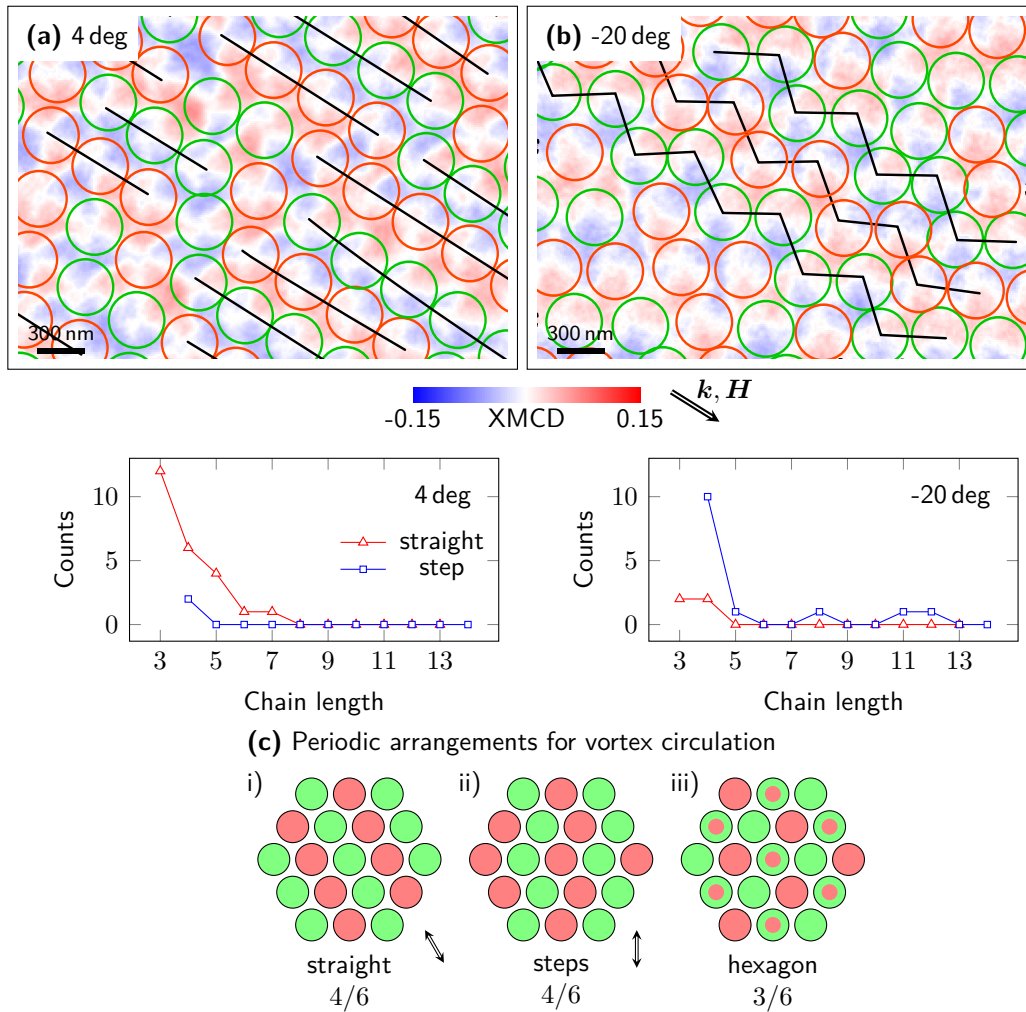


Fig. 5.2.: Vortex circulation patterns in closely packed Py(40/330) cap arrays. Remanent states after initially saturating with an in-plane magnetic field along (a) 4° and (b) -20° with respect to the lattice orientation. The vortex circulation is indicated by red and green circles. Analyzing the occurrence of straights and steps reveals an angle dependence and a non-vanishing vortex circulation coupling. (c) Possible periodic arrangement of circulation-coupled vortices in hexagonal arrays. The original saturation direction is indicated by arrows. Straights and steps represent the lowest ground state with 4 of 6 nearest neighbors matching alternating circulation. Hexagons observed in honeycomb lattices are less preferable. (Taken from [?])

merely half of nearest neighbors match the circulation. Note that such an investigation of circulation frustration is not possible using planar disks since the vortex state is not a remanent state in closely packed planar disks due to an emergent anisotropy originating from magnetostatic interactions between adjacent disks along the lattice vectors during the magnetization reversal of onion states [228, 229].

However, these considerations only apply to collective transitions since the system is not frustrated at remanence due to negligible stray fields. An applied magnetic field induces a preferential magnetization orientation parallel to the field direction even if the field value approaches zero. Vortices nucleate pairwise with opposite circulation at the edge of caps perpendicular to the external magnetic field. In this respect, the density of periodic patterns (relative coverage) can be used to estimate the correlation length in units of caps during vortex nucleation. For an array orientation of 4° , the correlation length at room temperature is four caps [Fig. 5.2(a)]. 57% of all caps are embedded by four caps with a matching circulation; 25% have three nearest neighbors with opposite circulation, independently of the crystal orientation. This indicates that roughly 40% of all caps are located at the grain boundaries. The coupling strength is too small to ensure a long-range arrangement of circulation at room temperature. A similar trend is observed for crystal orientations close to 30° and steps that appear to be more stable (longer) due to a more efficient coupling during nucleation. This causes locally chains of more than 10 entities at room temperature [Fig. 5.2(b)].

In order to resolve the vortex polarity and to address a possible topologically driven circulation-polarity coupling in hemispherical caps as predicted for curved magnetic surfaces resembling spherical shells [34], frequency-modulated magnetic force microscopy (MFM) is applied (Section 4.2). A typical MFM contrast of closely packed vortices ($t = 40$ nm, $\varnothing = 330$ nm) with bright and dark regions corresponding to the vortex core in the center of the cap (indicated by dashed circle) is depicted in Figure 4.2(a). Positive or negative charged core surfaces are distributed evenly in a random manner in spite of well-defined circulation patterns suggesting an absent circulation-polarity coupling. The profiles of positive (bright) and negative (dark) polarity are shown in Figure 4.2(b). All positive and negative profiles reveal the same shape with a FWHM of (46 ± 2) nm. Note that this value includes the convolution of the magnetic tip, which cannot unambiguously be deconvoluted due to the complexity of the magnetic structure of the vortex core and the interaction of the tip with the vortex itself.

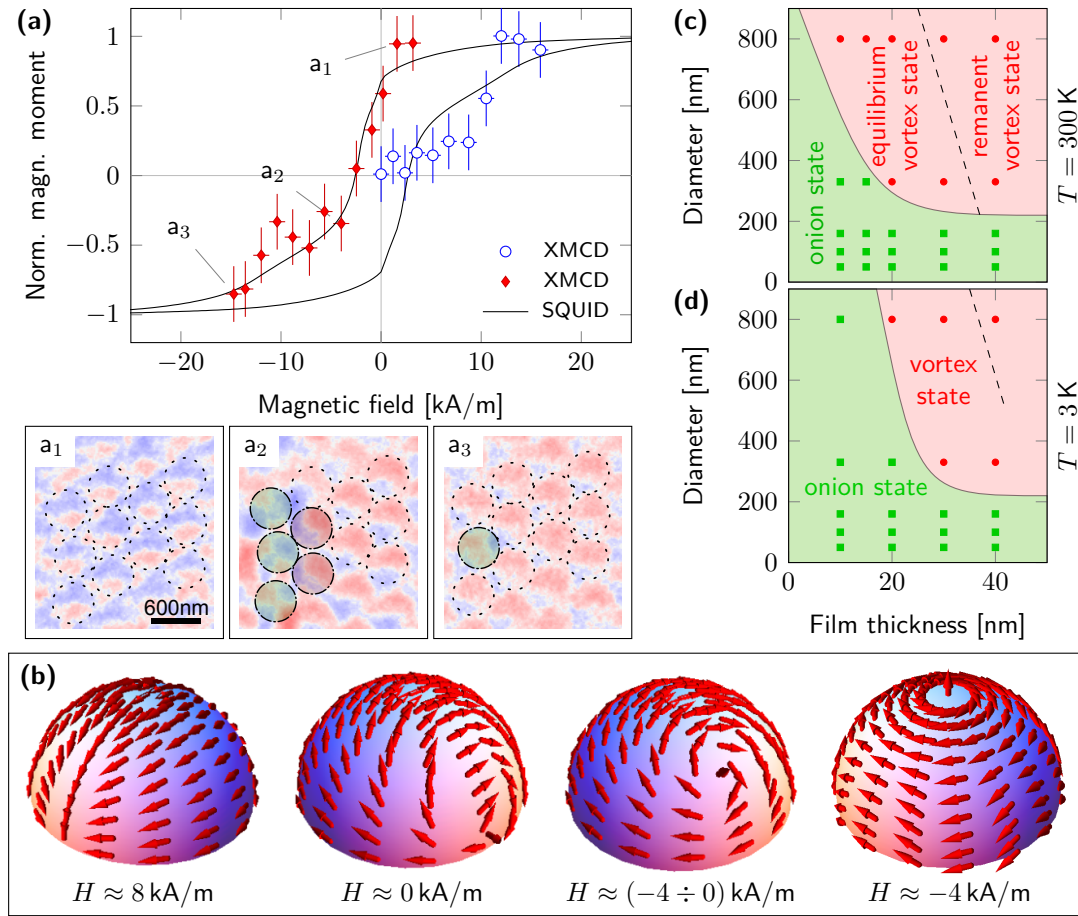


Fig. 5.3.: (a) Magnetization reversal of closely packed Py(20/330) caps (indicated by dashed circles) visualized by XPEEM. The images a_1 , a_2 and a_3 illustrate remanent, transition and saturation state, respectively. Caps that exhibit vortex states are indicated by $\cdot -$. The XMCD hysteresis curves are averaged over the front side of these vortices. The SQUID hysteresis loop is plotted as reference (solid). (b) Schematics of onion and vortex states exposed to in-plane magnetic fields. Panels (c) and (d) show the phase diagrams derived from the SQUID hysteresis loops at $T = 300$ K and $T = 3$ K, respectively. Boundary lines are shown as a guide to the eye. (Taken from (a), (b): [83]; (c): [?])

5.1.2. Magnetization Reversal

Magnetic Hysteresis and Phase Diagram

To verify the statement of intercap interactions during the vortex nucleation process selecting the circulation, the magnetic states are imaged while ramping an in-plane magnetic field. Using Py(20/330) cap arrays, the magnetostatic stray field contributions are significantly reduced compared to the aforementioned system [Py(40/330)] due to smaller volume

divergences (2.3), apparent by a large number of onion states and local vortex nucleation [Fig. 5.3(a)]. In the given example, the magnetostatic interaction is sufficiently large to nucleate vortices along two straights with opposite circulation but too weak to influence them at the opposite edge of the cap. The virgin curve extracted from the front side of the cap undergoing a vortex nucleation is shown in Figure 5.3(a) as blue symbols and reveals a transition at $H_{an} = (11.5 \pm 1.5)$ kA/m. This value matches very well the vortex annihilation field derived from the local maximum of the susceptibility $H_{an} = (12.0 \pm 0.8)$ kA/m that were obtained by superconducting quantum interference device (SQUID) measurements. Because SQUID averages the hysteresis loops over hundreds of structural domains with varying lattice orientations, this also implies a magnetization reversal process independent of the lattice orientation. After saturation the magnetic field is swept to monitor the magnetization reversal process [Fig. 5.3(a), red symbols].

The image sequence (a_1, a_2, a_3) shows the evolution of the magnetic pattern from a dipolar XMCD contrast in a single cap (onion state) into a coexistence of dipolar and quadrupole-like XMCD contrast distributed throughout the cap array. The corresponding magnetization configurations of onion and vortex states are shown as schematics in Figure 5.3(b). Both hysteresis curve and XPEEM patterns can be understood by means of micromagnetic simulations [83]. Accordingly, the slow decrease of the XMCD signal at positive field corresponds to the relaxation of the magnetization into the surface plane forming the onion state. The irreversible magnetic transition is initiated by the transformation of the onion into the metastable C-state, apparent in the hysteresis curve by a constant permeability [slope in Fig. 5.3(a)]. In cap arrays, the opening of the C-state is set by lattice orientation and neighboring caps predetermining vortex circulation patterns. With decreasing field the vortex core nucleates at the edge of the cap in order to minimize the stray field. As the external magnetic field becomes more negative, the core is shifted to the center. For even more negative fields, the core is displaced to the opposite edge with respect to the nucleation site and eventually expelled from the cap.

The phase diagrams for $T = 300$ K and $T = 3$ K are assembled by analyzing magnetic hysteresis loops acquired by SQUID magnetometry [Figs. 5.3(c), 5.3(d)]. The same magnetic hysteresis loops were also obtained at $T = 300$ K by alternating gradient magnetometry (AGM) and magneto-optical Kerr effect (MOKE) magnetometry. The solid lines separating the two phases, vortex and onion state, are given as a guide to the eye. The dashed line within the vortex phase illustrates the boundary above which the remanent vortex state occurs. Due to the limited number of possible magnetic domain patterns, the transition states

during magnetization reversal coincide with the equilibrium magnetization configuration that may differ from the remanent states, and can therefore be derived from the hysteresis loops [83]. Decreasing the diameter from 800 to 330 nm increases the vortex annihilation field, which can be referred to as an enhancement of the vortex stability. However, further decrease results in suppression of vortex nucleation in cap arrays. Instead, a rotation of the magnetization in the onion state takes place during reversal [83]. On the other hand, the vortex becomes less stable (smaller annihilation and nucleation fields) with decreasing Py thickness while keeping the diameter unchanged and is finally suppressed completely. Both trends can be understood by the decrease of the aspect ratio, the quotient of film thickness and particle diameter. For small aspect ratios, particularly the magnetic volume charges become small. As those contributions are the main driving force for stabilizing the vortex state, samples with small aspect ratio exhibit the onion state, as experimentally observed. Note that this simple argument cannot be applied to samples with small diameters, since the interaction between adjacent caps increases significantly as known from planar disk arrays [228]. Comparing the experimental phase diagram for closely packed cap arrays with the numerically determined one for single caps [Fig. 5.1(d)] reveals an expanded onion phase due to magnetostatic intercap interaction during the vortex nucleation process. The third phase with out-of-plane magnetization for large aspect ratios is absent in closely packed cap arrays due to the formation of a thickness modulated extended film instead of individual caps favoring the onion state.

Temperature Dependence of Annihilation and Nucleation Fields

The thermal activation of the vortex core nucleation at the edge decreases with decreasing temperature, which leads to an expansion of the onion state towards large thicknesses and diameters [Figs. 5.3(b), 5.3(c)]. To address this trend in more detail, the temperature dependence of vortex annihilation and nucleation fields for Py(40/330) cap arrays is shown in Figures 5.4(a) and (b), respectively. For high temperatures ($T > 100$ K), the slope originates from the temperature dependence of the saturation magnetization due to spin wave excitation (Bloch's law) that can be fitted by:

$$H_{an/n}(T) = H_{an/n}(0) \left(1 + \alpha_{an/n} T^{3/2}\right). \quad (5.1)$$

The fitting parameters $\alpha_{n/an}$ shown in Table 5.1 are one order of magnitude larger than those of individual planar disks [230]. The saturation magnetization measured at 24 kA/m

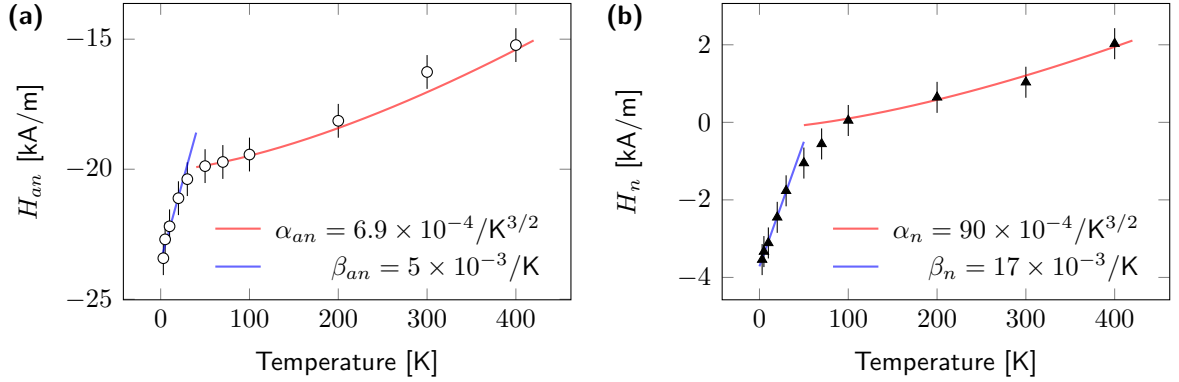


Fig. 5.4.: Temperature dependence of (a) vortex annihilation and (b) nucleation fields of closely packed Py(40/330) caps recorded by SQUID magnetometry. High ($T > 100$ K) and low ($T < 50$ K) temperature ranges are fitted via (5.1) and (5.2) accounting for spin wave excitations and thermal activation, respectively. (Taken from [83])

as a function of the temperature is fitted by $M_S(T) = M_S(0) (1 - c_1 T^{3/2} - c_2 T^2)$ with $c_1 = 3.65 \times 10^{-6} \text{K}^{-3/2}$ and $c_2 = 1.41 \times 10^{-7} \text{K}^{-2}$. Such an additional quadratic term was reported for nanoparticles [231], whose size reduces the k -space of spin waves significantly. In case of magnetic caps, the thickness gradient causes a similar confinement. However, the small quadratic contribution was neglected for fitting $H_{an/n}$.

The thermal activation of the magnetic transitions between onion and vortex state becomes the leading mechanism for temperatures below 50 K. Assuming a weak pinning and constant saturation magnetization, both vortex nucleation and annihilation field are fitted

Tab. 5.1.: Fitting parameters for temperature-dependent vortex nucleation (H_n) and annihilation fields (H_{an}) defined by $H_{an/n}(T) = H_{an/n}(0) (1 - \alpha_{an/n} T^{3/2})$ ($T > 100$ K) and $H_{an/n}(T) = H_{an/n}(0) (1 + \beta_{an/n} T)$ ($T < 50$ K). For comparison, the fitting parameters for planar disks of similar diameter and thickness are also presented. (Taken from [83])

$d[\text{nm}]/\varnothing[\text{nm}]$	$\alpha_n [10^{-4}/\text{K}^{3/2}]$	$\alpha_{an} [10^{-4}/\text{K}^{3/2}]$	$\beta_n [10^{-2}/\text{K}]$	$\beta_{an} [10^{-3}/\text{K}]$
closely packed Py caps on SiO ₂ particles				
20 / 330	14.0 ± 1.0	8.8 ± 0.2	1.2 ± 0.1	16.0 ± 1.2
40 / 330	90.0 ± 2.0	6.9 ± 0.4	1.7 ± 0.2	5.0 ± 0.4
40 / 800	1.3 ± 0.1	7.0 ± 0.2	2.0 ± 0.3	4.5 ± 0.7
individual planar Py disks [230]				
50 / 526	0.08 ± 0.02	1.0 ± 0.2	0.8 ± 0.1	1.3 ± 0.2
50 / 865	0.1 ± 0.03	0.3 ± 0.05	1.1 ± 0.4	5.9 ± 1.9

linearly by:

$$H_{an/n}(T) = H_{an/n}(0) \left(1 + \beta_{an/n} T\right), \quad (5.2)$$

with $\beta_{an/n} = k_B / \Delta E_{an/n} \ln \frac{f_0 \tau}{\ln 2}$ [232]. $H_{an/n}(0)$ is the field where the transition occurs without thermal activation; $\Delta E_{an/n}$, f_0 and τ are the energy barrier for vortex annihilation/nucleation, the attempt frequency of relaxation and the measurement time, respectively. Since f_0 is of the order 10 GHz \div 1 THz [233, 234], the logarithm term contributes by a constant factor of ≈ 25 . The corresponding coefficients $\beta_{an/n}$ are shown in Table 5.1, with values justifying the assumption of weak pinning. The value of β_{an} for Py(20/330) cap arrays is much smaller due to the partial onion transition discussed above. In this approach, the energy barriers for vortex annihilation and nucleation in closely packed Py(40/330) caps are (431 ± 34) meV and (127 ± 10) meV, respectively.

The complementary approach of calculating the energy barriers from relaxation/ susceptibility measurements [233, 234] as shown for out-of-plane magnetized caps [119] could not have been successfully applied without taking into account the curved geometry and modified stray fields of the cap structure.

5.2. Imprinted Non-Collinear Spin Textures in Hemispherical Caps

Vertically stacking two well-studied systems, namely out-of-plane magnetized caps [117–120] and soft-magnetic Py caps (Section 5.1), and providing an interlayer exchange coupling through a variable Pd spacer allows for imprinting non-collinear spin textures into the out-of-plane magnetized layers that resemble vortices, spiral domains and skyrmionic core textures [Fig. 5.5] [115]. These highly symmetric spin textures with distinct topology and tunable normal magnetization component/ opening angle are perfectly suited to deterministically increase the complexity of XMCD contrast analysis on curved surfaces, simultaneously offering interesting physical properties.

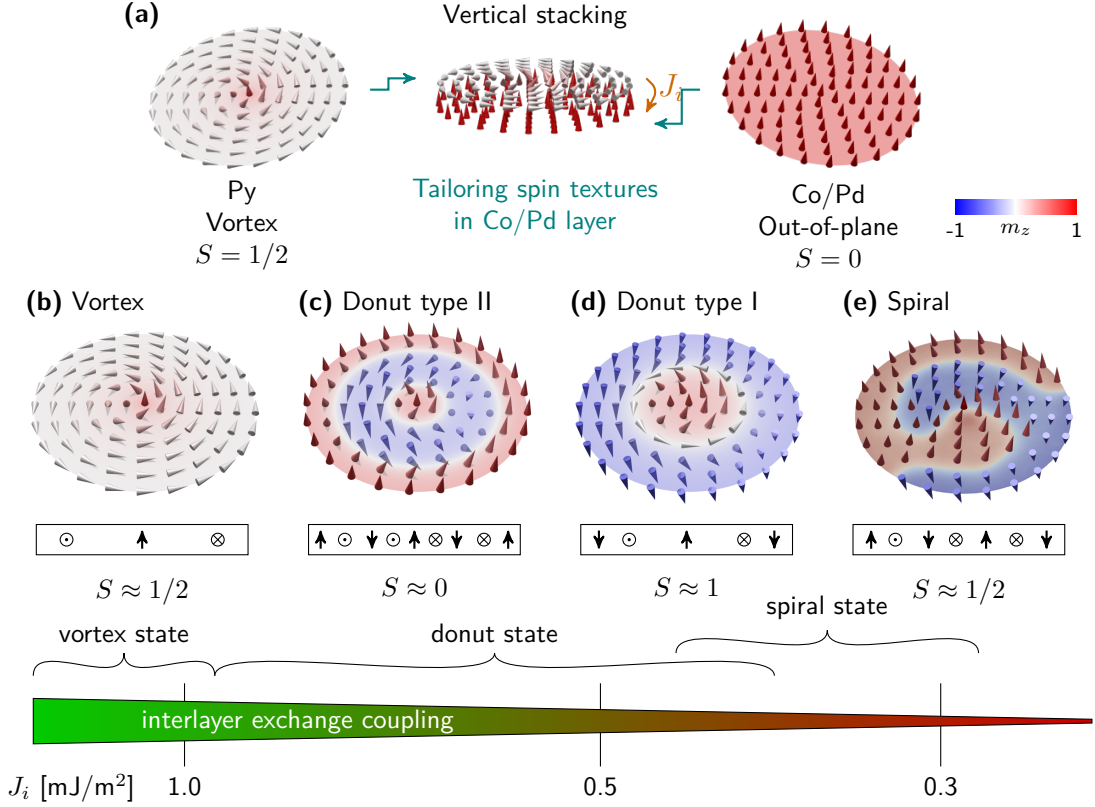


Fig. 5.5.: Imprint of non-collinear magnetic spin textures into out-of-plane magnetized films via interlayer exchange coupling to a vortex state (a). Figures (b)–(e) show four topologically distinct states in Co/Pd films with decreasing interlayer coupling J_i (left to right) after applying an out-of-plane magnetic field revealed by micromagnetic simulations. Colors correspond to the normalized out-of-plane magnetization component. The skyrmion number S of each state is estimated based on the sketched magnetization configuration in the cross-section. (Taken from [115])

5.2.1. Theoretical Predictions

Prior experimental realization the imprint mechanism is theoretically explored using micromagnetic simulations. The leading parameter determining the spin configuration in the out-of-plane magnetized layers is the ratio $\kappa = J_i/(2Kh)$ with thickness h and anisotropy K of the same [235]. In this work, the spacer thickness d and thus the interlayer exchange J_i are varied while keeping K and h constant. Simulations were conducted at $T = 0\text{ K}$ with Nmag v0.2 [236] in combination with the HLib library [237, 238]. Note that the high Curie temperature of the layer stack ($T_c > 400\text{ K}$) justifies the correlation with experimental data taken at room temperature. The modeled disk-like heterostructure consists of out-of-plane magnetized Co/Pd multilayer stack ($M_s = 500\text{ kA/m}$, $A = 10^{-11}\text{ J/m}$,

$K = 200 \text{ kJ/m}^3$) and soft-magnetic Permalloy film ($M_s = 860 \text{ kA/m}$, $A = 1.3 \times 10^{-11} \text{ J/m}$) [Fig. 5.5(a)]. The disk has a diameter $\varnothing = 400 \text{ nm}$ with a mesh size of 2.5 nm and 6 nm for Co/Pd (5 nm thick) and Py (40 nm thick), respectively. The large asymmetry between Co/Pd and Py thickness preserves the topology of the Py vortex. The effect of the Pd spacer thickness on the coupling between the layers is mimicked by varying the interlayer exchange coupling strength in the range $J_i = (0.1 \div 2) \text{ mJ/m}^2$, as expected for RKKY-like coupling [14–16] through Pd [239, 240]. The magnetic coupling through thick Pd spacers ($d \gtrsim 3 \text{ nm}$) is mediated by spin diffusion mechanisms involving unfilled $4d$ and $5s - p$ Pd bands [239], which can numerically described in the same way. Magnetostatic coupling alone does not stabilize the reported configurations [115]. The topologically non-trivial states are characterized by the skyrmion number [17]:

$$S = \frac{1}{4\pi} \int \mathbf{m} (\partial_x \mathbf{m} \times \partial_y \mathbf{m}) dx dy, \quad (5.3)$$

with the magnetization $\mathbf{m} = \mathbf{M}/M_s$ of the out-of-plane magnetized layer. Owing to the confinement within the nanostructure, the net integral charge is fractional [Figs. 5.5(b)–(e)] in contrast to DMI-driven skyrmionic systems with integer values [3–8, 17–19, 69].

In strongly coupled systems ($J_i \gtrsim 1 \text{ mJ/m}^2$), the equilibrium spin configuration, *i.e.* vortex structure, exhibits the same circulation in Py and Co/Pd layers [115]. Decreasing the interlayer exchange coupling ($J_i \approx 0.4 \text{ mJ/m}^2$) and running major or minor hysteresis loops stabilize the remanent donut state type II [Fig. 5.5(c)] and type I [Fig. 5.5(d)] with two and one domain walls, respectively, and radially varying opening angle/ normal magnetization component. In particular, donut type I exhibits a spin configuration similar to those in a disk with DMI [241] and a skyrmion number $S \approx 1$, justifying the reference as a skyrmionic core configuration. The circular symmetry is caused by the imprint of the central vortex core and the cylindrical geometry of the disk. The vortex core diameter in donut configurations is about 80 nm compared to 6 nm in Py [115], illustrating the possibility to tailor the vortex core profile *via* imprint, which might be beneficial for studying the inner structure of the vortex core. Systems with even smaller interlayer coupling ($J_i \lesssim 0.3 \text{ mJ/m}^2$) show a singledomain remanent state. The remanent donut state type II cannot be obtained in these systems, because all Co/Pd spins except the vortex core switch simultaneously.

The spiral state depicted in Figure 5.5(e) forms after relaxation from the out-of-plane saturated state or as remanent state after applying in-plane magnetic fields to the donut state type II [115]. The imprinted vortex core acts as a driving force that twists the domain wall to a spiral while approaching the center. As κ increases, the spiraling distortion of

the domain wall by the imprinted vortex is stronger leading to a more extended spiral. In this respect, its experimental observation would represent a strong hint for an interlayer exchange coupling with an in-plane circulation.

5.2.2. Experimental Observation

Layer stacks consisting of Pd(2)/[Co(0.4)/Pd(0.7)]₅/Pd(d)/Py(40)/Pd(2) with thicknesses in nm and variable Pd spacer thickness d ranging from 1 to 30 nm were prepared onto assemblies of non-magnetic SiO₂ spherical particles with a diameter of 500 nm (Section 3.1). Changing the spacer thickness at small values ($d \lesssim 5$ nm) alters the magnetic properties of the Co/Pd spins, *i.e.* transforming the originally out-of-plane preferential orientation into an in-plane preference [115]. Comparing the experimental hysteresis loops, recorded with the ALICE chamber at BESSY II in collaboration with Dr. F. Radu and Dr. R. Abrudan, with the numerical ones suggests that a spacer thickness $d = (3 \div 5)$ nm corresponds to an interlayer coupling strength $J_i = (0.4 \div 0.5)$ mJ/m², which is expected to stabilize magnetic spiral and donut textures in Co/Pd.

Utilizing XMCD with MTXM and XPEEM, the magnetic states are imaged at remanence after applying magnetic fields $H = \pm 30$ kA/m perpendicularly to the sample surface. In samples with $d = 1$ nm, a dipolar XMCD contrast is observed at the Fe L_3 and Co L_3 edges indicating a perfectly imprinted vortex state in the Co/Pd subsystem [Fig. 5.6(a)] [115]. For XPEEM studies, samples with inverted stack order are used. The 9 nm-thick top layers (Co/Pd and Pd) covering the Py system still allow for detecting secondary electrons excited in both Co/Pd and buried Py, and verifying the same sense of circulation [115]. The vortex state in the thin Co/Pd caps generates a dipolar XMCD contrast contrary to the quadrupolar one occurring in thick Py caps [Figs. 5.1, 5.2]. The small Co thickness and related resonant absorption of left and right circularly polarized X-rays while penetrating the magnetic cap are insufficient to compensate the XMCD contrast at the back side of the cap, usually inducing an inverted XMCD shadow contrast for thick films [83, 85, 137]. The lack of a significant contrast modification makes the interpretation in this respect easier. The XMCD contrast in-between neighboring caps is caused by two mechanisms: Curvature and electrostatic charging generate a halo and a detectable magnetic signal even outside the cap; The aforementioned asymmetry in transmitted intensity of left and right circularly polarized light at resonance results in an artificial XMCD contrast of non-magnetic regions (XMCD shadow contrast). While the first one sets the same contrast as

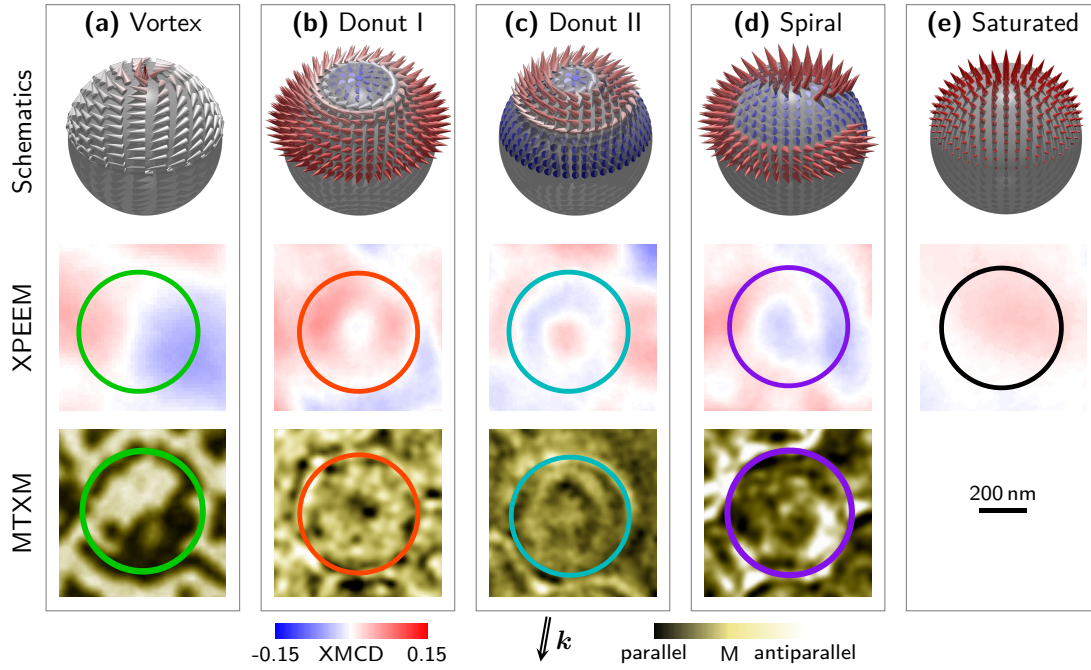


Fig. 5.6.: Experimental observation of imprinted non-collinear spin textures in hemispherical $[\text{Co}/\text{Pd}]/\text{Pd}/\text{Py}$ caps using XPEEM and MTXM. Schematics illustrate corresponding state. Varying Pd spacer thickness leads to distinct states: (a) $d = 1 \text{ nm}$: vortex; (b)–(d) $d = (4 \div 5) \text{ nm}$: donut and spiral; (e) $d = 30 \text{ nm}$: saturated. Circles indicate cap position with a diameter of 500 nm . XPEEM data is recorded at a constant X-ray beam incidence angle of 74° with respect to the surface normal. Out-of-plane and in-plane sensitivity of the MTXM data is provided by normal incidence and by tilting the sample 30° with respect to the X-ray beam, respectively. (Taken from [115])

in the embedding cap, the second one may also partially compensate the XMCD contrast. The very same mechanisms and their explanation apply also to soft-magnetic caps in the vortex state (Section 5.1). However, the high symmetry of their XMCD patterns due to the restriction to an in-plane circulation of the magnetization allowed a proper identification without paying particular attention to these artifacts.

A proper XMCD contrast interpretation becomes even more crucial when analyzing more complex spin textures, *i.e.* donut and spiral state, as occurring in samples with a Pd spacer $d = (4 \div 5) \text{ nm}$ [Figs. 5.6(b)–(d)]. The vortex state within the Py subsystem remains stable independently of the interlayer exchange coupling/ spacer thickness, in contrast to Co/Pd spins that show a transition towards out-of-plane orientation with increasing spacer thickness [115]. The residual coherent in-plane magnetization component due to the imprint mechanism is not detectable by MTXM. However, its impact can be seen by comparing the XMCD contrast of samples with moderate [$d = (4 \div 5) \text{ nm}$, Figs. 5.6(b)–(d)] and negligible

interlayer coupling [$d = 30$ nm, Fig. 5.6(e)], revealing inhomogeneous and "uniform" magnetization, respectively. The word "uniform" refers to the fact that the XMCD contrast of a saturated cap fades out when approaching the edge. Donut state type I [Fig. 5.6(b)] exhibits a white central region surrounded by a red area. The absence of a prominent blue core is due to the limited spatial resolution of the microscope, which leads to an XMCD signal that refers to a net magnetization in a certain volume. For the same reason, Py vortex cores could not be resolved, typically requiring Py film thicknesses larger than 70 nm [101, 242]. The usual implication of white contrast associated with no or very small parallel magnetization components with respect to the X-ray beam propagation direction, as applying to large homogeneous domains with respect to the spatial resolution, is not valid. The XMCD contrast of smaller spin textures, such as vortex cores, is blurred and may thus appear white, bluish, blue or even slightly reddish depending on the core size, when surrounded by magnetization vectors with opposite direction [Fig. 5.7]. The smallest observable core sizes range from 60 to 110 nm, which agrees well with 80 nm derived from micromagnetic simulations [115]. The donut state shown in Figure 5.7(c) possesses a core larger than the vortex core imprinted in Co/Pd by the Py vortex. In other words, not only the local, but also its spatial distribution as known from shadow contrast analysis is crucial for a proper interpretation. Alternatively, the appearance of states with different central contrast at same field history reflects a distribution of slightly varying magnetic properties throughout the cap array. This ends up in the observation of radially varying XMCD contrast patterns belonging to donut states with multiple circular domain walls [Fig. 5.7(e)]. The small asymmetry in the XPEEM data apparent in each cap and perpendicularly to the beam propagation direction [Fig. 5.7] hints for a small in-plane magnetization component of the donut state due to imprinting. The experimental observation of magnetic spirals [Fig. 5.6(d)] is another proof for interlayer exchange coupling with certain circulation as the vortex core dynamics act as a driven force for the domain wall twisting.

Manipulation of Skyrmion Number

The experimental observation of these stabilized non-collinear spin textures at room temperature and remanence is intriguing as it provides means to reliably switch between donut state type I and type II by applying out-of-plane magnetic fields below the switching field of the vortex core. Figure 5.8(a) plots minor and major hysteresis loops obtained by micromagnetic simulations with a moderate interlayer exchange coupling ($J_i \lesssim 0.4$ mJ/m²). The larger switching field of the vortex core $H_{an} \approx 140$ kA/m compared to the switching

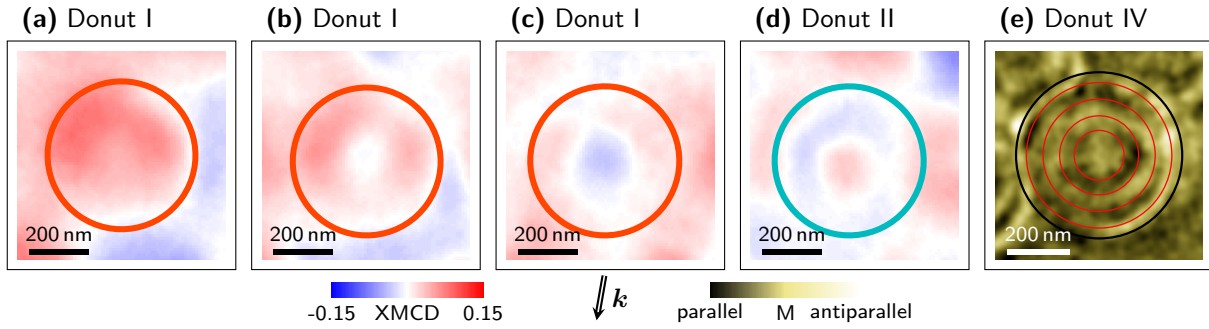


Fig. 5.7.: XMCD contrast patterns of donut states with various core sizes elucidating the importance of proper contrast analysis. (a)–(c) Donut state I with different core size. Cores with lateral expansions below the spatial resolution limit exhibit a shift towards the opposite color (white, bluish). (d) Donut state II with a faint contrast in the very center representing the core. (e) Donut state with four circular domain walls. (Taken from [115])

field of Co/Pd ($H \approx 20$ kA/m) is the basis for setting donut state type I by driving a minor hysteresis loop. The experimental realization is shown in Figure 5.8(b) after applying an out-of-plane magnetic field of $H = \pm 30$ kA/m and observing a distinct contrast change from blue-red to red-blue. In particular, the two XMCD contrast patterns refer to donut state type I and II, as the core polarity cannot be switched in the applied field. Also, both states were accordingly identified in Figure 5.7 based on the local change of the XMCD contrast. The successful manipulation of donut states implies a switching of the skyrmion number S , *i.e.* between $S \approx 1$ and $S \approx 0$, which might be appealing for prospective magnetic storage devices based on digital switching of topological charges.

Moreover, modifying topology of the imprinted states, interlayer coupling and core sizes significantly alters the magnetization dynamics including gyro frequency [Fig. 4.5] and damping coefficients due to varying core masses [217] that can be described by the Thiele equation [243, 244]. The physical limitation to immobile skyrmionic core textures due to spatial confinement to cap or disk may be overcome by stabilizing non-collinear spin textures with controllable topological properties in extended non-planar honeycomb lattices [163], which are also appealing for magnonic and spintronic applications. A demonstration of field- or current-driven displacement will require further optimization of structural and magnetic properties.

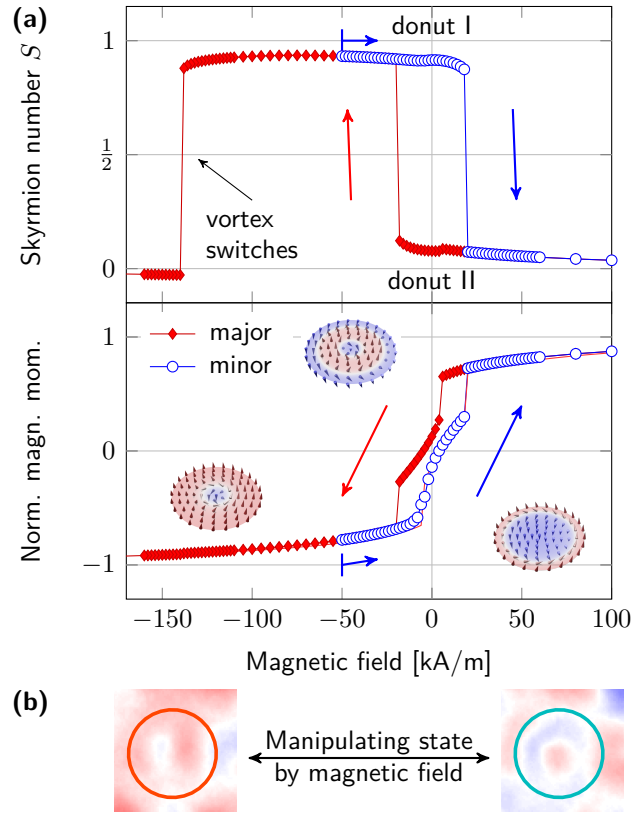


Fig. 5.8.: (a) Theoretically predicted switching of the skyrmion number S via out-of-plane magnetic fields ($J_i = 0.4 \text{ mJ/m}^2$). Initially out-of-plane saturated samples (positive field) exhibit donut state type II at remanence with $S \approx 0$. At negative fields, all Co/Pd spins except the vortex core reverse leading to $S \approx 1$ until the core switches as well. If the core has not been switched, the skyrmion number is preserved at remanence. Insets depict the normal magnetization component. (b) Experimentally observed switching between donut state I and II with same core polarity, and vice versa. (Taken from [115])

5.3. Cylindrical Permalloy Caps

The impact of the curvature-induced modifications on the magnetic properties is further studied by switching from an isotropic thickness gradient existing in hemispherical caps to uniaxial cylindrical caps that may serve eventually as magnetic shift registers. For this sake, non-magnetic cylindrical curvature templates are prepared by rolling up epitaxial strained bilayers and segmented using FIB etching as described in Section 3.2. While sticking to a constant Py film thickness ($d = 20 \text{ nm}$), the tube diameter is varied from 250 nm to 1.7 μm . The Py film is sandwiched by a Ta capping (2 nm) and buffer (5 nm) layer.

5.3.1. Magnetization Reversal Process

The magnetic hysteresis loops of an elongated cylindrical Py cap with a diameter $\varnothing = 600$ nm and a length of $30 \mu\text{m}$ are recorded by magneto-optical Kerr effect (MOKE) magnetometry and exemplarily shown in Figure 5.9(a) for two different in-plane field angles φ . Even though the spot size of the probe laser is approximately $10 \mu\text{m}$, contributions from surrounding planar Py films can be subtracted due to significantly smaller switching fields. In fact, the angle between two adjacent caps located in the probe area could be derived from the hysteresis loops by considering two angle-dependent coercive fields. To compensate for the small signal-to-noise ratio due to strong deflection on the cap, each magnetic hysteresis loop is averaged over thousands of individual sweeps. Figure 5.9(b) plots the coercive field H_c as a function of the in-plane angle φ for two different cap diameters. Its angle dependence is described by the modified Kondorsky model [245–247], which is valid for magnetization reversal processes governed by nucleation and motion of domain walls in uniaxial media taking pinning processes into account. Although the Kondorsky model was originally derived for hard-magnetic media, it can also be applied to describe soft-magnetic planar films with a shape anisotropy [248, 249]. The normalized coercive field reads [84]:

$$h_c(\varphi) = H_c(\varphi)/H_c(\varphi = 0) = h + (1 - h)/\cos(\varphi), \quad (5.4)$$

with the longitudinal coercive field $H_c(\varphi = 0) = H_0$ and the ratio h between the anisotropy constant and the longitudinal coercive field. The coefficients become $H_0 = 4.0$ kA/m, $h = 0.92$ and $H_0 = 1.2$ kA/m, $h = 0.72$ for caps with diameters $\varnothing = 600$ nm and $\varnothing = 1.7 \mu\text{m}$, respectively. Note that the curvature of the magnetic film leads to an increased effective shape anisotropy described by h that is not considered by the original Kondorsky function $h_c(\varphi) = 1/\cos(\varphi)$ (dashed curve) [245].

5.3.2. Magnetic Remanent States

The longitudinal magnetic domains existing in elongated caps transform at a certain segment length into Landau states and eventually for very short caps into transverse domains. This transition is monitored by XPEEM using a photon energy equal to the nickel L_3 absorption edge for three different cap diameters, namely 250 nm, 600 nm and $1.7 \mu\text{m}$, and segment lengths close to the numerically determined phase boundaries [84]. Figure 5.10(a) depicts PEEM and corresponding XMCD image of magnetic cap structures with a dia-

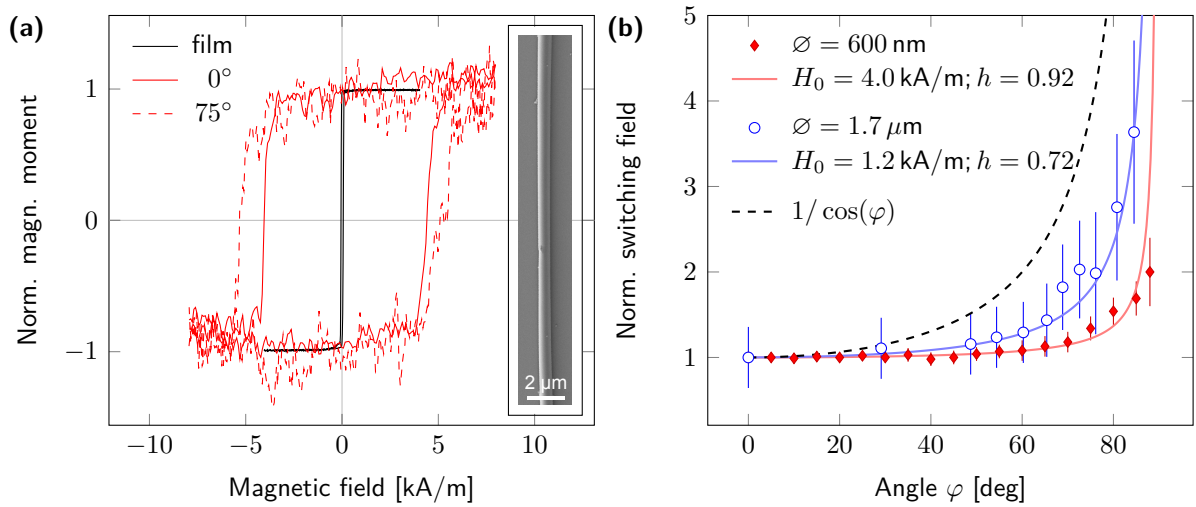


Fig. 5.9.: Angle-dependent magnetization reversal of an elongated soft-magnetic cylindrical cap. (a) Magnetic hysteresis loops of elongated Py caps with a diameter of 600 nm and a length of 30 μm for two different in-plane angles. 0° corresponds to a parallel alignment of the magnetic field with respect to the symmetry axis. (b) Normalized coercive fields fitted by $h_c(\varphi) = H_c(\varphi)/H_c(\varphi = 0) = h + (1 - h)/\cos(\varphi)$ with the longitudinal coercive field constant $H_c(\varphi = 0) = H_0$ and h being the ratio between anisotropy constant and longitudinal coercive field. The unmodified Kondorsky function is plotted for comparison (dashed line). (Taken from [84])

meter $\varnothing = 250$ nm (indicated by dashed rectangle) that reveal a transition from a uniform into X-shape contrast with increasing segment length. The latter pattern corresponds to a curling of the in-plane magnetization and represents a vortex state. Considering the spatial resolution of the used setup, the observed magnetic domains with feature sizes of about 40 nm are already at the limit. Increasing the diameter to 1.7 μm reveals the same transition but with a different scaling [Fig. 5.10(b)]. The accordingly determined magnetic remanent states are inserted as large symbols into the phase diagram, numerically assembled in collaboration with Dr. V.P. Kravchuk, shown in Figure 5.10(c). The hollow triangles represent Landau states with a vortex core (structured vortex states that consist of both 180° and 90° domain walls). Details on the numerical calculations are given in Reference [84]. With decreasing ratio between segment length and cap diameter, a transition from longitudinal *via* vortex to transverse states [Fig. 5.10(d)] occurs showing an excellent agreement between theory and experiment.

Analyzing vortex circulation patterns in double-tube configurations with a diameter of 1.7 μm provides further means to assess the stray field modification driven by the cap curvature [Fig. 5.10(b)]. No coupling between the two narrow cap rows is observed as expected for diameters larger than 800 nm due to the thickness gradient [83]. On the

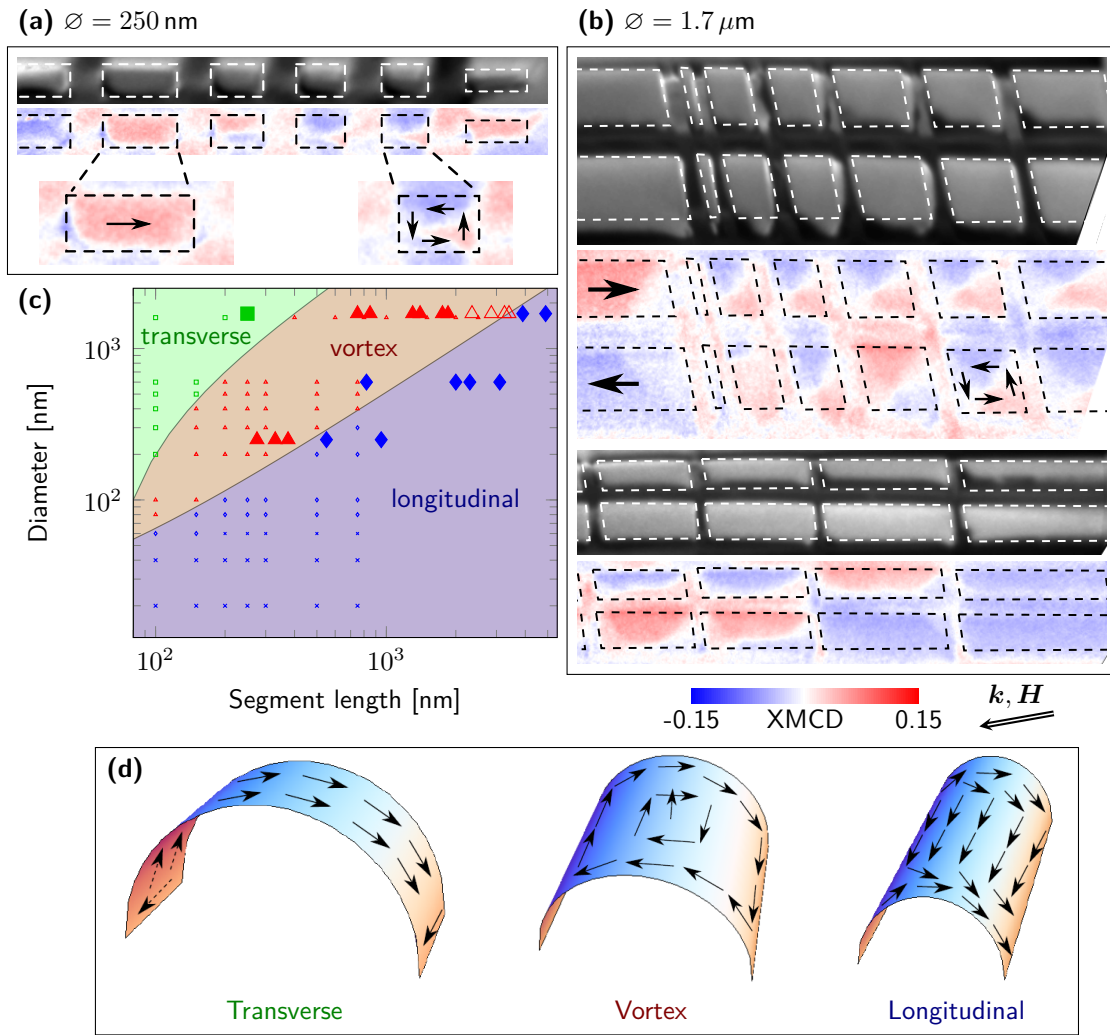


Fig. 5.10.: Magnetic remanent states in cylindrical Py cap structures with a thickness $d = 20$ nm, visualized by XPEEM. Panels (a) and (b) depict PEEM and XMCD images of caps (indicated by dashed rectangles) with a diameter of 250 nm and $1.7 \mu\text{m}$, respectively. Coming from long to short cap segments, the contrast transforms from uniform over multidomain (X-shape) to uniform (white). From the arrangement of the vortex circulation in (b), an anisotropic magnetostatic interaction between neighboring Py caps is observed due to the curvature-driven thickness gradient. (c) Numerically determined phase diagram of magnetic equilibrium states in cylindrical cap structures overlaid by experimental data. The hollow triangles represent Landau states with a vortex core (structured vortex states that consist of both 180° and 90° domain walls). (d) Schematics of the magnetic states. (Taken from [84])

contrary, the magnetostatic interaction between adjacent caps of the same row is not suppressed due to the absence of a thickness gradient along the symmetry axis leading to the same vortex circulation. The corresponding anisotropy of magnetostatic interaction indicates the substantial impact of a thickness gradient, which can even be scaled down to a few tens of nanometers. Thus, a much larger areal density of decoupled wires compared

to planar stripes can be achieved, which is beneficial to increase storage density of magnetic shift registers.

5.4. Magnetic Cap Structures in Life Sciences

Magnetic cap structures discussed in this Chapter are not only fundamentally interesting, but also appealing for life science applications when functioning as self-propelled Janus micromotors due to feasible fabrication, tunable functionality and directionality of motion. Deterministic motion of autonomous self-propelled micromotors has emerged to a rapidly growing field because of its application relevance in medicine for targeted drug delivery [250, 251], hyperthermia for cancer treatment [252–254], microsurgery [255], *et cetera*. Catalytic propulsion of micromotors is one of the leading approaches in the field of intelligent synthetic micromachines [48, 254, 256–259]. Using a combination of magnetic and catalytic layers ensures a directed and autonomous motion in, for instance, H_2O_2 . Redirecting the micromotor by means of magnetic fields requires a stable magnetic easy axis of the system usually given by its shape [259, 260].

We offer an alternative route to sputter deposit Co/Pt multilayer stacks with an out-of-plane magnetization directly onto monolayers of silica microbeads that resemble magnetic Janus particles (Section 3.1) [128]. An out-of-plane anisotropy provides magnetic field control, while the Pt (Pd) capping layer maintain the catalytic chemical reaction in H_2O_2 [Fig. 5.11(a)]. Targeted drug delivery, including pick up, transport and drop off, is achieved by reorienting the magnetic field and thus the Janus particle [Fig. 5.11(b)].

In spite of numerous demonstrations, the catalytic concept suffers from the incompatibility of H_2O_2 -based reactions with biological systems. Alternatives in liquid environment rely on various phoretic effects, such as electrophoresis [261, 262], diffusiophoresis [263, 264] and magnetophoresis [265]. Using Janus particles with thick soft-magnetic caps in combination with an *ac* magnetic field adds another phoretic effect, namely magnetically induced thermophoresis [129]. The heat generated by hysteretic losses (similar to those used for induction cooking) accumulates at the cap and induces a motion [Fig. 5.11(c)]. The directed motion is ensured by the vortex polarity and a *dc* magnetic field.

In this case, amplitude of the *ac* field is limited by the vortex annihilation field to guarantee control over the trajectory. This restriction can be overcome by adding an out-of-plane

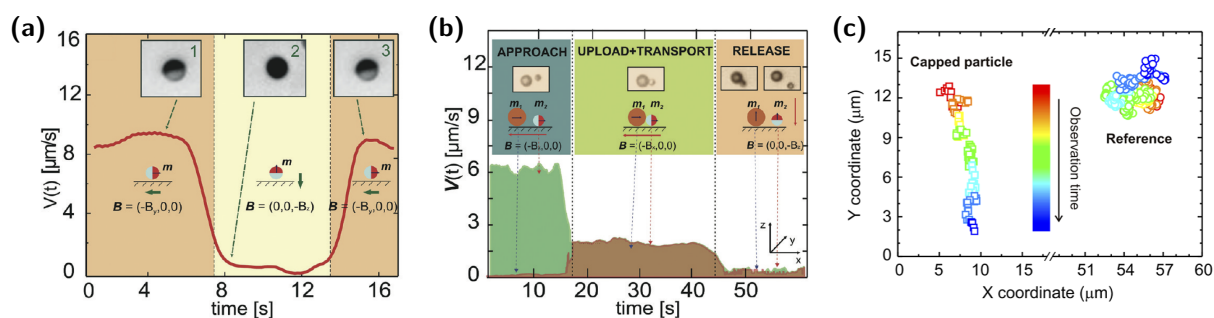


Fig. 5.11.: *Magnetic cap structures applied as self-propelled micromotors for targeted drug delivery in life sciences. (a) Motion control via dc magnetic field of Janus particles with out-of-plane magnetization capped with Pt layer to maintain catalytic reaction in H_2O_2 . (b) Velocity during all three steps of cargo transport: approach, pick up and transport, and release. (c) Self-propulsion of Janus particles with a thick soft-magnetic cap driven by magnetically induced thermophoresis in water. (Taken from (a), (b): [128]; (c): [129])*

magnetized film to the thick soft-magnetic layer. Avoiding any interlayer exchange coupling by choosing a thick spacer, keeps both subsystems independent of each other (Section 5.2) [115]. Distinct resonant frequencies for both subsystems would ensure a selected excitation of the soft-magnetic subsystem with potentially larger velocities.

5.5. Conclusion

In this Chapter, magnetic cap structures, resembling 2D curved surfaces with rotation (hemispherical) and mirror (cylindrical) symmetry were studied using magnetometry and XMCD with XPEEM and MTXM. Magnetic hysteresis loops had been acquire at various temperatures with MOKE and SQUID magnetometry to determine the magnetization reversal process including equilibrium and transition states as well as switching fields. On this basis, phase diagrams of magnetic ground states were assembled for closely packed cap arrays and compared with those obtained by micromagnetic simulations of individual ones.

The validity of those assigned states was proven by visualizing the magnetization in 3D cap structures utilizing XMCD with XPEEM and MTXM. An oblique illumination of the 3D objects in XPEEM led to a partially transmitted X-ray beam that causes at the back side the so-called XMCD shadow contrast. The net XMCD signal in the shadow takes values smaller or larger than that of a single interaction depending on film thicknesses and relative

orientation of magnetization with respect to the X-ray propagation direction. As shown in this Chapter, a proper XMCD contrast interpretation requires a profound understanding of the contrast origin and a precharacterization based on micromagnetic simulations or integral measurements like magnetometry. Exploiting the enlarged spatial resolution of the shadow contrast along the X-ray propagation direction due to non-orthogonal projections, magnetic states below the resolution limit of the XPEEM could be identified. Changing film thickness and cap diameter allowed further to tailor magnetostatic intercap interactions and provided means to nucleate closely packed vortices in cap arrays with distinct circulation patterns that might be interesting to applications for both vortex RAM and magnonics.

These closely packed vortices were used to imprint non-collinear spin textures, such as vortices, spirals and donut states representing skyrmionic core configurations, *via* interlayer exchange into out-of-plane magnetized caps. High symmetry and tunable normal magnetization component were exploited to deterministically increase the complexity of XMCD contrast analysis on curved surfaces. Potential applications of magnetic cap structures in life sciences were briefly discussed by demonstrating autonomous directed motion and drug delivery when employed as Janus micromotors.

The present cap geometries – curved surfaces with a major orientation normal to the substrate – were mainly studied with conventional "top view" microscopy. By these means the magnetic domain patterns could be visualized. More complex magnetic objects with multiple surfaces, *e.g.* cylindrical objects, cannot be addressed in this manner due to the lack of information about areas hidden from direct illumination of the beam and demand new approaches to be explored.

The present results are summarized in the following publications:

- Soft-magnetic caps on closely packed spherical particles: magnetization reversal, phase diagram and circulation patterns [83?],
- Single hemispherical caps: phase diagram, demonstration of T-XPEEM [85],
- Imprinted non-collinear spin textures in hemispherical caps [115],
- Caps on cylindrical objects [84],
- Cap structures functioning as Janus micromotors in life sciences [128, 129].

6. Cylindrical Magnetic Architectures

Cylindrical magnetic architectures prepared by rolled-up nanotech are tubular objects with well-defined magnetization orientation and tunable geometry. While on-chip integratability makes them very attractive for magnetic sensor application, their uniaxial cylindrical shape is well suited to develop magnetic 3D imaging and tomography techniques based on the knowledge accumulated in previous chapters. For either case, magnetic properties have to be set and investigated. Longitudinal and different kinds of circulating magnetization patterns are provided using magnetostrictive strained transition metals. Tube diameter and film thickness are varied in the lower micrometer and nanometer range, respectively, to ensure X-ray transparency and dimensions smaller than the field of view of the X-ray microscope both crucial for X-ray tomography studies. As the tube dimensions are much larger than the magnetic exchange length ($l_{ex} \approx 10$ nm), qualitative statements found for such microscopic tubes apply also to larger mesoscopic ones. *Results shown in this chapter are summarized in References [132, 133, 137].*

6.1. Tailoring Magnetic Domain Patterns

Tubular architectures with in-plane magnetization are prepared by rolling up magnetostrictive strained nanomembranes evaporated onto a sacrificial layer as described in Section 3.2. The tube diameter is varied in the lower micrometer range $\varnothing = (1 \div 20) \mu\text{m}$ [Fig. 3.4]. Varying the composition of NiFe alloy films allows further to tailor both magnitude and orientation of the strain-induced magnetic anisotropy by adjusting the effective magnetostriction constant [266].

6.1.1. Magnetic Hysteresis Loops

Magnetic properties of evaporated 20 nm-thick Py and Ni rolled-up nanomembranes, including switching fields and strain-induced anisotropies, are determined from magnetic hysteresis loops recorded with MOKE magnetometry [Fig. 6.1]. This way, the magnetization reversal of individual planar films before rolling (dashed curves) and of the top part of individual rolled-up tubes with diameters $\varnothing \approx 12 \mu\text{m}$ (solid curves) are investigated. The MOKE measurements are performed by applying an external magnetic field parallel (0°) and perpendicular (90° , in-plane) to the symmetry axis. The magnetic strain-induced easy axes along the longitudinal and transverse direction for Py and Ni, respectively, cause a rectangular shape of the hysteresis curves measured along those directions [Fig. 6.1]. The coercive field of the evaporated Py samples of $H_{c,P}^{Py} = (10.0 \pm 0.2) \text{ kA/m}$ is substantially larger than those typically obtained by magnetron-sputter deposition [84, 132]. Because of a larger evaporation pressure of nickel compared to iron, e-beam vapor deposition of Py ($\text{Ni}_{80}\text{Fe}_{20}$) results in an NiFe alloy with an approximately 4% larger iron concentration [267], which is in the following referred to as Fe-rich Py. The corresponding positive magnetostriction constant [266] imparts a strain-induced uniaxial anisotropy along the symmetry axis. Using a non-optimal general-purpose e-beam chamber further implants impurities that alter the magnetic properties. The latter statement was verified by depositing nickel at the same conditions in the very same and a brand-new dedicated chamber leading to coercive fields $H_{c,P}^{Ni} = (4 \div 12) \text{ kA/m}$ and $H_{c,P}^{Ni} = 3 \text{ kA/m}$, respectively. Both coercive and switching fields decrease upon rolling due to partial strain relaxation (Section 3.2).

The magnitude the strain-induced anisotropy is derived from the area enclosed by hard and easy axis hysteresis loops resulting for planar and rolled-up Fe-rich Py nanomembranes in $K_P^{Py} = (10.1 \pm 0.5) \text{ kJ/m}^3$ and $K_T^{Py} = (7.5 \pm 0.5) \text{ kJ/m}^3$, respectively. The corresponding compressive strains along the deposition incidence plane (90°) become $\varepsilon_P^{Py} = (1.3 \pm 0.4)\%$ and $\varepsilon_T^{Py} = (1.0 \pm 0.3)\%$, respectively, using the relation for the magnetostrictive anisotropy [67]:

$$K = \frac{3}{2} \lambda \varepsilon Y, \quad (6.1)$$

with the magnetostriction constant $\lambda = 0.5 \times 10^{-5}$ and the Young's modulus $Y = (100 \pm 20) \text{ GPa}$ for electroplated Py [266, 268, 269]. Note that the Young's modulus strongly depends on the morphology and may vary from the actual value of the present film. Comparing the strain relaxation of 0.3% to the analytically calculated strain required to roll up into tubes with such dimensions of 0.4% [Tab. 3.2] suggests that the remaining strain

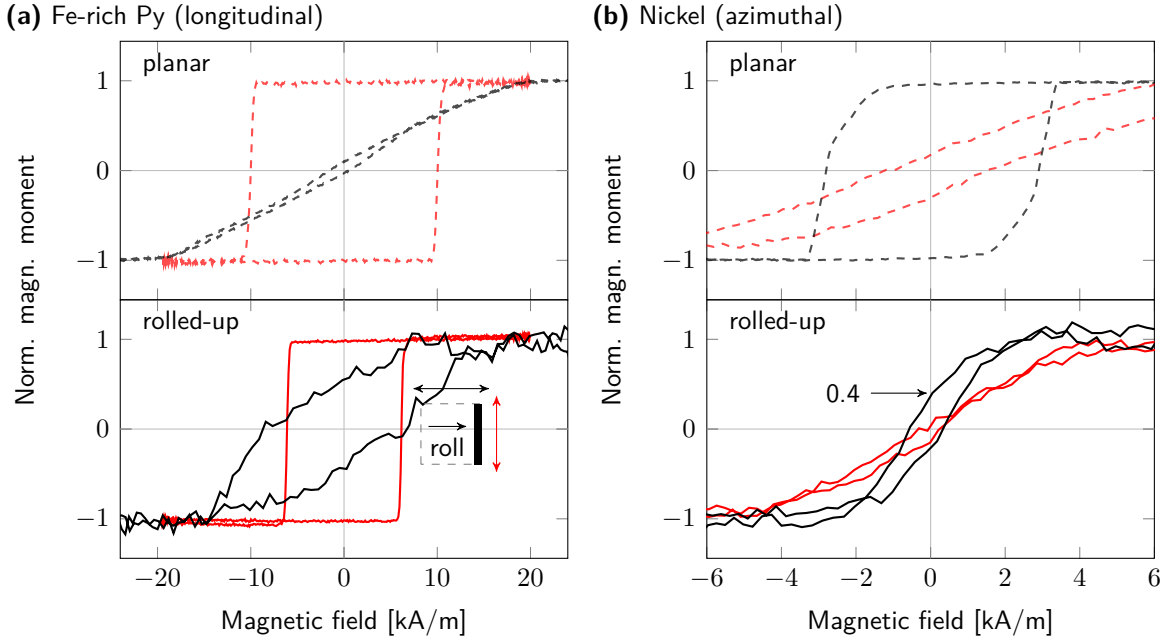


Fig. 6.1.: Magnetic hysteresis loops of planar and rolled-up nanomembranes consisting of (a) iron-rich Permalloy and (b) nickel. A clear difference in the magnetic easy axis is observed due to distinct magnetostriction constants. The strain is partially released upon rolling up, which reduces the magnetic anisotropy. The planar nickel film is saturated at remanence. After forming a cylindrical geometry the nickel magnetization arranges in multidomain states. (Taken from [133])

does not originate from a strain gradient but is due to a poor film quality also apparent by the large coercive fields.

In case of Ni, the strain-induced anisotropies for planar and rolled-up nanomembranes become $K_P^{Ni} = (1.2 \pm 0.3) \text{ kJ/m}^3$ and $K_T^{Ni} = (0.5 \pm 0.2) \text{ kJ/m}^3$, respectively. Using magnetostriction constant $\lambda = -3.5 \times 10^{-5}$ and the Young's modulus $Y = (150 \pm 50) \text{ GPa}$ [266, 270], the corresponding strains along the rolling direction are $\varepsilon_P^{Ni} = (0.02 \pm 0.01)\%$ and $\varepsilon_T^{Ni} = (0.01 \pm 0.01)\%$, respectively. Thus, the remaining strain is substantially smaller using a dedicated e-beam chamber than those determined for Py films. In any case, using magnetotstrictive materials for rolling up always induces a strain-induced magnetic easy axis due to remaining strain contributions that may be employed for magnetic sensing applications.

6.1.2. Magnetic Domains

The magnetic domain patterns in these hollow cylindrical objects are visualized with Kerr microscopy in collaboration with Dr. R. Schäfer (Section 4.1). In particular, the magnetic contrast is acquired from a narrow $5\ \mu\text{m}$ -wide stripe on top of the tube that could be focused onto during imaging [Fig. 6.2(a)]. The beam deflected from this region with surface angles in the range $(-25 \div 25)^\circ$ can still be collected by the objective. Figures 6.2(b)–(d) depicts the magnetic domain patterns revealing longitudinal, azimuthal and helical configurations at remanence after *ac* demagnetization [133]. These magnetic states are illustrated in Figure 2.10. The dash-dotted lines indicate the region with a detectable magnetic contrast that is smaller than the actual tube [Fig. 6.2(a)]. Note that the classification of an azimuthal magnetization configuration is given as rough classification. It is not possible to discriminate azimuthal states from helical ones with small pitch (offset along symmetry axis per winding) based on Kerr microscopy and magnetometry. Changing the geometry of the nanomembrane from $100\ \mu\text{m} \times 100\ \mu\text{m}$ to $50\ \mu\text{m} \times 100\ \mu\text{m}$ (with a shorter tube length) alters the magnetic shape anisotropy of the sample and allows for tilting the effective magnetic easy axis from longitudinal to helical orientation [Fig. 6.2(d)]. Alternatively, the same result is obtained when depositing at a tilt angle with respect to the edge of the rectangular nanomembrane. Generally, this leads to a rolling up along the same tilt angle forming a rolled-up nanomembrane with structural helical geometry.

The physical origin of small domains with circulating magnetization forming at remanence in tubular objects is its topology [Fig. 6.2(a)]. The domain formation while applying a magnetic field along the symmetry axis, representing the hard axis, is similar to that of planar micro stripes with a transverse magnetic easy axis [271]. In contrast, remanent domains after applying a magnetic field along the easy axis are significantly larger in planar stripes than in a tube. The initially homogeneous magnetization in the planar stripe splits up into domains to minimize magnetic stray field contributions. The maximum domain wall density is determined by the strength of the magnetic anisotropy and the stripe width [272]. On the contrary, tubular architectures start with homogeneously magnetized domains at the surfaces perpendicular to the applied magnetic field. The domain walls nucleate at the surfaces parallel to the field direction as no preferential magnetic orientation is induced and propagate through the entire tube in circulating/ azimuthal direction, leading to a non-saturated remanence state [Fig. 6.2(b)]. Thus, smaller magnetic anisotropies are needed allowing for larger domain wall densities. Co-evaporation of nickel and carbon provides further means to alter strain, saturation magnetization and exchange, favoring

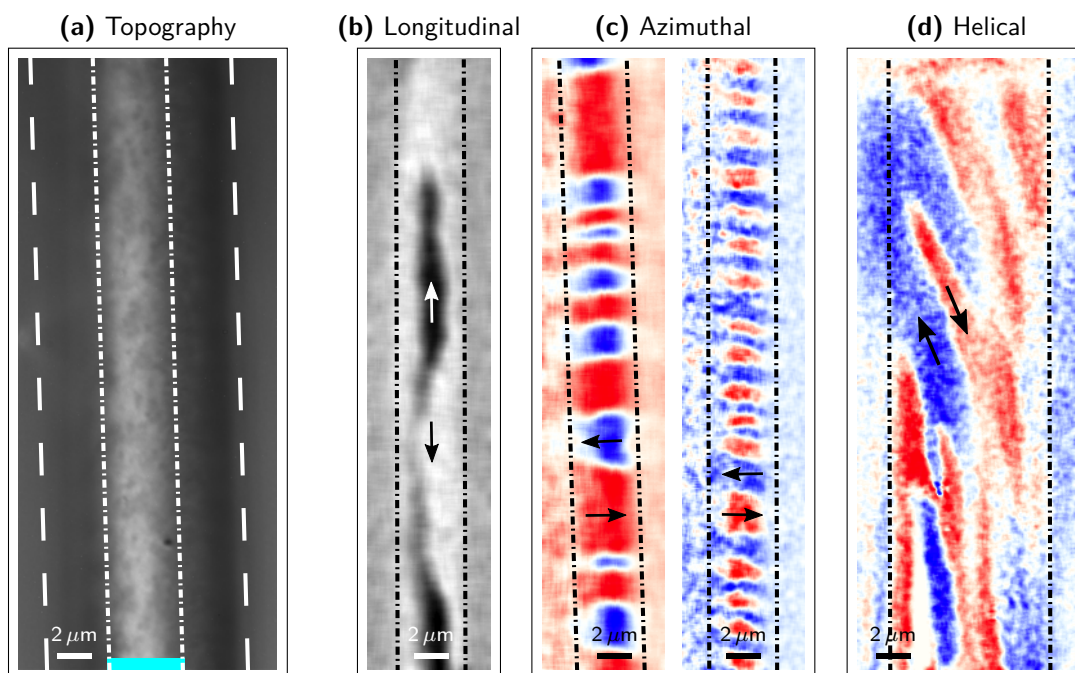


Fig. 6.2.: Magnetic domain patterns in iron-rich Permalloy and nickel nanomembranes rolled up into cylindrical objects imaged with Kerr microscopy after ac demagnetization. (a) Optical image of the top side of a tube ($\varnothing = 12 \mu\text{m}$, indicated by dashed lines). Only a narrow $\approx 5 \mu\text{m}$ -wide stripe on top of the tube (indicated by dash-dotted lines and cyan marker) is in focus due to the curvature and limited depth of focus. (b) Longitudinal magnetization pattern in Fe-rich Py tubes with $\varnothing = 12 \mu\text{m}$ and a length of $100 \mu\text{m}$. (c) Azimuthal magnetization in Ni tubes with the same geometry. (d) Helical magnetization with both azimuthal and longitudinal components in Fe-rich Py tubes with $\varnothing = 20 \mu\text{m}$ and a length of $50 \mu\text{m}$. Magnetization is indicated by arrows. The states are illustrated in Fig. 2.10. (Taken from [133])

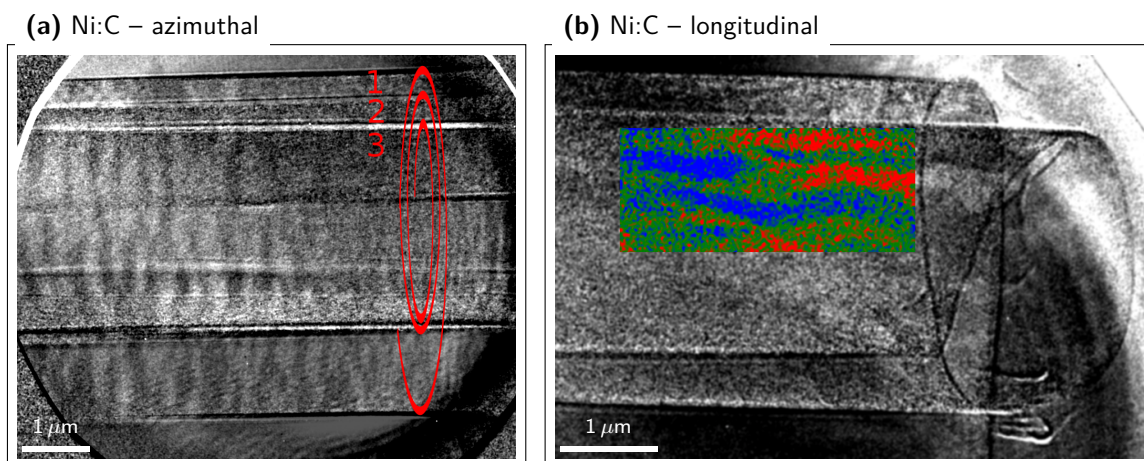


Fig. 6.3.: Magnetic domains in rolled-up Ni film alloyed with carbon visualized with MTXM. Panels (a) and (b) show states with a magnetic easy axis perpendicular and parallel to the symmetry axis, respectively. Red line in (a) schematically shows the winding of the rolled-up nanomembrane. The magnetic pattern in panel (b) is color coded. (Taken from [133])

azimuthally magnetized domains with feature sizes down to 100 nm [Fig. 6.3] and potentially low magnetic anisotropy perfectly suited for giant magnetoimpedance-based sensors for magnetoencephalography. The continuity of the magnetic film even favors a transition from longitudinal into helical magnetization patterns upon rolling [132].

6.1.3. Magnetoresistance Measurements

The magnetoresistive response can be used as a fingerprint of well-defined magnetic domain patterns, such as longitudinal and azimuthal magnetization textures, and applied to obtain information on the magnetization reversal behavior of the entire cylindrical object. Vice versa, the magnetic domain patterns have to be tuned to adjust sensor characteristics of magnetoresistive devices. For this sake, the tubes are transferred onto electric gold contact pads using a micromanipulator in a cross-beam workstation and contacted in two-point geometry by focused ion beam-assisted Pt deposition [Fig. 6.4(a), also Section A.1]. A direct current of 10 mA, equal to a current density of about 10^6 A/cm², is applied to the sample during measurement (in collaboration with M. Melzer).

Magnetoresistance (MR) curves of Fe-rich Py and nickel rolled-up nanomembranes are shown for various field directions in Figures 6.4(b) and 6.4(c), respectively. The uniaxial longitudinal magnetic anisotropy of Fe-rich Py is reflected by a prominent angle-independent magnetoelectric response perpendicular to the symmetry axis, the decrease in resistance for increasing angles between current and magnetization [273] and a flat curve recorded along the symmetry axis with two minima occurring at the coercive field [Fig. 6.4(b)]. The azimuthal Ni magnetization reveals essentially different characteristics with a large drop in resistance at the coercive field along and small hysteresis curves perpendicular to the symmetry axis [Fig. 6.4(c)]. Small deviations of the remanence resistance for perpendicular alignment are assigned to edge effects of the rolled-up nanomembrane, such as domain walls and longitudinal magnetization components leading to a larger anisotropic magnetoresistance (AMR). Nonetheless, the AMR curves exhibit a uniaxial magnetic symmetry of rolled-up nanomembranes in spite of their spiral-like cross-sections. This uniaxial symmetry was independently verified for soft-magnetic tubes by ferromagnetic resonance spectroscopy (FMR) [82, 131] and magnetic X-ray imaging (Section 6.2) [137].

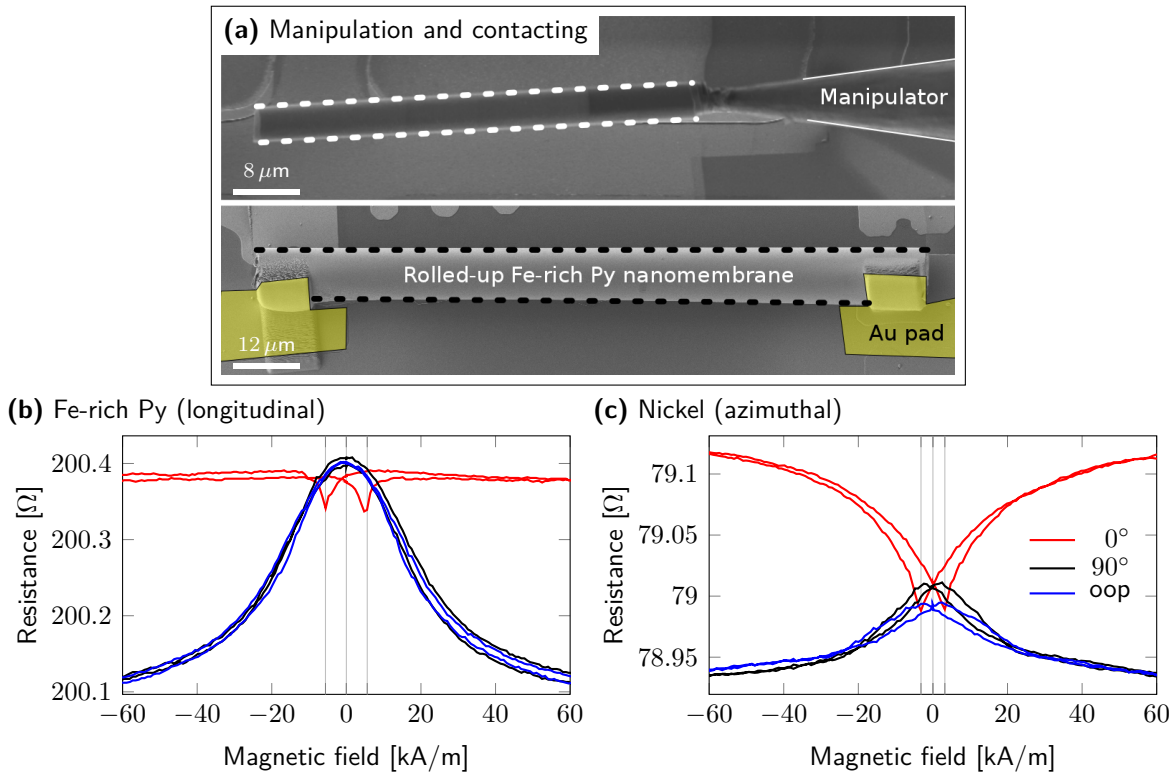


Fig. 6.4.: *Magnetoresistance curves of magnetic tubes with longitudinal and azimuthal magnetic domain patterns. (a) After transferring and contacting the tube to gold pads using micro-manipulator and FIB assisted Pt deposition in a cross-beam workstation, measurements were carried out in two-point configuration. (b) Whereas Fe-rich Permalloy shows a hysteresis-free response perpendicularly to the symmetry axis, (c) nickel exhibits the typical anisotropic magnetoresistance characteristics due to azimuthal anisotropy. Dips in the longitudinal curves (0°) correspond to the switching fields. (Taken from [133])*

6.2. Imaging Inner Magnetization Textures

The demand for a 3D reconstruction of the magnetization field to fully characterize the tubular architecture requires the development of magnetization-sensitive tomographic imaging. The crucial aspect of identifying domain patterns in buried magnetic films is exemplarily demonstrated for tightly and loosely wound rolled-up nanomembranes with a winding separation of about 200 nm [Fig. 3.4(b)]. The curved thin films consist of $\text{In}_{33}\text{Ga}_{67}\text{As}(5)/\text{GaAs}(5.6)/\text{Py}(15)$ layer stacks with units in nanometer and diameters $\varnothing \lesssim 3 \mu\text{m}$ (Section 3.2). The 12 nm-thick non-magnetic capping layer prevents Ni and Fe photoelectrons from leaving the surface due to inelastic scattering while lowering the X-ray beam intensity by merely 2% [133]. Thus, information about the magnetization can only be obtained in transmission by analyzing the shadow XMCD contrast at the back side

of the 3D object (Section 4.3.4). This possibility further enables an on-chip characterization of optionally encapsulated magnetic devices without the need to transfer them onto transparent nanomembranes as required for TXM.

6.2.1. Tightly Wound Rolled-up Nanomembranes

The projected images of the magnetization in tightly wound rolled-up nanomembranes reveal large domains with a magnetization pointing either along or perpendicularly to the symmetry axis [Fig. 6.5]. The dash-dotted lines enclose the shadow region of the tube located at the top. The magnetization components along the X-ray propagation direction, namely 45° , are color-coded in blue/ red. Note that white refers to a vanishing *net* XMCD signal originating from either a perpendicularly aligned magnetization or contrast compensation due to the penetration of X-ray beams through multiple windings with opposed magnetization orientations (Section 4.3.4).

In order to identify the corresponding magnetization patterns, XMCD contrast simulations are performed (in collaboration with Dr. L. Han) taking into account a magnetization-dependent absorption of the circularly polarized X-ray beam penetrating a magnetic tube. The magnetization field is analytically defined on the tube assuming uniform distributions, such as longitudinal and azimuthal magnetization alignments. The absorption coefficient for (anti-)parallel alignment is approximated in first order as [133]:

$$\mu_{\pm} = \mu_{\pm}^{Fe} \frac{a_{Fe \text{ in Py}}}{a_{Fe}} + \mu_{\pm}^{Ni} \frac{a_{Ni \text{ in Py}}}{a_{Ni}}, \quad (6.2)$$

with the atomic density a . The individual absorption coefficients are estimated based on the work of Stöhr [212] (*i.e.* $\mu_{+}^{Fe} \approx 1 \mu\text{m}^{-1}$, $\mu_{-}^{Fe} \approx 5 \mu\text{m}^{-1}$, $\mu_{+}^{Ni} \approx 3 \mu\text{m}^{-1}$ at the Fe L_3 absorption edge). Contributions from the non-magnetic layers of 2% are neglected. The effective absorption coefficient is obtained by linear interpolation between μ_{-} and μ_{+} with the scalar product of magnetization \mathbf{M} and X-ray propagation direction \mathbf{k} :

$$\mu_{\pm}^* = \mu_{\pm} + (\mu_{\mp} - \mu_{\pm}) \frac{1}{2} (\mathbf{M}\mathbf{k} + 1). \quad (6.3)$$

The accordingly defined intensity at each point j of the tube is multiplied along the X-ray propagation direction and projected onto a plane representing the substrate.

Correlating experimental and simulated data allows for identifying states with azimuthal

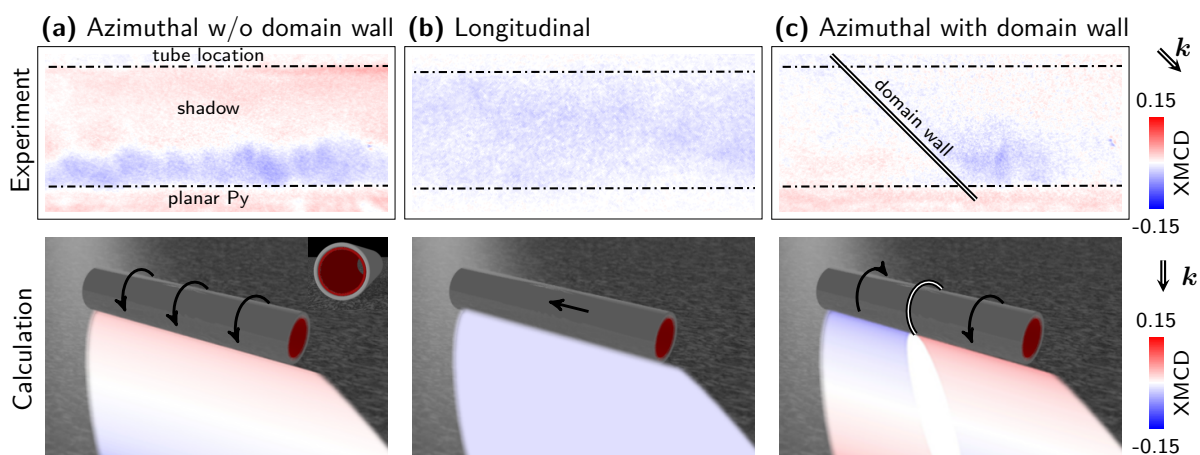


Fig. 6.5.: Comparison between experimental and simulated shadow XMCD contrast of (a) an azimuthally and (b) a longitudinally magnetized state within a magnetic tightly wound rolled-up nanomembrane with cylindrical shape. The orientation of the magnetic moments is indicated by arrows. X-ray beam hits the tube at a shallow angle of 16° and at 45° with respect to the symmetry axis. Dash-dotted lines enclose the shadow region of the tube with one winding. Panel (c) shows an azimuthal state with a 180° domain wall domain wall perpendicular to the symmetry axis (double line). (Taken from [137])

[Fig. 6.5(a)] and longitudinal [Fig. 6.5(b)] magnetization. As the X-ray beam hits the sample at 45° with respect to the symmetry axis, 180° domain walls perpendicular to the symmetry axis are projected under 45° in the shadow contrast. Consequently, 180° domain walls perpendicular to the symmetry axis (azimuthal orientation) generate an elliptical region with zero net XMCD contrast aligned along the beam propagation direction [Fig. 6.5(c)]. The good correspondence between experiment and simulation suggests that indeed tightly wound rolled-up nanomembranes with multiple windings can be treated as a tube [131] with a magnetostatically driven commensurable domain pattern throughout all windings [133].

6.2.2. Loosely Wound Rolled-up Nanomembranes

The capability to resolve layer specifically magnetic domain patterns is demonstrated on the example of rolled-up nanomembranes with loosely wound layers separated by approximately 200 nm [Fig. 3.4(b), right image]. The corresponding XMCD signal of the object consists of narrow stripes aligned along the symmetry axis which refer to the magnetic contrast originating from each winding [Fig. 6.6]. Upon illumination with linear polarized light, the edges of those windings appear as dark lines due to an effectively varying thick-

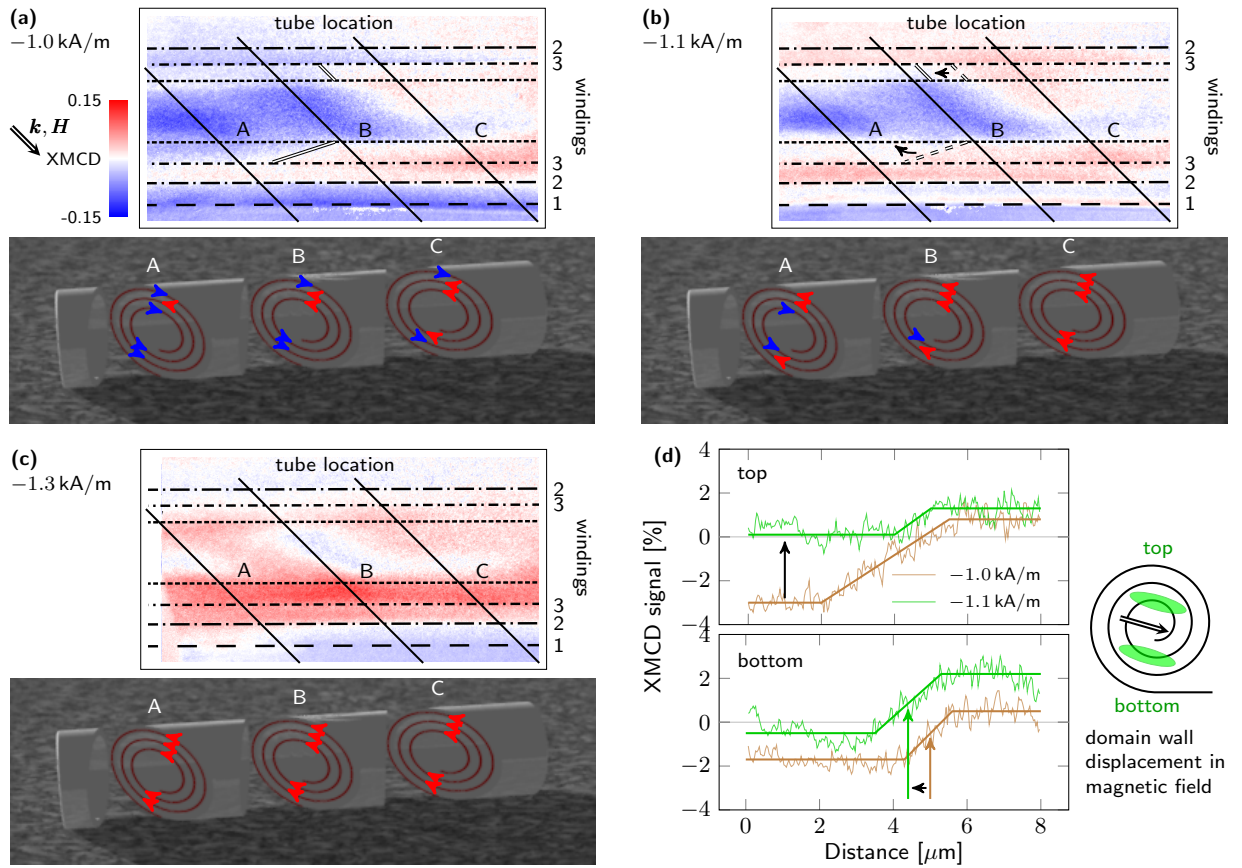


Fig. 6.6.: Layer-specific imaging of buried 3D magnetic rolled-up nanomembranes with multiple windings using T-XPEEM. The distinction between signals of different windings is accomplished as the absorption at the edges of the windings is pronounced (indicated by dash-dotted lines). (a)–(c) Snap shots of the magnetization reversal process while applying an in-plane magnetic field at 45° with respect to the symmetry axis after initially saturating at 2.4 kA/m . The planar magnetic film switches already at $< 0.2 \text{ kA/m}$. The magnetization at each winding can be reconstructed from the shadow contrast as shown for different line profiles (A, B, C) and reassembled along the symmetry axis. (d) Line profiles along the tube, i.e. of winding 3, provide insight into the magnetic field-driven evolution, including the distinction between domain wall displacement along or perpendicular to the symmetry axis (indicated by black arrow). (Taken from [137])

ness. The sample was initially saturated by applying an in-plane magnetic field larger than the switching field and sequentially exposed to increasing negative fields. As the shadow contrast is analyzed on top of a uniformly magnetized planar Py film, an additional but non-disturbing offset has to be considered. The central shadow region refers to layers that experience mainly perpendicular magnetic field components. Hence, contrast changes appear at larger fields. Contrary, the contrast at the edge of a winding fades and reverses at field values $H_c = (-1.3 \div -1.0) \text{ kA/m}$ similar to those obtained by magneto-optical Kerr effect magnetometry [137]. The larger XMCD signal originating from the edge of

each winding allows for reconstructing more complex magnetization configurations within the 3D magnetic architectures. The dependence of the magnetization reversal on the local magnetization orientation (domains) emphasizes the importance of a non-destructive layer-specific imaging of individual windings. The magnetization orientation at each winding along the profile sections A, B and C are shown in the corresponding schematic 3D images [Fig. 6.6]. Stacking multiple line profiles along the symmetry axis provides means to assess the magnetization configuration within the 3D magnetic architecture. The observation hints for a continuous domain pattern in the nanomembrane with oblique domain walls, thus appearing at different locations along the symmetry axis in each winding.

A more quantitative analysis of the magnetization including domain wall displacement during magnetization reversal is done by extracting the line profile of each winding along the symmetry axis, exemplarily shown for winding 3 in Figure 6.6(d). The transition region marked by brown and green arrows for external magnetic fields of -1.0 and -1.1 kA/m, respectively, refer to the magnetic domain walls indicated by solid double lines. The dashed double lines represent for illustration the domain wall position at -1.0 kA/m [Fig. 6.6(b)]. Analyzing the XMCD signal of the top and bottom part of winding 3 reveals a displacement perpendicular to and along the symmetry axis, respectively. Assuming a continuous pattern, such a change may be assigned to a combination of domain wall translation and rotation, which is likely to occur in soft-magnetic materials. Moreover, the similarity of the magnetic pattern in Figures 6.6 and 6.5(c) suggests an azimuthal or slightly tilted magnetization in the inner winding, whose energetically unfavored domain decreases in size by magnetization rotation and domain wall displacement.

6.3. Conclusion

Magnetic thin films with cylindrical shape in the lower micrometer range were investigated utilizing XMCD with T-XPEEM and MTXM, and applying Kerr microscopy and MOKE magnetometry. Properly choosing strained magnetic nanomembranes allowed to fabricate hollow cylindrical architectures with tailored magnetic properties due to residual strain distributions in the relaxed rolled-up film. Varying both magnetostriction constants of the NiFe alloy and shape of the magnetic film provided means to set longitudinal, helical or azimuthal magnetization configurations. Particularly, domains with circulating magnetization and small magnetic anisotropy stabilized by the cylindrical geometry of the tube

could be of interest for giant magnetoimpedance (GMI) applications [138]. The tunability was suggested by MOKE magnetometry and magnetoresistance measurements, and confirmed by direct visualization of the in-plane magnetization component on top of the tube using Kerr microscopy. Strong beam deflection on curved surfaces and defocusing problems restrict the use of reflection microscopy like Kerr microscopy to a narrow stripe ($\approx \frac{1}{3}\varnothing$) along the very top of the tube. This issue could in principle be solved by recording images while rotating the sample around the symmetry axis. However, spatial resolution limits and the lack of information about buried magnetic domain patterns cannot be overcome.

Magnetic domain patterns of buried magnetic surfaces were visualized on-chip and as a function of external magnetic fields by analyzing the XMCD shadow contrast of rolled-up nanomembranes with T-XPEEM. Whereas the magnetization in loosely wound surfaces behaves independently in each winding, tightly wound nanomembranes reveal a uniaxial magnetic anisotropy due to magnetostatic coupling between adjacent windings. The capability of on-chip characterization is highly demanded to confirm the performance of already integrated devices before and after encapsulation.

Acquiring 2D projections of the magnetization along a single projection angle provides first insight into the 3D magnetization configurations. However, this information is in general insufficient to retrieve the spatial distribution of the magnetization in 3D objects. For this sake, a complete set of projections is required as will be presented in the next Chapter.

The present results are summarized in the following publications:

- Magnetic rolled-up nanomembranes with cylindrical shape: fabrication, "top view" visualization with Kerr microscopy, magnetic hysteresis, magnetoresistance [132, 133],
- Buried magnetic domain patterns: layer-specific identification with T-XPEEM [137],

7. 3D Imaging of Tubular Magnetic Architectures

With a solid background of understanding the origin of XMCD contrast patterns in 3D magnetic thin films, proper methods to prepare hollow cylindrical objects with well-defined magnetic properties and shape, and approaches to visualize element- and layer-specific inner magnetization textures, all requirements to develop 3D imaging – magnetic soft X-ray tomography (MXT) – are fulfilled. To demonstrate the capability of MXT, we retrieve the magnetic domain patterns in tubes with well defined magnetization orientations. For these systems, the magnetization distribution can be determined from one data set recorded around one single projection axis that coincides with the symmetry axis. Using reconstruction algorithms to analyze the angular evolution of 2D projections provides quantitative information about domain patterns and magnetic coupling phenomena between windings of azimuthally and radially magnetized tubular objects. While simple spin textures like circulating magnetization textures can be derived from the experimental data by correlation with XMCD contrast simulations in the projected patterns, more complex domain patterns require proper tomographic reconstruction algorithms. *Results shown in this chapter are summarized in Reference [65].*

7.1. Circulating Magnetization Patterns

Strained Ni nanomembranes rolled up into cylindrical objects are lifted with a micromanipulator and vertically fixed using focused ion beam (FIB) assisted Pt deposition on a Pt coated Si wafer (Section A.1). After manipulation, the Ni tube exhibits an elliptical cross-section with a major and minor axis of $x = (8.4 \pm 0.2) \mu\text{m}$ and $y = (5.5 \pm 0.2) \mu\text{m}$, respectively, and is tilted by $\beta = (31 \pm 1)^\circ$ with respect to the surface normal [Fig. 7.1].

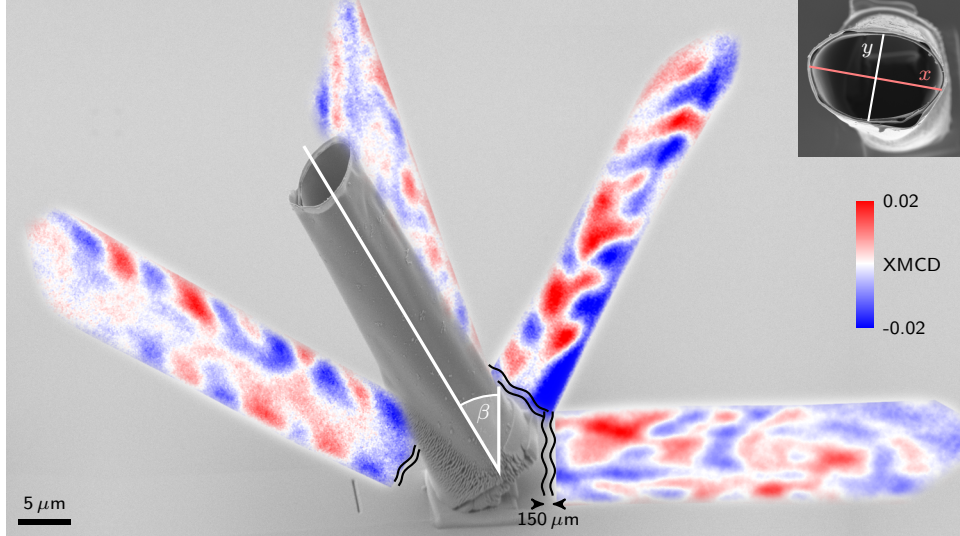


Fig. 7.1.: *Electron micrograph of a vertically fixed Ni tube with circulating magnetization overlaid with XMCD shadow contrast patterns recorded with T-XPEEM at various projection angles. The projected patterns from the top 10 μm of the tube are imaged on the substrate 150 μm away from the tube location (indicated by wiggly lines). Each projection pattern reveals distinct features due to tilt $\beta \approx 31^\circ$, eccentricity and oblique illumination that require a correlation with XMCD contrast simulations. The lengths of major and minor axis are $x = (8.4 \pm 0.2) \mu\text{m}$ and $y = (5.5 \pm 0.2) \mu\text{m}$, respectively. (Taken from [65])*

The spatial orientation of the tube with respect to the X-ray beam propagation direction inside the XPEEM is determined by analyzing the angle-dependent projection of the elliptical cross-section of the tube onto the planar substrate [Fig. 7.2(a)]. Tube orientations with a tilt towards and away from the X-ray beam incidence direction are referred to as $\alpha = 0^\circ$ and $\alpha = 180^\circ$, respectively. The long focal length of the X-ray beam of 32 cm provides equal foci for front and back side of the tube and ensures a parallel projection of the magnetization texture. Although the magnetic domains do not change during illumination, their projections at various angles reveal distinct features in both domain shape and contrast level [Fig. 7.1].

The experimental data is correlated with XMCD contrast simulations carried out using the POV-Ray (Persistence of Vision Raytracer) framework [274]. The rolled-up nanomembrane is approximated as a closed hollow cylinder with one winding because of tightly rolling up along the edge and magnetostatic interwinding coupling (Section 6.2) [131, 137]. A parallel light source resembling the propagating X-ray beam projects the magnetic spin texture onto the planar substrate. To each magnetization inside the tubular object an effective absorption coefficient is assigned according to (6.3). The spatial orientation of tube and magnetization is considered by applying various rotation matrices. Projections

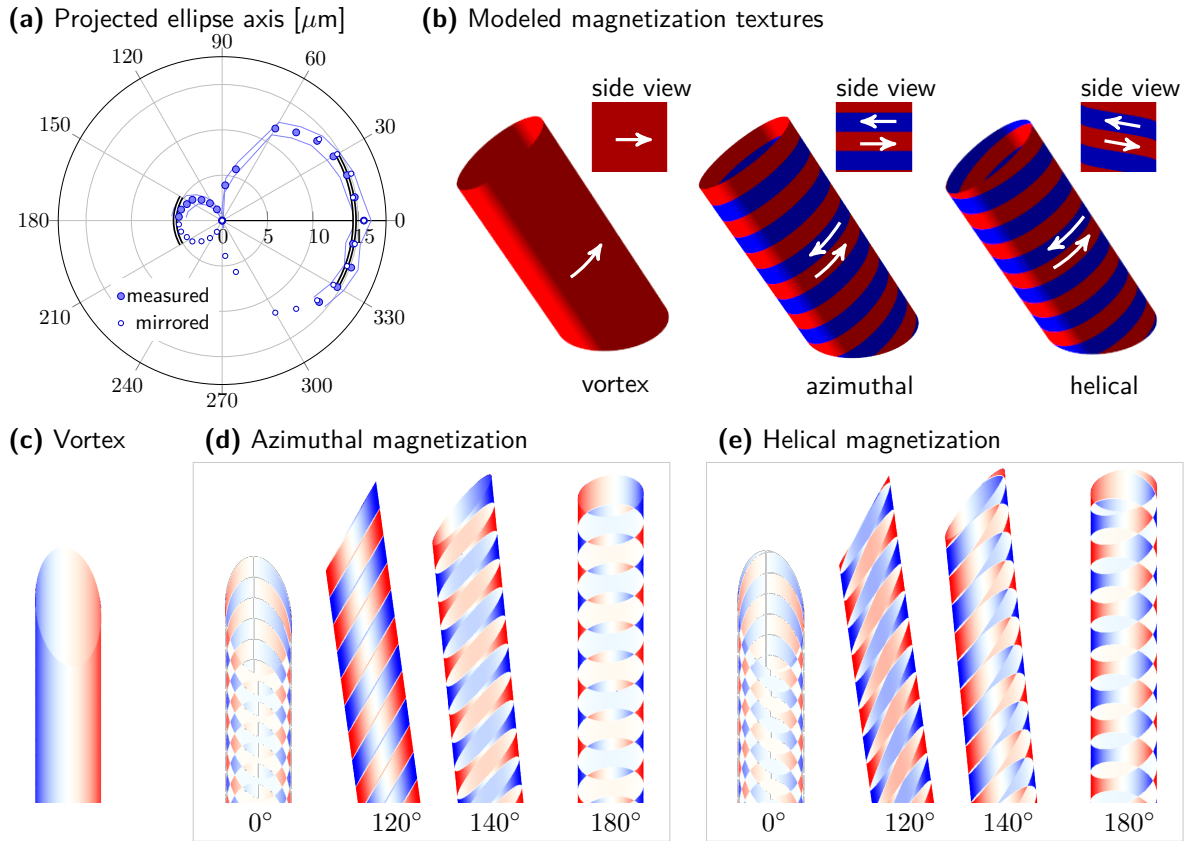


Fig. 7.2.: Modeling the 2D projections of magnetic patterns to discriminate magnetization textures. (a) Angle dependence of the projected ellipse axis along the beam when illuminating at 74° with respect to the surface normal in XPEEM to precisely determine the tube orientation. For 0° and 180° , the tube is tilted towards and away from the beam, respectively. The double lines indicate the analytically calculated values. (b) Possible magnetization textures within the rolled-up nickel nanomembrane approximated as hollow cylinder. In addition to the 3D perspective view, the side views are shown as insets. Tube geometry is taken from experiment; Domain width is $1\mu\text{m}$. Panels (c), (d) and (e) depict the simulated 2D projections of vortex, azimuthal and helical magnetization for various projection angles, respectively. The 2D projection of the vortex texture is angle-independent. Whereas magnetic patterns in (d) and (e) appear similar for projection angles close to 0° , a distinct difference between both textures occurs for angles larger than 90° . (Taken from [65])

at different angles are taken into account by altering the X-ray propagation direction \mathbf{k} . Although the present approach performs only one iteration by assuming a homogeneous thickness of the tube to ensure time efficiency, architectures with local thickness variations may be simulated by conducting multiple iterations with smaller discretization.

According to the experimental tube geometry, two different periodic magnetic domain patterns with an easy axis curling around the symmetry axis, namely azimuthal and helical magnetization [Fig. 7.2(b)], and various pitch sizes are modeled [65]. Domains with red

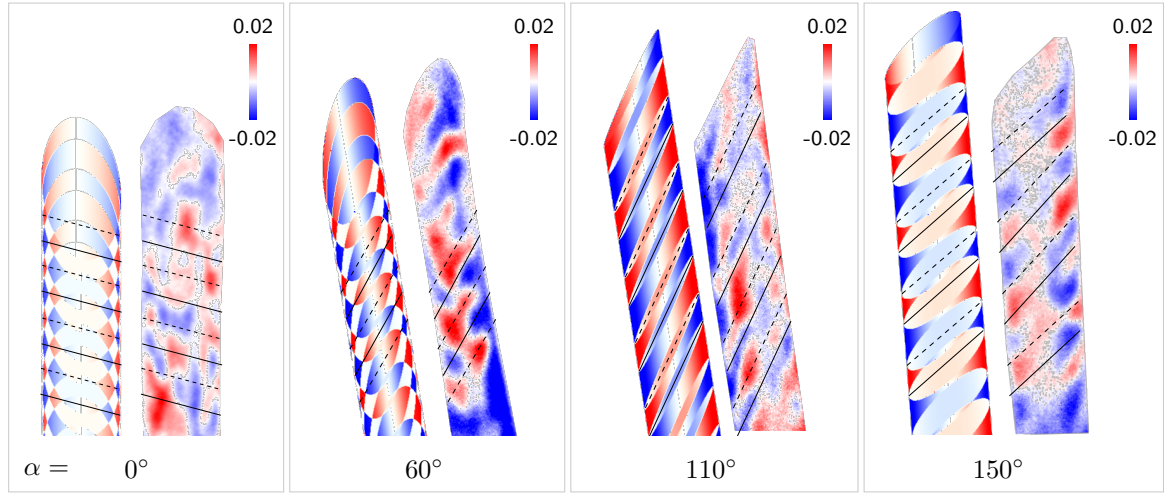


Fig. 7.3.: Correlation of experimental with simulated XMCD contrast of azimuthal magnetization textures with alternating domain widths [$0.9\ \mu\text{m}$ & $1.2\ \mu\text{m}$ (11% & 15%)] at different projection angles. The projections reveal distinct and complex patterns that can only be assigned by simulation correlation to the corresponding magnetization textures. Solid lines serve as guide to the eye. (Taken from [65])

and blue shading refer to a clockwise and counterclockwise circulating magnetization, respectively. The uniform vortex state (azimuthal magnetization without a domain wall) causes a dipolar XMCD contrast [Fig. 7.2(c)] not observed in experiment. An azimuthal magnetization generates a reversed contrast on opposite sides of the tube [Fig. 7.2(d)] similar to that observed in experiment [Fig. 7.1], while for helices with smallest pitch, the same contrast is expected [Fig. 7.2(e)]. On this basis, a helical magnetization can certainly be excluded. The simulated contrast of an azimuthal periodically alternating domain configuration is shown in Figure 7.3 and agrees well with experiment. For better visualization, solid and dashed lines serve as a guide to the eye. The magnetic domain configuration matching best with experiment is considered to be the true configuration. Distinct features for different projection angles are visible: At $\alpha = 0^\circ$, the overlap is the largest leading to many small separated domains with the weakest signal due to the smallest scalar product between \mathbf{M} and \mathbf{k} . With increasing angles both contrast and domain size ascend. At $\alpha = 110^\circ$, the X-ray propagation direction is almost perpendicular to the axis of the tilted tube resulting in stripe domains. The apparently bent blue domain in the experimental data can be explained as the blue contrast on each side of the tube originates from two adjacent domains that are connected by a bluish elliptical overlap. These stripes transform into domains located at the edge of the tube when reaching projection angles close to 150° . At $\alpha = 180^\circ$, the contrast in the center of the tube returns while preserving the edge domains. Based on the appearance of these features and their evolution as a

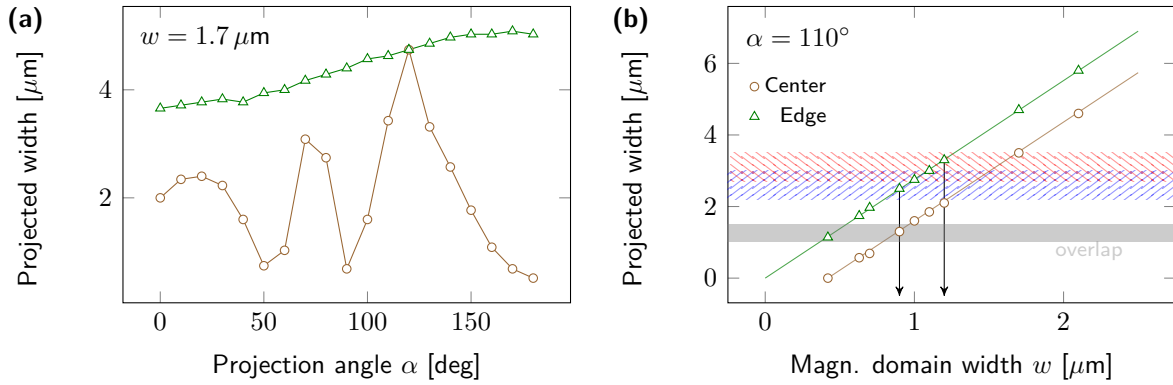


Fig. 7.4.: Angle dependence of domain widths in XMCD contrast patterns. (a) Angle dependence of the projected domain width taken at the edge and the central region of the shadow contrast. The oscillatory behavior increases with decreasing domain width or approaching the center. (b) Linear dependence of the projected width on the magnetic domain width. Experimental data (indicated shaded areas) suggests a periodically alternating domain width. (Taken from [65])

function of the projection angle, the presence of the 3D azimuthal magnetization pattern within the tube is confirmed.

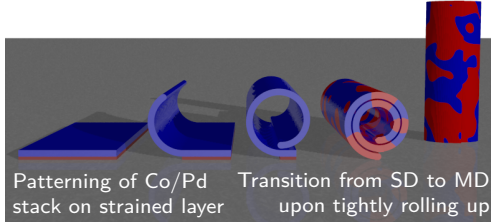
The sensitivity of the 2D projection on domain size and projection angle is shown for $w = 1.7 \mu\text{m}$ and $\alpha = 110^\circ$, respectively, in Figure 7.4. The pitch of the projected domains at the edge of the XMCD contrast is equal to that of the magnetization texture multiplied by a factor of 2.76. Because of tilt and eccentricity of the object, regions of the projected images with vanishing and existing XMCD contrast exhibit an oscillatory behavior that increases with decreasing width of the magnetic domains or approaching the central region of the projected pattern [Fig. 7.4(a)]. This angle dependence demonstrates the fundamental importance of acquiring and correlating projections at various angles to determine the spatial orientation of structure and magnetic domains. The experimental data of clockwise and counterclockwise circulating domains at 110° is inserted into Figure 7.4(b) to determine the widths of the magnetic domains. The corresponding domain configuration is an alternation of $(0.9 \pm 0.2) \mu\text{m}$ and $(1.2 \pm 0.2) \mu\text{m}$ wide azimuthal domains. These values represent 11% and 15% the major symmetry axis, respectively [inset in Fig. 7.1]. The corresponding remanent magnetization of the top side of the tube of $0.4 M_s$ coincides reasonably well with that measured by MOKE magnetometry [Fig. 6.1(b)]. Note that for those simple magnetic domain patterns with straight domain walls, a correlation based analysis of a set of 2D projections is sufficient to retrieve 3D information even if the object is tilted with respect to the rotation axis.

7.2. Radially Magnetized Tubular Architectures

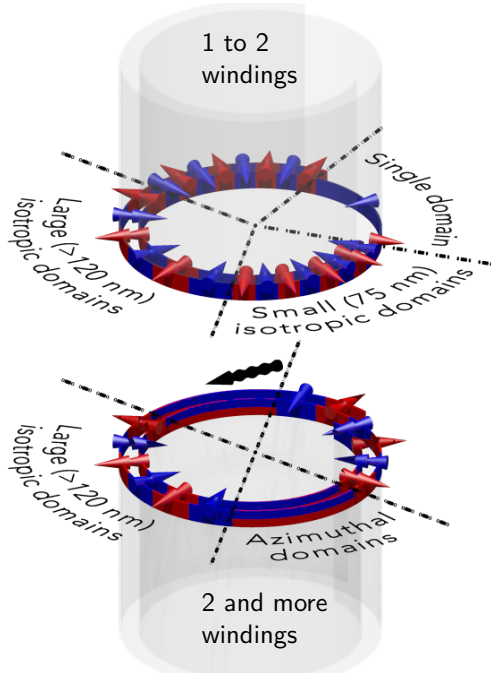
The aforementioned complexity of the XMCD contrast evolution due to oblique illumination in T-XPEEM can be avoided by orthogonally projecting the magnetization onto a CCD screen using TXM (Section 4.3.2). The lack of a preferential domain wall orientation in out-of-plane magnetized Co/Pd films prohibits a clear identification of the magnetization based on correlation as done in Section 7.1 for circulating magnetization textures and demands a new algorithm to be developed. Using 20 nm-thick strained Ti layers, tubular objects with a diameter $\varnothing \approx 2 \mu\text{m}$ and a low X-ray absorption of $\approx 20\%$ per winding at the Co L_3 edge are prepared (Section 3.2). Rolling up non-rectangular nanomembranes with an out-of-plane magnetization into tightly wound thin films allows to simultaneously investigate homogeneously magnetized (one winding) and multi domain (multiple windings) states at remanence due to magnetostatic interaction between adjacent windings [Fig. 7.5(a)]. Analyzing the magnetic field-driven reversal process confirmed the imprint of magnetic domains in every adjacent winding by observing a collective switching. This way, the complexity of projected patterns could be stepwise increased to develop and verify MXT (Section 4.4).

Selected remanent states after initial saturation ($H \approx 200 \text{ kA/m}$) along 180° are shown in Figure 7.5(b). Two sets of drift-corrected 2D projections taken at angles from 0° to 180° with step size $\delta = 4^\circ$ are assembled into a 3D pattern of the tube and presented as movies in Reference [65]. The projected patterns reveal strong contrast in the center with three different contrast levels referring to domains on front and back side of the tube with magnetization vectors pointing in- or outside the tube [Fig. 7.5(b)]. The corresponding ambiguity of states prohibits the use of conventional microscopy of a single 2D projection as described in Section 4.4 [Fig. 4.8]. An identification of the local magnetization on front and back side of the tube can exclusively be given by a proper analysis of the magnetic contrast evolution with varying projection angle [Fig. 7.5(b)]. For this sake, structural geometry and orientation of the magnetic film need to be determined applying conventional scalar tomography as done in Figure 7.6 in collaboration with Dr. D. Parkinson. Note that reconstructing the magnetic domain patterns fails due to neglecting the vector property of the magnetization.

(a) Preparation of radially magnetized tubes



(c) Schematics of magnetic domains



(b) Reconstruction procedure

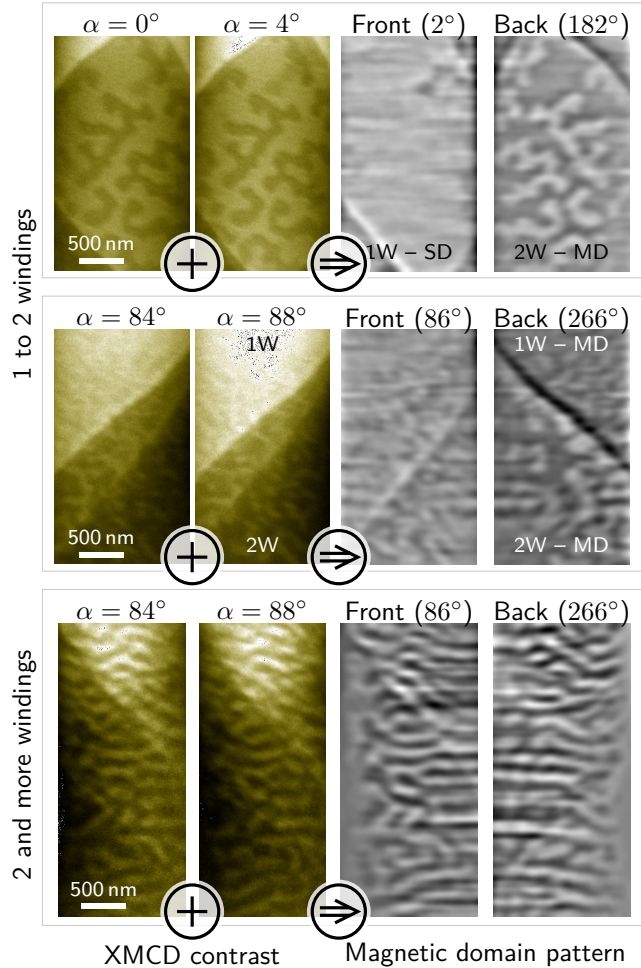


Fig. 7.5.: Fabrication and characterization of radially magnetized tubes. (a) Preparation of radially magnetized tubes via rolling up out-of-plane magnetized Co/Pd multilayer stacks. The initial single domain (SD) state transforms into a multi domain (MD) state upon tightly rolling up. Normal magnetization component is indicated by red and blue. (b) Remanent state of an out-of-plane magnetized rolled-up nanomembrane with $2\ \mu\text{m}$ diameter (field initially applied along 180°) visualized in MTXM. Dark and bright contrast refer to strong and weak absorption, and a magnetization pointing outside and inside the tube, respectively. The magnetization is reconstructed by analyzing the evolution of magnetic contrast with varying projection angle α , e.g. between α and $\alpha + 4^\circ$. Regions with one and two windings are indicated by 1W and 2W, respectively. (c) Schematic illustration of the magnetic domain patterns in tightly wound rolled-up nanomembranes. Large and small domains form along and perpendicularly to the field direction, respectively. A multi domain state wrapping around the whole tube exhibits azimuthally aligned domains. (Taken from [65])

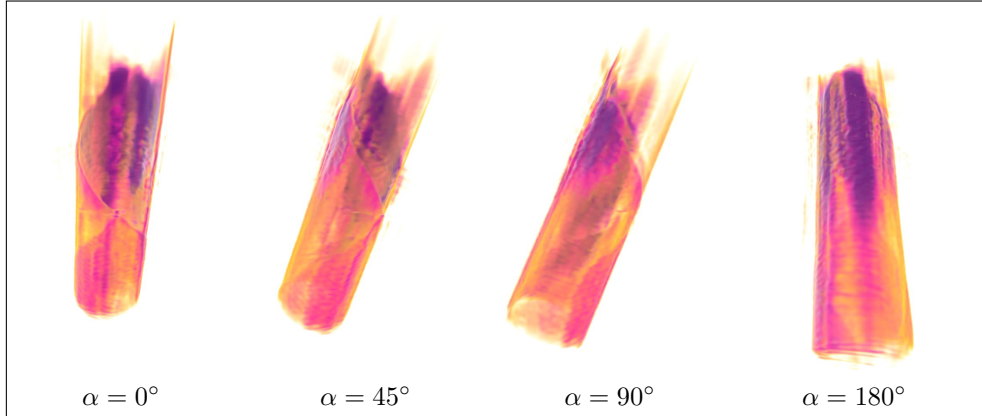


Fig. 7.6.: 3D spatial distribution of the rolled-up nanomembrane obtained by performing conventional scalar tomography. Snapshots at various angles reveal areas with one, two and multiple windings. Despite of these variations, the objects possess a uniaxial cylindrical symmetry. Reconstructing the magnetization patterns fails with scalar tomography. (Taken from [65])

7.2.1. Reconstruction Algorithm

The reason for using several tilt axes in magnetic tomography in contrast to scalar tomography is the vector property of the magnetization leading to three generally independent components. While the approach described by Lade *et al.* [155] requires three sets of projections taken at three orthogonal tilt axes, Phatak *et al.* [156] proposed a reconstruction algorithm of the magnetic induction \mathbf{B} from two sets exploiting the Maxwell equation $\nabla \cdot \mathbf{B} = 0$. However, these procedures cannot straightforwardly be applied to XMCD based tomography because no phase shift due to interaction with magnetic fluxes is recorded.

The present approach relies on solving systems of linear equations similar to those used by Manke *et al.* [52], which represents a complementary way to reconstruct the data without using the Fourier slice theorem (Section 2.3). The contrast change with varying tilt angle mathematically describes the derivative of the magnetization with respect to the rotation angle. Keeping in mind that XMCD is sensitive to the magnetization component pointing along the X-ray trajectory, the contribution of the magnetization component depending on the rotation axes can be determined. Using tubular architectures with well-defined magnetization orientations, *e.g.* radial or in-plane, provides means to consider 1D or 2D vector fields defined on the surface of the cylinder. In this respect, the determined magnetization component refers directly to the magnetization vector. Thus, data acquisition around one tilt axis coinciding with the symmetry axis of the tube is sufficient.

For contributions from front and back side described by $f(x)$ and $b(x)$ ($\propto \mathbf{Mk}$), respectively, the overall XMCD contrast at projection angle α_n and image position x perpendicularly to the rotation/ symmetry axis reads $I^{\alpha_n}(x) = f(x_n) + b(x_{-n})$ with $\alpha_n = \alpha_0 + n\delta$, $x_n = x + g\left(n\delta\frac{\varnothing}{2}\right)$ and the rotation step size δ . The matrix transformation due to the curvature is taken into account by $g\left(n\delta\frac{\varnothing}{2}\right)$ with a lateral displacement at the very center of $\delta\frac{\varnothing}{2}$ perpendicularly to the symmetry axis. Thus, the XMCD contrast can be disentangled by integrating the difference between projections taken at α_0 and α_1 [65]:

$$\frac{1}{2\delta} [I^{\alpha_0}(x_0) - I^{\alpha_1}(x_{-1})] = \frac{1}{2\delta} [b(x_0) - b(x_0 - \delta\varnothing)] \approx \partial_x b^{(\alpha_0 + \delta/2)}(x_0). \quad (7.1)$$

In this notation, $I^{\alpha_1}(x_{-1})$ is the XMCD contrast at $\alpha + \delta$ shifted by $g\left(-\delta\frac{\varnothing}{2}\right)$ perpendicularly to the symmetry axis to eliminate contributions from the front side. In case of a radially magnetized tube, the accordingly identified magnetization texture is unambiguously defined assuming a constant saturation magnetization. Spin textures with unknown magnetization orientation, such as soft-magnetic materials, require to take projections around another rotation axis. In order to capture the magnetic domains in a correct way the lateral shift $\delta\frac{\varnothing}{2}$ between two subsequent projections must not exceed the domain feature size. For instance, data recorded with rotation step sizes $\delta \approx 4^\circ$ allows to reconstruct features as small as 40 nm at the surface with curvature radii of $1\ \mu\text{m}$ ($1\ \mu\text{m}$ away from the rotation axis). The step size has to be adjusted for each object accordingly to its dimensions and the required resolution. In the present case, the smallest domain size is 75 nm (see below), which can fairly be captured with $\delta = 4^\circ$.

In contrast to manual tracking based on the analysis of multiple projections, the numerical approach requires only two projections when dealing with two surfaces. Drift corrections and pseudo-pattern recognition are included that already offer an assessment of the systematic error due to domain wall creeping during data acquisition and the capability to be applied to more complex samples. Considering multiple projections and solving the corresponding system of linear equations further provides means to discriminate contributions from more than two surfaces (Section 8.2).

7.2.2. Reconstruction of Radial Magnetization Patterns

The accordingly reconstructed magnetization textures of the radially magnetized tubular architecture in the area with one to two windings and more than two windings are shown

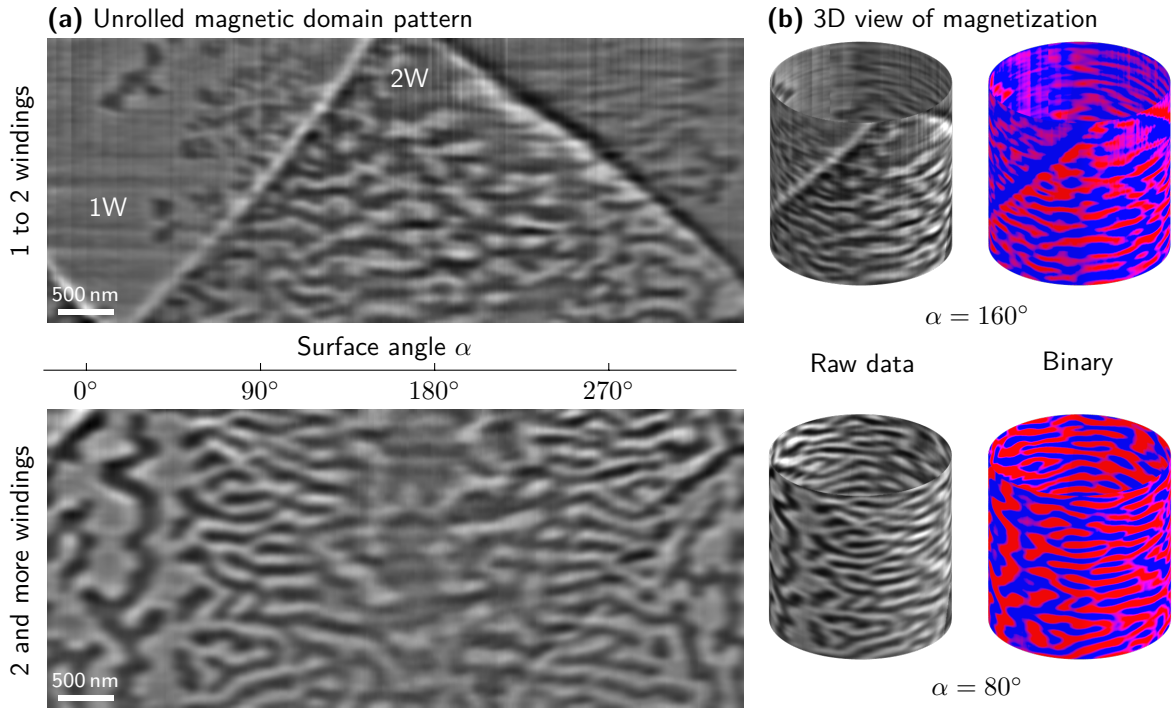


Fig. 7.7.: 3D reconstruction of the magnetization. (a) Unrolled magnetic domain patterns for better visualization. The transition from large isotropic to small azimuthal domains is obvious when approaching surfaces perpendicular to the direction of the initially applied magnetic field (180°). Dark contrast refers to strong absorption and a magnetization pointing outside the tube. (b) 3D view of the magnetization in the thin films with cylindrical shape. In addition to the raw data (gray), the processed binary data with red and blue referring to radial magnetization vectors pointing outside and inside the tube, respectively, are shown. (Taken from [65])

in Figure 7.7 as unrolled magnetic domain patterns and 3D view. Comparing the reconstructed 3D structural information to the corresponding MXT signals allows to correlate the 3D magnetization pattern to the peculiar structure of the object [Fig. 7.7(b)]. The magnetization in areas with non-overlapping windings is in a magnetic single domain state [Fig. 7.7(a), top row], while the area with two windings is split into multiple domains [Fig. 7.7(a)]. Although expected, this information cannot be obtained without performing MXT. Moreover, multi domain states extended into the area with only one winding at the transition region between one and two windings are identified [Fig. 7.7(a), top row]. These domains are stable during the complete measurement indicating that the domain walls are pinned on structural inhomogeneities as known from Co/Pd multilayer stacks. This justifies a pinning dominated displacement of magnetic domain walls when applying external magnetic fields, which can be described using the Kondorsky model of the magnetization reversal [245]. The appearance of the single domain state in the areas with one winding is

perfectly in line with the magnetic hysteresis loop acquired on planar films before rolling up [65]. The number of Co/Pd bilayers is optimized to ensure full remanence of the sample after magnetic saturation. The appearance of the multi domain state in the areas with two windings can be explained by an increased magnetostatic energy of the sample, which favors the multi domain state when doubling the number of Co/Pd repetitions [275]. Note that the uniaxial magnetic anisotropy of the sample is not expected to change due to the Ti spacer between each Co/Pd multilayer stack (winding). Therefore, the reconstructed multi domain pattern in the areas with two windings shed light on the relevance of the magnetostatic coupling between the neighboring windings of the 3D curved magnetic thin films determining its magnetic state.

The magnetic states in Figure 7.7 are obtained after the sample has been exposed to a magnetic field applied perpendicularly to the symmetry axis along $\alpha = 180^\circ$ (perpendicular to the area with single winding). The morphology of the multi domain pattern is clearly changing with the angle featuring large isotropic domains with a size of more than 120 nm on the opposite side of the tube along the field direction and small domains with sizes down to 75 nm in surfaces perpendicular to the magnetic field [Figs. 7.5(c), 7.7]. This difference in morphology of the domain pattern is even more prominent in areas with two or more windings [Fig. 7.7, bottom row]. Regions, which are perpendicular to the direction of the applied magnetic field, reveal narrow magnetic domains with lateral dimensions down to 75 nm along the symmetry axis and an elongation along the circumference of the tube [referred to as azimuthal domains in Fig. 7.5(c)]. The appearance of this peculiar domain pattern can be understood by considering the angular dependence of the switching field of the curved film: The switching field for the Co/Pd multilayers is about 60 kA/m when the field is applied along the easy axis ($\alpha = 0^\circ$). The maximum field of 200 kA/m available at the setup is sufficient to saturate the sample in the angle range $\alpha = (-73 \div 73)^\circ$, taking into account the Kondorsky magnetization reversal process [65]. The excluded regions cannot be saturated since the required field diverges at $\alpha = 90^\circ$. In these areas, the multi domain pattern will be preserved. The observation of narrow azimuthal domains suggests that the applied magnetic field causes a shift of the domain walls in the areas perpendicular to the field direction, which is possible if the domain walls are of Bloch type. Hence, by reconstructing the magnetic domain pattern in the tubular object, we can gain information about the structure of the magnetic domain walls in the sample. Simultaneously, such an arrangement minimizes stray field contributions independently of the lateral expansion. These narrow azimuthal domains propagate around the tube circumference and merge into larger isotropic domains observed at $\alpha \approx 0^\circ$ or $\alpha \approx 180^\circ$

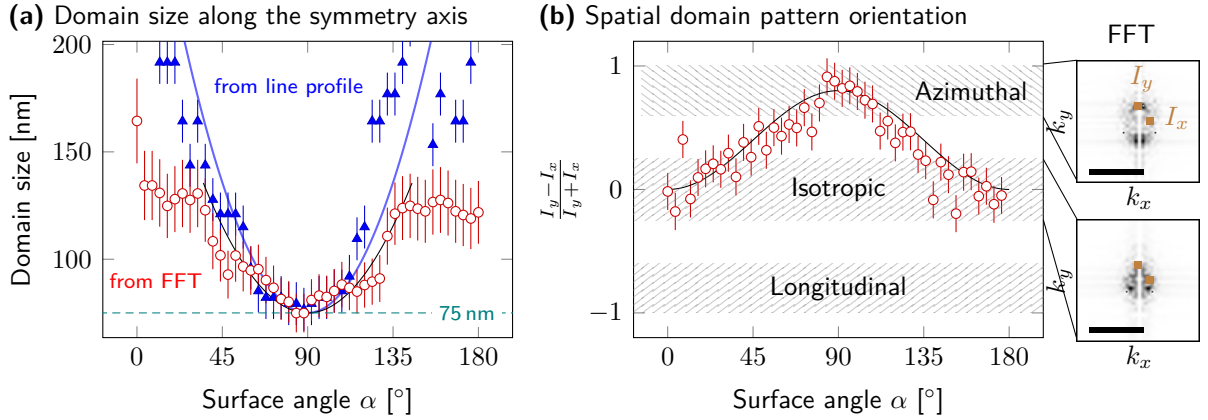


Fig. 7.8.: Angle dependence of the magnetic domain pattern. (a) Domain width in longitudinal direction reveals smallest values at $\alpha \approx 90^\circ$. Data is extracted from line profiles of real space images and from peak positions of FFT images, respectively. (b) Continuous transition from an isotropic/ random domain configuration into an azimuthal ordering obtained from FFT. Solid lines serve as a guide to the eye. Scale bars are 10/nm. (Taken from [65])

[Fig. 7.7]. A similar mechanism is known for in-plane magnetized thin films with spatially varying anisotropy that favors small narrow domains in regions with large switching fields evolving into larger domains in areas with smaller switching fields [271].

Performing 2D fast Fourier transformation (2D FFT) to a selected area ($1 \times 1 \mu\text{m}^2$) of the magnetic domain patterns recorded at different projection angles allows to address both domain morphology and their periodicity [Fig. 7.8]. The largest domain size of 130 nm is observed at $\alpha \approx 0^\circ$ and $\alpha \approx 180^\circ$, which decreases down to (75 ± 9) nm at $\alpha \approx 90^\circ$ [Fig. 7.8(a)]. The 2D FFT data is in good agreement with the domain size extracted from the line profiles along the tube axis. The uncertainty of real space and reciprocal space data is determined by the standard deviation and the resolution in the reciprocal space, respectively. Analyzing the normalized intensity differences of the 2D FFT data, $\frac{I_y - I_x}{I_y + I_x}$ with I_x and I_y extracted from a $1.4 \times 1.4/\text{nm}^2$ area at the location of maximum peak intensity [brown rectangles in the FFT of Fig. 7.8(b)], provides access to the spatial asymmetry of the domain pattern and allows to quantify its morphology [Fig. 7.8(b)]. Surface angles close to $\alpha = 0^\circ$ and $\alpha = 180^\circ$ do not reveal an asymmetry between the FFT intensity I_x and I_y , which agrees with the observed isotropic domain pattern. Approaching projection angles $\alpha \approx 90^\circ$ results in an increase of the asymmetry to positive values indicating a transition to narrow azimuthal domains as visualized in Figure 7.7(b).

7.3. Generalization of the Reconstruction Algorithm

The present approach is a first milestone of 3D imaging magnetic curved surfaces at the mesoscale utilizing XMCD. The major contribution to future developments of MXT is the generalization of the current algorithm (Section 7.2.1) to multiple surfaces and eventually arbitrarily shaped 3D objects. One possible route is to set up and solve a system of linear equations Υ_0^k for XMCD contributions f_k and b_k on front and back side of the magnetic objects, respectively, that add up to the measured intensity as:

$$I^{\alpha_n}(x) = \sum_{j=1}^N [f_j(x_n^j) + b_j(x_{-n}^j)] . \quad (7.2)$$

Each surface is located at r_j causing a j -dependent lateral shift upon rotation $x_n^j = x + g_j(n\delta r_j)$. The shape of the surface is considered, as before, by g_j that needs to be defined analytically or as a rotation matrix based on the 3D reconstruction of the magnetic objects using conventional scalar tomography. Assuming a linear relation of g_j for small δ , the linear system Υ_0^k becomes:

$$\begin{aligned} \Upsilon_0^k &= I^{\alpha_0}(x_0^k) - I^{\alpha_1}(x_{-1}^k) \\ &= [b_k(x_0^k) - b_k(x_{-1}^k - \delta r_k)] \\ &\quad + \sum_{\substack{j=1 \\ j \neq k}}^N [f_j(x_n^j) - f_j(x_{n+1}^j - \delta r_k) + b_j(x_{-n}^j) - b_j(x_{-n-1}^j - \delta r_k)] . \end{aligned} \quad (7.3)$$

For one surface on front and back side ($N = 1$) as studied in Section 7.2.1, (7.3) becomes (7.1). Disentangling contributions from multiple surfaces can be accomplished by recording $\geq N + 1$ projections along similar angles. The smallest step size δ revealing new data is however limited by spatial resolution and depth of focus of the used X-ray microscopy. The solution of (7.3) leads to the magnetization component that depends on the rotation around a certain axis. The implementation of this algorithm and its verification by simulations and experiment is another milestone to be reached. Similarly, other components can be determined by comparing projection at various tilt/ rotation angles.

7.4. Conclusion

The projected XMCD signals of tubular magnetic thin films were recorded with T-XPEEM and MTXM, and analyzed for various projection angles around one rotation axis coinciding with the symmetry axis. Using tubular curved thin films with well-defined magnetization orientation provided the minimized experimental effort while offering means to reconstruct the magnetic domain pattern from a single data set. This simplification is in general not possible due to an underdetermination of the parameter space of the magnetization vector in contrast to scalar densities. While the reconstruction with conventional scalar tomography algorithm fails due to the neglect of the vector property of the magnetization, MXT revealed properly the 3D magnetization texture.

Circulating magnetization patterns were identified by correlation with XMCD contrast simulations of azimuthal and helical magnetization configurations. A periodic commensurable domain pattern throughout the windings was observed that is attributed to circulation sense of the magnetization around the symmetry axis, straight domain wall orientation and magnetostatic interwinding interaction. The absence of a preferential domain wall orientation and the corresponding ambiguity of states in more complex systems like radially magnetized Co/Pd tubes required to retrieve the magnetization directly from the XMCD contrast. Analyzing the evolution of magnetic domains as a function of the projection angle provided means to disentangle contributions from either surface and to reconstruct the magnetization from its derivative perpendicular to the rotation axis. This way, the remanent states in radially magnetized tubular architectures were visualized providing means to quantify magnetic domain patterns. Depending on the magnetic field direction with respect to the surface angle and the effective out-of-plane magnetic anisotropy, different kinds of magnetic domain patterns with distinct morphology and feature sizes down to 75 nm were observed.

The present approach represents a platform to visualize magnetization textures in 3D curved magnetic thin films that can be extended to multiple surfaces with virtually any shape by implementing further algorithms. Setting up and solving a system of linear equations based on multiple projections may be applied to reconstruct magnetic domains at various surfaces. The realization will be the scope of future works.

The present results are summarized in [65].

8. Conclusion & Outlook

8.1. Conclusion

Within the last years, 3D curved magnetic surfaces have attracted much attention in both theoretical and experimental research due to striking properties [31–33, 35, 38, 39] originating from curvature-induced contributions to the magnetic exchange energy [28, 29]. In addition to well-established magnetometry [43, 44], FMR [82, 131, 136] and MR [42, 133] measurements, visualization of magnetic domain patterns is of great importance since they determine the system's response to external stimuli. Magnetic neutron tomography [51, 52] and electron-based 3D imaging, such as electron holography [53–56] and vector field electron tomography [57, 58], are well-established techniques to investigate macroscopic and nanoscopic samples, respectively. However, visualization of nanoscopic domains in mesoscopic samples is not provided by these techniques.

The goal of this thesis was to develop magnetic X-ray tomography (MXT), a visualization technique with nanometer spatial resolution based on XMCD as element-specific contrast mechanism with full-field microscopy, *i.e.* MTXM and XPEEM. While the XMCD contrast of planar films can usually be interpreted as the magnetization component, 3D objects like curved surfaces with local magnetization textures of possibly different orientation generate net XMCD signals that do not represent the magnetization component. Owing to the vector property of the magnetization, the XMCD contrast is a non-additive value that demands knowledge about structure and magnetization of the system under investigation.

Without losing generality, two distinct structural geometries were investigated in the scope of this thesis, namely magnetic cap structures with one curved surface and magnetic tubes with two or more surfaces, referring to the number of magnetic layers in radial direction. Depositing onto curvature templates or rolling up strained thin films into cylindrical

objects provided tunable diameter and number of windings as well as various kinds of materials including NiFe alloys and out-of-plane magnetized Co/Pd. Permalloy cap structures stabilized highly deterministic magnetic spin textures, such as magnetic vortex and onion states [83? –85] as well as donut and spiral states when exchange coupled to out-of-plane magnetized Co/Pd multilayers [115], with distinct XMCD contrast patterns, which could be understood by analyzing "top view" images. An oblique illumination of the 3D objects in T-XPEEM further led to the so-called XMCD shadow contrast at the back side of the object [85, 137]. Its enlarged spatial resolution along the X-ray propagation direction due to a non-orthogonal projection was exploited to identify magnetic states below the resolution limit of the used microscope. Phase diagrams for both hemispherical and cylindrical cap structures were assembled based on the analysis of the XMCD contrast that agree well with those derived from micromagnetic simulations and magnetometry measurements [84? , 85].

The impact of multiple surfaces with different magnetization patterns along the X-ray beam propagation direction on the resulting XMCD patterns is significant as it may be altered by partial or entire compensation depending on magnetization configuration, incidence angle and film thicknesses [83, 85, 115, 137]. The increased complexity in 3D curved surfaces due to contributions from either side was approached by fabricating rolled-up magnetic NiFe nanomembranes resembling spirals (loosely wound) or hollow tubes (tightly wound) with well-defined magnetization orientations (easy axes) [132, 133, 137]. The full set of measurement techniques, including magneto-optical Kerr microscopy, magnetometry, magnetoresistance measurements, and SEM for structural characterization, was applied to assess the magnetic properties. Magnetic domain patterns, magnetic anisotropy and magnetoresistive response were tailored by adjusting shape of the thin film and magnetostriction constants of the NiFe alloy [132, 133]. The magnetostatic interwinding coupling was modified by changing the spatial separation between adjacent soft-magnetic surfaces and investigated on-chip and as a function of external magnetic fields using T-XPEEM [137], mimicking a performance check of already on-chip integrated devices with magnetic functionality before and after encapsulation.

For specific magnetization textures, the entire 3D domain pattern and even the magnetization reversal could be retrieved from 2D projections taken at the same projection angle [137, 223]. Generally, this approach is insufficient to derive the spatial distribution of arbitrary magnetization configurations. For this purpose, tomographic imaging is required with a complete set of projections. The capability of MXT was exemplarily demonstrated by

reconstructing the magnetization configurations in circulating and radially magnetized 3D surfaces with cylindrical shape and various number of windings. This way, characteristics of two distinct magnetic domain patterns have been obtained. The peculiarity of using systems with uniaxial structural symmetry and defined magnetic easy axes allowed for reconstructing the magnetization textures from one set of projections around the symmetry axis [65]. Analyzing the contrast change as a function of the projection angle, remanent states with feature sizes down to 75 nm were retrieved, that had not been possible with conventional scalar tomography reconstruction due to the neglect of the vector property of the magnetization. By these means, the dependence of the domain morphology on surface angle with respect to the initially applied magnetic field and number of windings could be studied and addressed for the first time.

8.2. Outlook

Magnetic X-ray Tomography

Providing means to study samples with thicknesses up to 200 nm, MXT closes the gap between investigating 3D magnetic nanostructures and bulky crystals using electron-based 3D imaging and neutron tomography, respectively. Composite materials with even larger thickness may be investigated element specifically due to an effectively reduced absorption cross-section at resonance. A successful establishment of MXT relies on three major aspects, namely generalization of the present algorithm, application to various sample architectures and realization of a 3D rotation stage in the microscope. The latter requirement is technically challenging due to a fixed rotation axis in T-XPEEM [200] and a spatial separation of merely 2 mm between both zone plates in TXM [196]. The realization may still be possible since tilts around two additional preferentially orthogonal rotation axes would be sufficient for most cases. I envision that the future development of MXT will strongly contribute to the understanding of fundamental mechanisms in magnetic 3D curved surfaces, including performance optimization of cylindrical structures for magnetoencephalography [138], curvature- and topology-driven effects in spirals [39], Möbius bands and tubes, and to the characterization of 3D-shaped mesoscopic objects, such as core-shell particles, buried interfaces and 3D heterostructures, with nanometer spatial resolution.

Nevertheless, MXT may right away be applied to visualize domain patterns in multicom-

ponent tubular surfaces with interacting or non-interacting magnetic subsystems. An important aspect to verify the developed (to be developed) algorithm is to provide a sample that possesses multiple magnetization orientations on the surface. Using heterostructures consisting of the same materials, *e.g.* Ni (in-plane) and Ni/Co multilayers (out-of-plane) [74–76], offers this possibility as well as a verification by imaging at the Co L_3 edge.

Sample Architectures

The fabrication of curved heterostructures by tightly rolling up provides means to assemble magnetic field-tunable metamaterials based on magnonic excitations that function as hyperlenses with cylindrical shape [276–279]. On the other hand, rolling up magnetic honeycomb lattices [163] into cylindrical objects with well-defined orientation could result in a 3D magnonic crystal, which offers a magnetic field control over the energy band gaps. Aside from these fundamental aspects, tubular objects may serve as highly sensitive giant magnetoimpedance-based sensors with low magnetic anisotropy and azimuthal magnetization [138], or as transport channels for magnetic particles (containing cells) with alternating longitudinal magnetization of exchange bias layers by moving inhomogeneous stray fields originating from the domain walls along the tube axis [280].

Cap structures may provide a very first experimental proof by static imaging of curvature-driven modifications to magnetization reversal dynamics of soft-magnetic vortex states originating from a circulation-dependent switching [36, 116]. The present approach of imprinting non-collinear spin textures is currently limited to immobile skyrmionic core textures due to spatial confinement to cap or disk. However, this restriction may be overcome by stabilizing these magnetization configurations in extended non-planar honeycomb lattices [163], which is also appealing for magnonic and spintronic applications. A demonstration of field- or current-driven displacement will require further optimization of structural and magnetic properties.

Self-propulsion of soft-magnetic Janus micromotors by means of magnetically induced thermophoresis limits the amplitude of the *ac* magnetic field to the vortex annihilation field. This restriction can be overcome by adding an out-of-plane magnetized film to the thick soft-magnetic layer. Avoiding any interlayer exchange coupling by choosing a thick spacer, keeps both subsystems independent of each other [115]. Distinct resonant frequencies for both subsystems would ensure a selected excitation of the soft-magnetic layer and larger

velocities.

A. Appendix

A.1. Versatility of Cross-Beam Workstation

The cross-beam workstation (NVision40, Zeiss), consisting of two individual e-beam and focused ion beam (FIB) columns and two in-lens detectors, offers aside from high-resolution scanning electron microscopy (SEM) [281] special features, such as lithography, deposition, slicing, mechanical manipulation and electrical measurements. A variable field emission electron source allows for probing all kinds of materials. Detecting secondary electrons (SE) and back-scattered electrons (BSE) enables the mapping of morphology and of chem-

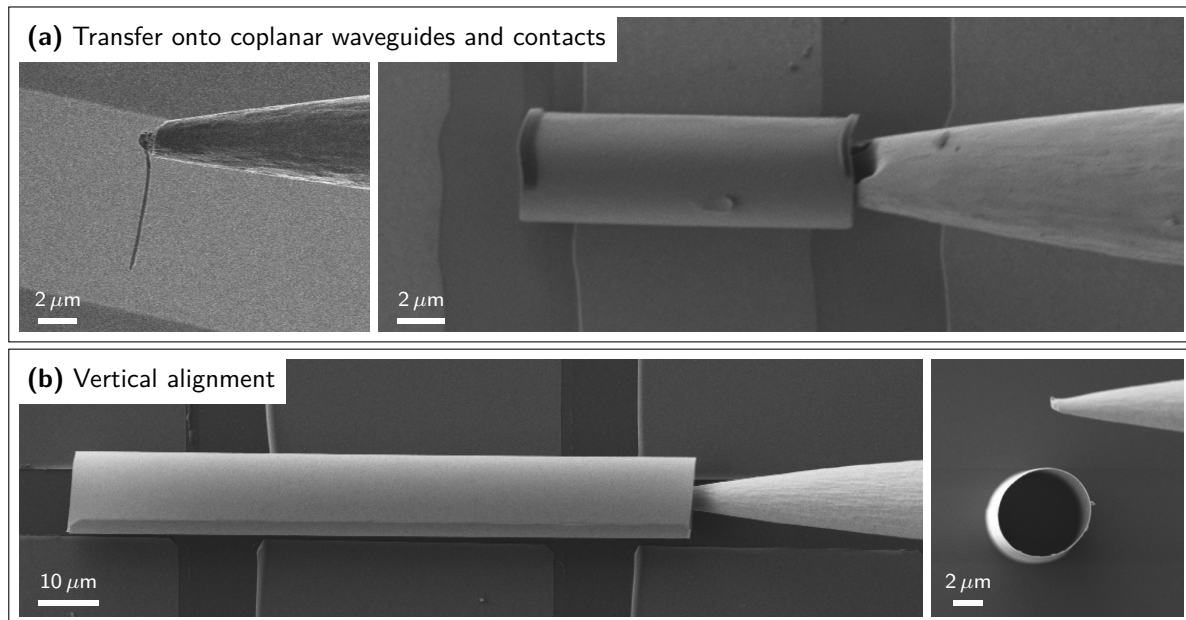


Fig. A.1.: Manipulating and transferring cylindrical objects with a micromanipulator inside a cross-beam workstation. (a) Transfer of magnetic nanorods ($\varnothing = 100 \text{ nm}$) and rolled-up nanomembranes onto coplanar wave guides. (b) Vertical alignment of $100 \mu\text{m}$ -long tubes with a diameter of about $8 \mu\text{m}$.

ical constitution at the nanoscale, respectively. Slicing to prepare cross-sections or to define lateral dimensions is done by utilizing FIB etching at high current ($\gtrsim 1$ nA). Electric contacts and mechanical anchors to tubular objects can be realized by FIB assisted metal deposition of Pt when operating at a low current $[(1 \div 10)$ pA]. Mechanical manipulation of spherical and tubular architectures, including rotation, positioning onto electric contacts or coplanar waveguides [Fig. A.1(a)], and vertically aligning tubes [Fig. A.1(b)], is accomplished using a tungsten tip mounted onto a micromanipulator (MM3A-EM, Kleindiek Nanotechnik).

A.2. Lithographical Patterning

Lithography on photo resistive polymer films is the most commonly used technique in industry and research to define lateral dimensions of nano- and microstructures. In this thesis, all relevant patterning presented in this thesis is achieved by optical lithography, including sacrificial and strained layers for rolling up, electric contacts for magnetoresistance measurements, coplanar waveguides for stroboscopic investigations and opening windows for particle self-assembly. Most of the work is done *via* lift-off, which removes already deposited layers from the substrate by resolving the underlaying photoresist. For this sake, a negative photoresist (AZ-5214E, MicroChemicals) is used that provides for optimized exposure and development conditions an undercut of $\gtrsim 2 \mu\text{m}$. The undercut is crucial for a complete removal even without ultrasonication when handling nanomembranes. The following procedure is used:

1. Spin coating of AZ-5214E at 6000 rpm ($d \approx 1.1 \mu\text{m}$)
2. Prebaking at 90°C for 4 min
3. First exposure with mask for 2 s (MJB4, Süss MicroTec) or 4.5 ms (μPG 501, Heidelberg Instruments)
4. Reversal bake at 120°C for 2 min
5. Flood exposure for 30 s (MJB4)
6. Film deposition
7. Lift-off using acetone or N-Methyl-2-pyrrolidone

Different top layers, such as Si, Cu, Cr, Si_3N_4 nanomembranes, require fine tuning of the first exposure time due to a modified reflexion and thus cross linking of the polymer.

Bibliography

- [1] I. E. Dzyaloshinskii, *Thermodynamic theory of weak ferromagnetism in antiferromagnetic substances*. Sov. Phys. JETP **5**, 1259 (1957).
- [2] T. Moriya, *Anisotropic superexchange interaction and weak ferromagnetism*. Phys. Rev. **120**, 91 (1960).
- [3] A. N. Bogdanov and D. A. Yablonskii, *Thermodynamically stable "vortices" in magnetically ordered crystals. the mixed state of magnets*. Sov. Phys. JETP **68**, 101 (1989).
- [4] U. K. Roessler, A. N. Bogdanov, and C. Pfleiderer, *Spontaneous skyrmion ground states in magnetic metals*. Nature (London) **442**, 797 (2006).
- [5] X. Z. Yu, Y. Onose, N. Kanazawa, J. H. Park, J. H. Han, Y. Matsui, N. Nagaosa, and Y. Tokura, *Real-space observation of a two-dimensional skyrmion crystal*. Nature (London) **465**, 901 (2010).
- [6] S. X. Huang and C. L. Chien, *Extended skyrmion phase in epitaxial FeGe(111) thin films*. Phys. Rev. Lett. **108**, 267201 (2012).
- [7] N. Kanazawa, Y. Onose, T. Arima, D. Okuyama, K. Ohoyama, S. Wakimoto, K. Kakurai, S. Ishiwata, and Y. Tokura, *Large topological hall effect in a short-period helimagnet mng*. Phys. Rev. Lett. **106**, 156603 (2011).
- [8] S. Seki, X. Z. Yu, S. Ishiwata, and Y. Tokura, *Observation of skyrmions in a multiferroic material*. Science **336**, 198 (2012).
- [9] A. Fert, V. Cros, and J. Sampaio, *Skyrmions on the track*. Nat. Nano. **8**, 152 (2013).

- [10] N. Nagaosa and Y. Tokura, *Topological properties and dynamics of magnetic skyrmions*. Nat. Nano. **8**, 899 (2013).
- [11] D. A. Allwood, G. Xiong, M. D. Cooke, C. C. Faulkner, D. Atkinson, N. Vernier, and R. P. Cowburn, *Submicrometer ferromagnetic not gate and shift register*. Science **296**, 2003 (2002).
- [12] S. S. P. Parkin, M. Hayashi, and L. Thomas, *Magnetic domain-wall racetrack memory*. Science **320**, 190 (2008).
- [13] D. A. Allwood, G. Xiong, C. C. Faulkner, D. Atkinson, D. Petit, and R. P. Cowburn, *Magnetic domain-wall logic*. Science **309**, 1688 (2005).
- [14] M. A. Ruderman and C. Kittel, *Indirect exchange coupling of nuclear magnetic moments by conduction electrons*. Phys. Rev. **96**, 99 (1954).
- [15] T. Kasuya, *A theory of metallic ferro- and antiferromagnetism on zener's model*. Progress of Theoretical Physics **16**, 45 (1956).
- [16] K. Yosida, *Magnetic Properties of Cu-Mn Alloys*. Phys. Rev. **106**, 893 (1957).
- [17] S. Heinze, K. von Bergmann, M. Menzel, J. Brede, A. Kubetzka, R. Wiesendanger, G. Bihlmayer, and S. Blugel, *Spontaneous atomic-scale magnetic skyrmion lattice in two dimensions*. Nat. Phys. **7**, 713 (2011).
- [18] N. Romming, C. Hanneken, M. Menzel, J. E. Bickel, B. Wolter, K. von Bergmann, A. Kubetzka, and R. Wiesendanger, *Writing and deleting single magnetic skyrmions*. Science **341**, 636 (2013).
- [19] A. Sonntag, J. Hermenau, S. Krause, and R. Wiesendanger, *Thermal stability of an interface-stabilized skyrmion lattice*. Phys. Rev. Lett. **113**, 077202 (2014).
- [20] P. Grünberg, R. Schreiber, Y. Pang, M. B. Brodsky, and H. Sowers, *Layered magnetic structures: Evidence for antiferromagnetic coupling of fe layers across cr interlayers*. Phys. Rev. Lett. **57**, 2442 (1986).
- [21] S. S. P. Parkin and D. Mauri, *Spin engineering: Direct determination of the*

- ruderman-kittel-kasuya-yosida far-field range function in ruthenium*. Phys. Rev. B **44**, 7131 (1991).
- [22] S. Emori, U. Bauer, S.-M. Ahn, E. Martinez, and G. S. D. Beach, *Current-driven dynamics of chiral ferromagnetic domain walls*. Nat. Mater. **12**, 611 (2013).
- [23] K.-S. Ryu, L. Thomas, S.-H. Yang, and S. Parkin, *Current-driven dynamics of chiral ferromagnetic domain walls*. Nat. Nano. **8**, 527 (2013).
- [24] G. Chen, J. Zhu, A. Quesada, J. Li, A. T. N'Diaye, Y. Huo, T. P. Ma, Y. Chen, H. Y. Kwon, C. Won, Z. Q. Qiu, A. K. Schmid, and Y. Z. Wu, *Novel chiral magnetic domain wall structure in Fe/Ni/Cu(001) films*. Phys. Rev. Lett. **110**, 177204 (2013).
- [25] G. Chen, T. Ma, A. T. N'Diaye, H. Kwon, C. Won, Y. Wu, and A. K. Schmid, *Tailoring the chirality of magnetic domain walls by interface engineering*. Nat. Commun. **4**, 2671 (2013).
- [26] J. Torrejon, J. Kim, J. Sinha, S. Mitani, M. Hayashi, M. Yamanouchi, and H. Ohno, *Interface control of the magnetic chirality in CoFeB/MgO heterostructures with heavy-metal underlayers*. Nat. Commun. **5**, 4655 (2014).
- [27] G. Chen, A. T. N'Diaye, S. P. Kang, H. Y. Kwon, C. Won, Y. Wu, Z. Q. Qiu, and A. K. Schmid, *Unlocking bloch-type chirality in ultrathin magnets through uniaxial strain*. Nat. Commun. **6**, 6598 (2015).
- [28] Y. Gaididei, V. P. Kravchuk, and D. D. Sheka, *Curvature effects in thin magnetic shells*. Phys. Rev. Lett. **112**, 257203 (2014).
- [29] D. D. Sheka, V. P. Kravchuk, and Y. Gaididei, *Curvature effects in statics and dynamics of low dimensional magnets*. J. Phys. A: Math. Theor. **48**, 125202 (2015).
- [30] C. Dietrich, R. Hertel, M. Huber, D. Weiss, R. Schäfer, and J. Zweck, *Influence of perpendicular magnetic fields on the domain structure of permalloy microstructures grown on thin membranes*. Phys. Rev. B **77**, 174427 (2008).
- [31] M. Yan, C. Andreas, A. Kákay, F. García-Sánchez, and R. Hertel, *Fast domain wall dynamics in magnetic nanotubes: Suppression of walker breakdown and cherenkov-like spin wave emission*. Appl. Phys. Lett. **99**, 122505 (2011).

- [32] M. Yan, C. Andreas, A. Kákay, F. García-Sánchez, and R. Hertel, *Chiral symmetry breaking and pair-creation mediated walker breakdown in magnetic nanotubes*. Appl. Phys. Lett. **100**, 252401 (2012).
- [33] J. A. Otalora, J. A. Lopez-Lopez, P. Vargas, and P. Landeros, *Chirality switching and propagation control of a vortex domain wall in ferromagnetic nanotubes*. Appl. Phys. Lett. **100**, 072407 (2012).
- [34] V. P. Kravchuk, D. D. Sheka, R. Streubel, D. Makarov, O. G. Schmidt, and Y. Gaididei, *Out-of-surface vortices in spherical shells*. Phys. Rev. B **85**, 144433 (2012).
- [35] M. Yan, A. Kákay, C. Andreas, and R. Hertel, *Spin-cherenkov effect and magnonic mach cones*. Phys. Rev. B **88**, 220412 (2013).
- [36] M. I. Sloika, V. P. Kravchuk, D. D. Sheka, and Y. Gaididei, *Curvature induced chirality symmetry breaking in vortex core switching phenomena*. Appl. Phys. Lett. **104**, 252403 (2014).
- [37] R. Hertel, *Curvature-induced magnetochirality*. SPIN **03**, 1340009 (2013).
- [38] M. Yan, A. Kákay, S. Gliga, and R. Hertel, *Beating the walker limit with massless domain walls in cylindrical nanowires*. Phys. Rev. Lett. **104**, 057201 (2010).
- [39] C. Ortix, D. Makarov, R. Streubel, E. J. Smith, P. Fischer, O. G. Schmidt, and J. van den Brink, *Emergent toroidization and linear magneto-electric coupling in radially magnetized rolled-up nanomembranes* (2015), in preparation.
- [40] K. Nielsch, R. B. Wehrspohn, J. Barthel, J. Kirschner, U. Gösele, S. F. Fischer, and H. Kronmüller, *Hexagonally ordered 100 nm period nickel nanowire arrays*. Appl. Phys. Lett. **79**, 1360 (2001).
- [41] K. Nielsch, J. Choi, K. Schwirn, R. B. Wehrspohn, and U. Gösele, *Self-ordering regimes of porous alumina: The 10 porosity rule*. Nano Lett. **2**, 677 (2002).
- [42] D. Ruffer, R. Huber, P. Berberich, S. Albert, E. Russo-Averchi, M. Heiss, J. Arbiol, A. Fontcuberta i Morral, and D. Grundler, *Magnetic states of an individual ni nanotube probed by anisotropic magnetoresistance*. Nanoscale **4**, 4989 (2012).

- [43] D. P. Weber, D. Ruffer, A. Buchter, F. Xue, E. Russo-Averchi, R. Huber, P. Berberich, J. Arbiol, A. Fontcuberta i Morral, D. Grundler, and M. Poggio, *Cantilever magnetometry of individual ni nanotubes*. Nano Lett. **12**, 6139 (2012).
- [44] A. Buchter, J. Nagel, D. Ruffer, F. Xue, D. P. Weber, O. F. Kieler, T. Weimann, J. Kohlmann, A. B. Zorin, E. Russo-Averchi, R. Huber, P. Berberich, A. Fontcuberta i Morral, M. Kemmler, R. Kleiner, D. Koelle, D. Grundler, and M. Poggio, *Reversal mechanism of an individual ni nanotube simultaneously studied by torque and squid magnetometry*. Phys. Rev. Lett. **111**, 067202 (2013).
- [45] V. Y. Prinz, V. A. Seleznev, A. K. Gutakovskiy, A. V. Chehovskiy, V. V. Preobrazhenskii, M. A. Putyato, and T. A. Gavrilova, *Free-standing and overgrown InGaAs/GaAs nanotubes, nanohelices and their arrays*. Physica E **6**, 828 (2000).
- [46] O. G. Schmidt and K. Eberl, *Thin solid films roll up into nanotubes*. Nature (London) **410**, 168 (2001).
- [47] C. Deneke, C. Müller, N. Y. Jin-Phillipp, and O. G. Schmidt, *Diameter scalability of rolled-up In(Ga)As/GaAs nanotubes*. Semicond. Sci. Technol. **17**, 1278 (2002).
- [48] Y. Mei, G. Huang, A. A. Solovev, E. B. Ureña, I. Mönch, F. Ding, T. Reindl, R. K. Y. Fu, P. K. Chu, and O. G. Schmidt, *Versatile approach for integrative and functionalized tubes by strain engineering of nanomembranes on polymers*. Adv. Mater. **20**, 4085 (2008).
- [49] P. Cendula, S. Kiravittaya, Y. F. Mei, C. Deneke, and O. G. Schmidt, *Bending and wrinkling as competing relaxation pathways for strained free-hanging films*. Phys. Rev. B **79**, 085429 (2009).
- [50] P. Cendula, S. Kiravittaya, I. Mönch, J. Schumann, and O. G. Schmidt, *Directional roll-up of nanomembranes mediated by wrinkling*. Nano Lett. **11**, 236 (2011).
- [51] N. Kardjilov, I. Manke, M. Strobl, A. Hilger, W. Treimer, M. Meissner, T. Krist, and J. Banhart, *Three-dimensional imaging of magnetic fields with polarized neutrons*. Nat. Phys. **4**, 399 (2008).
- [52] I. Manke, N. Kardjilov, R. Schäfer, A. Hilger, M. Strobl, M. Dawson, C. Grünzweig,

- G. Behr, M. Hentschel, C. David, A. Kupsch, A. Lange, and J. Banhart, *Three-dimensional imaging of magnetic domains*. Nat. Commun. **1**, 125 (2010).
- [53] R. E. Dunin-Borkowski, M. R. McCartney, R. B. Frankel, D. A. Bazylinski, M. Pósfai, and P. R. Buseck, *Magnetic microstructure of magnetotactic bacteria by electron holography*. Science **282**, 1868 (1998).
- [54] S. L. Tripp, R. E. Dunin-Borkowski, and A. Wei, *Flux closure in self-assembled cobalt nanoparticle rings*. Angew. Chem. Int. Edit. **42**, 5591 (2003).
- [55] N. Biziere, C. Gatel, R. Lassalle-Balier, M. C. Clochard, J. E. Wegrowe, and E. Snoeck, *Imaging the fine structure of a magnetic domain wall in a *ni* nanocylinder*. Nano Lett. **13**, 2053 (2013).
- [56] C. Phatak, Y. Liu, E. B. Gulsoy, D. Schmidt, E. Franke-Schubert, and A. Petford-Long, *Visualization of the magnetic structure of sculpted three-dimensional cobalt nanospirals*. Nano Lett. **14**, 759 (2014).
- [57] C. Phatak, A. K. Petford-Long, and M. De Graef, *Three-dimensional study of the vector potential of magnetic structures*. Phys. Rev. Lett. **104**, 253901 (2010).
- [58] T. Tanigaki, Y. Takahashi, T. Shimakura, T. Akashi, R. Tsuneta, A. Sugawara, and D. Shindo, *Three-dimensional observation of magnetic vortex cores in stacked ferromagnetic discs*. Nano Lett. **15**, 1309 (2015).
- [59] J. R. Arnold, J. P. Testa, P. J. Friedman, and G. X. Kambic, *Computed tomographic analysis of meteorite inclusions*. Science **219**, 383 (1983).
- [60] W. D. Carlson and C. Denison, *Mechanisms of porphyroblast crystallization: Results from high-resolution computed x-ray tomography*. Science **257**, 1236 (1992).
- [61] J. H. Kinney, T. M. Breunig, T. L. Starr, D. Haupt, M. C. Nichols, S. R. Stock, M. D. Butts, and R. A. Saroyan, *X-ray tomographic study of chemical vapor infiltration processing of ceramic composites*. Science **260**, 789 (1993).
- [62] J. Carrascosa, F. Chichón, E. Pereiro, M. Rodríguez, J. Fernández, M. Esteban, S. Heim, P. Guttmann, and G. Schneider, *Cryo-x-ray tomography of vaccinia virus membranes and inner compartments*. J. Struct. Biol. **168**, 234 (2009).

- [63] G. Schneider, P. Guttman, S. Heim, S. Rehbein, F. Mueller, K. Nagashima, J. B. Heymann, W. G. Muller, and J. G. McNally, *Three-dimensional cellular ultrastructure resolved by x-ray microscopy*. Nat. Meth. **7**, 985 (2010).
- [64] E. Hummel, P. Guttman, S. Werner, B. Tarek, G. Schneider, M. Kunz, A. S. Frangakis, and B. Westermann, *3d ultrastructural organization of whole chlamydomonas reinhardtii cells studied by nanoscale soft x-ray tomography*. PLoS ONE **7**, e53293 (2012).
- [65] R. Streubel, F. Kronast, P. Fischer, D. Parkinson, O. G. Schmidt, and D. Makarov, *Retrieving spin textures on curved magnetic thin films with full-field soft x-ray microscopies*. Nat. Commun. **6**, 7612 (2015).
- [66] W. Heitler and F. London, *Wechselwirkung neutraler atome und homöopolare bindung nach der quantenmechanik*. Z. Physik **44**, 455 (1927).
- [67] A. Hubert and R. Schäfer, *Magnetic Domains* (Springer, 1998).
- [68] I. E. Dzyaloshinskii, *Theory of helicoidal structures in antiferromagnets*. Sov. Phys. JETP **19**, 960 (1964).
- [69] A. N. Bogdanov and U. K. Röbner, *Chiral symmetry breaking in magnetic thin films and multilayers*. Phys. Rev. Lett. **87**, 037203 (2001).
- [70] L. D. Landau and E. Lifschitz, *Lehrbuch der Theoretischen Physik, Elektrodynamik der Kontinua*, 1st ed. (Akademie Verlag, 1985).
- [71] R. P. Cowburn, D. K. Koltsov, A. O. Adeyeye, M. E. Welland, and D. M. Tricker, *Single-domain circular nanomagnets*. Phys. Rev. Lett. **83**, 1042 (1999).
- [72] Y. Acremann, C. H. Back, M. Buess, O. Portmann, A. Vaterlaus, D. Pescia, and H. Melchior, *Imaging precessional motion of the magnetization vector*. Science **290**, 492 (2000).
- [73] A. Wachowiak, J. Wiebe, M. Bode, O. Pietzsch, M. Morgenstern, and R. Wiesendanger, *Direct observation of internal spin structure of magnetic vortex cores*. Science **298**, 577 (2002).

- [74] G. H. O. Daalderop, P. J. Kelly, and F. J. A. den Broeder, *Prediction and confirmation of perpendicular magnetic anisotropy in Co/Ni multilayers*. Phys. Rev. Lett. **68**, 682 (1992).
- [75] S. Mizukami, X. Zhang, T. Kubota, H. Naganuma, M. Oogane, Y. Ando, and T. Miyazaki, *Gilbert damping in ni/co multilayer films exhibiting large perpendicular anisotropy*. Appl. Phys. Express **4**, 013005 (2011).
- [76] M. Haertinger, C. H. Back, S.-H. Yang, S. S. P. Parkin, and G. Woltersdorf, *Properties of Ni/Co multilayers as a function of the number of multilayer repetitions*. J. Phys. D: Appl. Phys. **46**, 175001 (2013).
- [77] H.-C. Yuan, Z. Ma, M. M. Roberts, D. E. Savage, and M. G. Lagally, *High-speed strained-single-crystal-silicon thin-film transistors on flexible polymers*. J. Appl. Phys. **100**, 013708 (2006).
- [78] D.-H. Kim, J.-H. Ahn, W. M. Choi, H.-S. Kim, T.-H. Kim, J. Song, Y. Y. Huang, Z. Liu, C. Lu, and J. A. Rogers, *Stretchable and foldable silicon integrated circuits*. Science **320**, 507 (2008).
- [79] T. Sekitani, Y. Noguchi, K. Hata, T. Fukushima, T. Aida, and T. Someya, *A rubberlike stretchable active matrix using elastic conductors*. Science **321**, 1468 (2008).
- [80] D.-H. Kim, N. Lu, R. Ma, Y.-S. Kim, R.-H. Kim, S. Wang, J. Wu, S. M. Won, H. Tao, A. Islam, K. J. Yu, T.-i. Kim, R. Chowdhury, M. Ying, L. Xu, M. Li, H.-J. Chung, H. Keum, M. McCormick, P. Liu, Y.-W. Zhang, F. G. Omenetto, Y. Huang, T. Coleman, and J. A. Rogers, *Epidermal electronics*. Science **333**, 838 (2011).
- [81] M. Kaltenbrunner, T. Sekitani, J. Reeder, T. Yokota, K. Kuribara, T. Tokuhara, M. Drack, R. Schwodiauer, I. Graz, S. Bauer-Gogonea, S. Bauer, and T. Someya, *An ultra-lightweight design for imperceptible plastic electronics*. Nature (London) **499**, 458 (2013).
- [82] F. Balhorn, S. Mansfeld, A. Krohn, J. Topp, W. Hansen, D. Heitmann, and S. Mendach, *Spin-wave interference in three-dimensional rolled-up ferromagnetic microtubes*. Phys. Rev. Lett. **104**, 037205 (2010).
- [83] R. Streubel, D. Makarov, F. Kronast, V. Kravchuk, M. Albrecht, and O. G. Schmidt,

- Magnetic vortices on closely packed spherically curved surfaces.* Phys. Rev. B **85**, 174429 (2012).
- [84] R. Streubel, D. J. Thurmer, D. Makarov, F. Kronast, T. Kosub, V. Kravchuk, D. D. Sheka, Y. Gaididei, R. Schäfer, and O. G. Schmidt, *Magnetically capped rolled-up nanomembranes.* Nano Lett. **12**, 3961 (2012).
- [85] R. Streubel, V. P. Kravchuk, D. D. Sheka, D. Makarov, F. Kronast, O. G. Schmidt, and Y. Gaididei, *Equilibrium magnetic states in individual hemispherical permalloy caps.* Appl. Phys. Lett. **101**, 132419 (2012).
- [86] M. Burgess and B. Jensen, *Fermions near two-dimensional surfaces.* Phys. Rev. A **48**, 1861 (1993).
- [87] Y. B. Gaididei, S. F. Mingaleev, and P. L. Christiansen, *Curvature-induced symmetry breaking in nonlinear Schrödinger models.* Phys. Rev. E **62**, R53 (2000).
- [88] P. L. Gaididei, Yu. B. and Christiansen, P. G. Kevrekidis, H. Büttner, and A. R. Bishop, *Localization of nonlinear excitations in curved waveguides.* New J. Phys. **7**, 52 (2005).
- [89] G. Ferrari and G. Cuoghi, *Schrödinger equation for a particle on a curved surface in an electric and magnetic field.* Phys. Rev. Lett. **100**, 230403 (2008).
- [90] M. J. Bowick and L. Giomi, *Two-dimensional matter: order, curvature and defects.* Adv. Phys. **58**, 449 (2009).
- [91] A. M. Turner, V. Vitelli, and D. R. Nelson, *Vortices on curved surfaces.* Rev. Mod. Phys. **82**, 1301 (2010).
- [92] G. Napoli and L. Vergori, *Extrinsic curvature effects on nematic shells.* Phys. Rev. Lett. **108**, 207803 (2012).
- [93] G. Napoli and L. Vergori, *Surface free energies for nematic shells.* Physical Review E **85**, 061701 (2012).
- [94] P. Landeros, O. J. Suarez, A. Cuchillo, and P. Vargas, *Equilibrium states and vortex domain wall nucleation in ferromagnetic nanotubes.* Phys. Rev. B **79**, 024404 (2009).

- [95] P. Landeros and A. S. Núñez, *Domain wall motion on magnetic nanotubes*. J. Appl. Phys. **108**, 033917 (2010).
- [96] A. González, P. Landeros, and A. S. Núñez, *Spin wave spectrum of magnetic nanotubes*. J. Magn. Magn. Mater. **322**, 530 (2010).
- [97] J.-G. Zhu, Y. Zheng, and G. A. Prinz, *Ultrahigh density vertical magnetoresistive random access memory (invited)*. J. Appl. Phys. **87**, 6668 (2000).
- [98] K. W. Chou, A. Puzic, H. Stoll, D. Dolgos, G. Schütz, B. Van Waeyenberge, A. Vansteenkiste, T. Tyliczszak, G. Woltersdorf, and C. H. Back, *Direct observation of the vortex core magnetization and its dynamics*. Appl. Phys. Lett. **90**, 202505 (2007).
- [99] M. Curcic, B. Van Waeyenberge, A. Vansteenkiste, M. Weigand, V. Sackmann, H. Stoll, M. Fähnle, T. Tyliczszak, G. Woltersdorf, C. H. Back, and G. Schütz, *Polarization selective magnetic vortex dynamics and core reversal in rotating magnetic fields*. Phys. Rev. Lett. **101**, 197204 (2008).
- [100] A. Vansteenkiste, M. Weigand, M. Curcic, H. Stoll, G. Schütz, and B. Van Waeyenberge, *Chiral symmetry breaking of magnetic vortices by sample roughness*. New J. Phys. **11**, 063006 (2009).
- [101] M.-Y. Im, P. Fischer, K. Yamada, T. Sato, S. Kasai, Y. Nakatani, and T. Ono, *Symmetry breaking in the formation of magnetic vortex states in a permalloy nanodisk*. Nat. Commun. **3**, 983 (2012).
- [102] N. L. Schryer and L. R. Walker, *The motion of 180° domain walls in uniform dc magnetic fields*. J. Appl. Phys. **45**, 5406 (1974).
- [103] Y. Nakatani, A. Thiaville, and J. Miltat, *Faster magnetic walls in rough wires*. Nat. Mater. **2**, 521 (2003).
- [104] G. S. D. Beach, C. Nistor, C. Knutson, M. Tsoi, and J. L. Erskine, *Dynamics of field-driven domain-wall propagation in ferromagnetic nanowires*. Nat. Mater. **4**, 741 (2005).
- [105] M. Hayashi, L. Thomas, C. Rettner, R. Moriya, X. Jiang, and S. S. P. Parkin,

Dependence of current and field driven depinning of domain walls on their structure and chirality in permalloy nanowires. Phys. Rev. Lett. **97**, 207205 (2006).

- [106] L. Thomas, M. Hayashi, X. Jiang, R. Moriya, C. Rettner, and S. S. P. Parkin, *Oscillatory dependence of current-driven magnetic domain wall motion on current pulse length.* Nature (London) **443**, 197 (2006).
- [107] M. Hayashi, L. Thomas, Y. B. Bazaliy, C. Rettner, R. Moriya, X. Jiang, and S. S. P. Parkin, *Influence of current on field-driven domain wall motion in permalloy nanowires from time resolved measurements of anisotropic magnetoresistance.* Phys. Rev. Lett. **96**, 197207 (2006).
- [108] M. Hayashi, L. Thomas, C. Rettner, R. Moriya, and S. S. P. Parkin, *Direct observation of the coherent precession of magnetic domain walls propagating along permalloy nanowires.* Nat. Phys. **3**, 21 (2007).
- [109] J. Yang, C. Nistor, G. S. D. Beach, and J. L. Erskine, *Magnetic domain-wall velocity oscillations in permalloy nanowires.* Phys. Rev. B **77**, 014413 (2008).
- [110] M. Vázquez, G. A. Basheed, G. Infante, and R. P. Del Real, *Trapping and injecting single domain walls in magnetic wire by local fields.* Phys. Rev. Lett. **108**, 037201 (2012).
- [111] L. Thomas, M. Hayashi, R. Moriya, C. Rettner, and S. Parkin, *Topological repulsion between domain walls in magnetic nanowires leading to the formation of bound states.* Nat. Commun. **3**, 810 (2012).
- [112] I. M. Miron, T. Moore, H. Szambolics, L. D. Buda-Prejbeanu, S. Auffret, B. Rodmacq, S. Pizzini, J. Vogel, M. Bonfim, A. Schuhl, and G. Gaudin, *Fast current-induced domain-wall motion controlled by the rashba effect.* Nat. Mater. **10**, 419 (2011).
- [113] J. H. Franken, M. Hoeijmakers, H. J. M. Swagten, and B. Koopmans, *Tunable resistivity of individual magnetic domain walls.* Phys. Rev. Lett. **108**, 037205 (2012).
- [114] J. Milnor, *Analytic proofs of hairy ball theorem and brouwer fixed-point theorem.* Am. Math. Mon. **85**, 521 (1978).

- [115] R. Streubel, L. Han, M.-Y. Im, F. Kronast, U. K. Rößler, F. Radu, R. Abrudan, G. Lin, O. G. Schmidt, P. Fischer, and D. Makarov, *Manipulating topological states by imprinting non-collinear spin textures*. Sci. Rep. **5**, 8787 (2015).
- [116] K. V. Yershov, V. P. Kravchuk, D. D. Sheka, and Y. Gaididei, *Controllable vortex chirality switching on spherical shells*. J. Appl. Phys. **117**, 083908 (2015).
- [117] M. Albrecht, G. Hu, I. L. Guhr, T. C. Ulbrich, J. Boneberg, P. Leiderer, and G. Schatz, *Magnetic multilayers on nanospheres*. Nat. Mater. **4**, 203 (2005).
- [118] T. C. Ulbrich, D. Makarov, G. Hu, I. L. Guhr, D. Suess, T. Schrefl, and M. Albrecht, *Magnetization reversal in a novel gradient nanomaterial*. Phys. Rev. Lett. **96**, 077202 (2006).
- [119] T. C. Ulbrich, C. Bran, D. Makarov, O. Hellwig, J. D. Risner-Jamtegaard, D. Yaney, H. Rohrmann, V. Neu, and M. Albrecht, *Effect of magnetic coupling on the magnetization reversal in arrays of magnetic nanocaps*. Phys. Rev. B **81**, 054421 (2010).
- [120] C. M. Günther, O. Hellwig, A. Menzel, B. Pfau, F. Radu, D. Makarov, M. Albrecht, A. Goncharov, T. Schrefl, W. F. Schlotter, R. Rick, J. Lüning, and S. Eisebitt, *Microscopic reversal behavior of magnetically capped nanospheres*. Phys. Rev. B **81**, 064411 (2010).
- [121] M. Albrecht and D. Makarov, *Magnetic films on nanoparticle arrays*. Open Surf. Sci. J. **4**, 42 (2012).
- [122] M. V. Sapozhnikov, O. L. Ermolaeva, B. G. Gribkov, I. M. Nefedov, I. R. Karetnikova, S. A. Gusev, V. V. Rogov, B. B. Troitskii, and L. V. Khokhlova, *Frustrated magnetic vortices in hexagonal lattice of magnetic nanocaps*. Phys. Rev. B **85**, 054402 (2012).
- [123] K. Yamada, S. Kasai, Y. Nakatani, K. Kobayashi, H. Kohno, A. Thiaville, and T. Ono, *Electrical switching of the vortex core in a magnetic disk*. Nat. Mater. **6**, 269 (2007).
- [124] B. Pigeau, G. de Loubens, O. Klein, A. Riegler, F. Lochner, G. Schmidt, and L. W. Molenkamp, *Optimal control of vortex-core polarity by resonant microwave pulses*. Nat. Phys. **7**, 26 (2011).

- [125] Y.-S. Yu, H. Jung, K.-S. Lee, P. Fischer, and S.-K. Kim, *Memory-bit selection and recording by rotating fields in vortex-core cross-point architecture*. Appl. Phys. Lett. **98**, 052507 (2011).
- [126] K. Nakano, D. Chiba, N. Ohshima, S. Kasai, T. Sato, Y. Nakatani, K. Sekiguchi, K. Kobayashi, and T. Ono, *All-electrical operation of magnetic vortex core memory cell*. Appl. Phys. Lett. **99**, 262505 (2011).
- [127] D. Mitin, D. Nissen, P. Schädlich, S. S. P. K. Arekapudi, and M. Albrecht, *Single vortex core recording in a magnetic vortex lattice*. J. Appl. Phys. **115**, 063906 (2014).
- [128] L. Baraban, D. Makarov, R. Streubel, I. Mönch, D. Grimm, S. Sanchez, and O. G. Schmidt, *Catalytic janus motors on microfluidic chip: Deterministic motion for targeted cargo delivery*. ACS Nano **6**, 3383 (2012).
- [129] L. Baraban, R. Streubel, D. Makarov, L. Han, D. Karanushenko, O. G. Schmidt, and G. Cuniberti, *Fuel-free locomotion of janus motors: Magnetically induced thermophoresis*. ACS Nano **7**, 1360 (2013).
- [130] E. Bermúdez Ureña, Y. Mei, E. Coric, D. Makarov, M. Albrecht, and O. G. Schmidt, *Fabrication of ferromagnetic rolled-up microtubes for magnetic sensors on fluids*. J. Phys. D: Appl. Phys. **42**, 055001 (2009).
- [131] F. Balhorn, S. Jeni, W. Hansen, D. Heitmann, and S. Mendach, *Axial and azimuthal spin-wave eigenmodes in rolled-up permalloy stripes*. Appl. Phys. Lett. **100**, 222402 (2012).
- [132] R. Streubel, D. Makarov, J. Lee, C. Müller, M. Melzer, R. Schäfer, C. C. Bof Bufon, S.-K. Kim, and O. G. Schmidt, *Rolled-up permalloy nanomembranes with multiple windings*. SPIN **03**, 1340001 (2013).
- [133] R. Streubel, J. Lee, D. Makarov, M.-Y. Im, D. Karanushenko, L. Han, R. Schäfer, P. Fischer, S.-K. Kim, and O. G. Schmidt, *Magnetic microstructure of rolled-up single-layer ferromagnetic nanomembranes*. Adv. Mater. **26**, 316 (2014).
- [134] E. J. Smith, D. Makarov, S. Sanchez, V. M. Fomin, and O. G. Schmidt, *Magnetic microhelix coil structures*. Phys. Rev. Lett. **107**, 097204 (2011).

- [135] J. Zarpellon, H. F. Jurca, J. Varalda, C. Deranlot, J. M. George, M. D. Martins, S. O. Parreiras, C. Müller, and D. H. Mosca, *Magnetic domains in rolled-up nanomembranes of Co/Pt multilayers with perpendicular magnetic anisotropy*. RSC Adv. **4**, 8410 (2014).
- [136] S. Mendach, J. Podbielski, J. Topp, W. Hansen, and D. Heitmann, *Spin-wave confinement in rolled-up ferromagnetic tubes*. Appl. Phys. Lett. **93**, 262501 (2008).
- [137] R. Streubel, L. Han, F. Kronast, A. A. Ünal, O. G. Schmidt, and D. Makarov, *Imaging of buried 3d magnetic rolled-up nanomembranes*. Nano Lett. **14**, 3981 (2014).
- [138] M. Vázquez, *Giant magneto-impedance in soft magnetic wires*. J. Magn. Magn. Mater. **226–230, Part 1**, 693 (2001).
- [139] L. Liu, A. A. Ioannides, and M. Streit, *Single trial analysis of neurophysiological correlates of the recognition of complex objects and facial expressions of emotion*. Brain Topogr. **11**, 291 (1999).
- [140] T. Dumas, S. Dubal, Y. Attal, M. Chupin, R. Jouvent, S. Morel, and N. George, *Meg evidence for dynamic amygdala modulations by gaze and facial emotions*. PLoS ONE **8**, e74145 (2013).
- [141] I. Mönch, D. Makarov, R. Koseva, L. Baraban, D. Karnaushenko, C. Kaiser, K.-F. Arndt, and O. G. Schmidt, *Rolled-up magnetic sensor: Nanomembrane architecture for in-flow detection of magnetic objects*. ACS Nano **5**, 7436 (2011).
- [142] C. Müller, C. C. Bof Bufon, M. E. Navarro-Fuentes, D. Makarov, D. H. Mosca, and O. G. Schmidt, *Towards compact three-dimensional magnetoelectronics—Magnetoresistance in rolled-up Co/Cu nanomembranes*. Appl. Phys. Lett. **100**, 022409 (2012).
- [143] A. C. Kak and M. Slaney, *Principles of computerized tomographic imaging*, Vol. 33 (IEEE Press, 1988).
- [144] J. Radon, *Über die Bestimmung von Funktionen durch ihre Integralwerte längs gewisser Mannigfaltigkeiten*. Ber. Verh. Sächs. Akad. Wiss. **69**, 262 (1917).

- [145] H. Nyquist, *Certain topics in telegraph transmission theory*. Trans. AIEE **47**, 617 (1928).
- [146] S. Kaczmarz, *Angenäherte Auflösung von Systemen linearer Gleichungen*. Bulletin International de l'Academie Polonaise des Sciences et des Lettres **35**, 355 (1937).
- [147] D. J. De Rosier and A. Klug, *Reconstruction of three dimensional structures from electron micrographs*. Nature (London) **217**, 130 (1968).
- [148] P. A. Midgley and R. E. Dunin-Borkowski, *Electron tomography and holography in materials science*. Nat. Mater. **8**, 1476 (2009).
- [149] O. Schärpf, *Theory of magnetic neutron small-angle scattering using the dynamical theory of diffraction instead of the born approximation. i. determination of the scattering angle*. J. Appl. Cryst. **11**, 626 (1978).
- [150] A. Lange, M. P. Hentschel, and A. Kupsch, *Computed tomography reconstructions by DIRECTT-2D model calculations compared to filtered backprojection*. MP Mater. Test. **50**, 272 (2008).
- [151] D. Gabor, *A new microscopic principle*. Nature (London) **161**, 777 (1948).
- [152] H. Lichte, *Electron holography approaching atomic resolution*. Ultramicroscopy **20**, 293 (1986).
- [153] D. Paganin and K. A. Nugent, *Noninterferometric phase imaging with partially coherent light*. Phys. Rev. Lett. **80**, 2586 (1998).
- [154] M. De Graef and Y. Zhu, *Quantitative noninterferometric lorentz microscopy*. J. Appl. Phys. **89**, 7177 (2001).
- [155] S. J. Lade, D. Paganin, and M. J. Morgan, *Electron tomography of electromagnetic fields, potentials and sources*. Opt. Commun. **253**, 392 (2005).
- [156] C. Phatak, M. Beleggia, and M. De Graef, *Vector field electron tomography of magnetic materials: Theoretical development*. Ultramicroscopy **108**, 503 (2008).

- [157] Y. Aharonov and D. Bohm, *Significance of electromagnetic potentials in the quantum theory*. Phys. Rev. **115**, 485 (1959).
- [158] G. Möllenstedt and H. Düker, *Beobachtungen und Messungen an Biprisma-Interferenzen mit Elektronenwellen*. Z. Physik **145**, 377 (1956).
- [159] R. Micheletto, H. Fukuda, and M. Ohtsu, *A simple method for the production of a two-dimensional, ordered array of small latex particles*. Langmuir **11**, 3333 (1995).
- [160] F. Burmeister, C. Schäfle, T. Matthes, M. Böhmisch, J. Boneberg, and P. Leiderer, *Colloid monolayers as versatile lithographic masks*. Langmuir **13**, 2983 (1997).
- [161] C. L. Haynes and R. P. Van Duyne, *Nanosphere lithography: a versatile nanofabrication tool for studies of size-dependent nanoparticle optics*. J. Phys. Chem. **105**, 5599 (2001).
- [162] A. S. Hall, S. A. Friesen, and T. E. Mallouk, *Wafer-scale fabrication of plasmonic crystals from patterned silicon templates prepared by nanosphere lithography*. Nano Lett. **13**, 2623 (2013).
- [163] R. Streubel, F. Kronast, U. K. Rößler, O. G. Schmidt, and D. Makarov, *Reconfigurable large-area magnetic vortex circulation patterns*. Phys. Rev. B **92**, 104431 (2015).
- [164] A. Kosiorek, W. Kandulski, P. Chudzinski, K. Kempa, and M. Giersig, *Shadow nanosphere lithography: Simulation and experiment*. Nano Lett. **4**, 1359 (2004).
- [165] J. Zhang, Y. Li, X. Zhang, and B. Yang, *Colloidal self-assembly meets nanofabrication: From two-dimensional colloidal crystals to nanostructure arrays*. Adv. Mater. **22**, 4249 (2010).
- [166] D. J. Thurmer, C. C. Bof Bufon, C. Deneke, and O. G. Schmidt, *Nanomembrane-based mesoscopic superconducting hybrid junctions*. Nano Lett. **10**, 3704 (2010).
- [167] C. C. Bof Bufon, J. D. A. Espinoza, D. J. Thurmer, M. Bauer, C. Deneke, U. Zschieschang, H. Klauk, and O. G. Schmidt, *Hybrid organic/inorganic molecular heterojunctions based on strained nanomembranes*. Nano Lett. **11**, 3727 (2011).

- [168] E. J. Smith, W. Xi, D. Makarov, I. Mönch, S. Harazim, V. A. Bolaños Quinones, C. K. Schmidt, Y. Mei, S. Sanchez, and O. G. Schmidt, *Lab-in-a-tube: ultracompact components for on-chip capture and detection of individual micro-/nanoorganisms*. Lab Chip **12**, 1917 (2012).
- [169] S. M. Harazim, V. A. Bolanos Quinones, S. Kiravittaya, S. Sanchez, and O. G. Schmidt, *Lab-in-a-tube: on-chip integration of glass optofluidic ring resonators for label-free sensing applications*. Lab Chip **12**, 2649 (2012).
- [170] P. O. Vaccaro, K. Kubota, and T. Aida, *Strain-driven self-positioning of micromachined structures*. Appl. Phys. Lett. **78**, 2852 (2001).
- [171] E. Yablonoitch, T. Gmitter, J. P. Harbison, and R. Bhat, *Extreme selectivity in the lift-off of epitaxial GaAs films*. Appl. Phys. Lett. **51**, 2222 (1987).
- [172] C. Deneke, *Aufgerollte Nanoröhren auf III-V Halbleiterbasis: Herstellung, strukturelle Charakterisierung und mögliche Anwendungen*, Dissertation, University Stuttgart (2005).
- [173] M. Ohring, *Materials sciences of thin films* (Academic Press, 2001).
- [174] C.-Y. You and S.-C. Shin, *Derivation of simplified analytic formulae for magneto-optical kerr effects*. Appl. Phys. Lett. **69**, 1315 (1996).
- [175] G. Traeger, L. Wenzel, and A. Hubert, *Computer experiments on the information depth and the figure of merit in magneto-optics*. physica status solidi (a) **131**, 201 (1992).
- [176] U. Hartmann, *Magnetic force microscopy*. Annu. Rev. Mater. Sci. **29**, 53 (1999).
- [177] C. F. Reiche, S. Vock, V. Neu, L. Schultz, B. Büchner, and T. Mühl, *Bidirectional quantitative force gradient microscopy*. New J. Phys. **17**, 013014 (2015).
- [178] M. R. Scheinfein, J. Unguris, M. H. Kelley, D. T. Pierce, and R. J. Celotta, *Scanning electron microscopy with polarization analysis (sempa)*. Rev. Sci. Instrum. **61**, 2501 (1990).

- [179] T. Duden and E. Bauer, *A compact electron-spin-polarization manipulator*. Rev. Sci. Instrum. **66**, 2861 (1995).
- [180] F. El Gabaly, S. Gallego, C. Muñoz, L. Szunyogh, P. Weinberger, C. Klein, A. K. Schmid, K. F. McCarty, and J. de la Figuera, *Imaging Spin-Reorientation Transitions in Consecutive Atomic Co Layers on Ru(0001)*. Phys. Rev. Lett. **96**, 147202 (2006).
- [181] M. Bode, *Spin-polarized scanning tunnelling microscopy*. Rep. Prog. Phys. **66**, 523 (2003).
- [182] M. Pratzner, H. J. Elmers, M. Bode, O. Pietzsch, A. Kubetzka, and R. Wiesendanger, *Atomic-Scale Magnetic Domain Walls in Quasi-One-Dimensional Fe Nanostripes*. Phys. Rev. Lett. **87**, 127201 (2001).
- [183] S. Heinze, M. Bode, A. Kubetzka, O. Pietzsch, X. Nie, S. Blügel, and R. Wiesendanger, *Real-space imaging of two-dimensional antiferromagnetism on the atomic scale*. Science **288**, 1805 (2000).
- [184] O. Pietzsch, A. Kubetzka, M. Bode, and R. Wiesendanger, *Real-space observation of dipolar antiferromagnetism in magnetic nanowires by spin-polarized scanning tunneling spectroscopy*. Phys. Rev. Lett. **84**, 5212 (2000).
- [185] P. Schattschneider and J. Verbeeck, *Theory of free electron vortices*. Ultramicroscopy **111**, 1461 (2011).
- [186] P. Schattschneider, S. Rubino, C. Hebert, J. Rusz, J. Kunes, P. Novák, E. Carlino, M. Fabrizioli, G. Panaccione, and G. Rossi, *Detection of magnetic circular dichroism using a transmission electron microscope*. Nature (London) **441**, 486 (2006).
- [187] J. Verbeeck, H. Tian, and P. Schattschneider, *Production and application of electron vortex beams*. Nature (London) **467**, 301 (2010).
- [188] A. Beche, R. Van Boxem, G. Van Tendeloo, and J. Verbeeck, *Magnetic monopole field exposed by electrons*. Nat. Phys. **10**, 26 (2014).
- [189] K. Y. Bliokh, P. Schattschneider, J. Verbeeck, and F. Nori, *Electron vortex beams*

in a magnetic field: A new twist on landau levels and aharonov-bohm states. Phys. Rev. X **2**, 041011 (2012).

- [190] J. Stöhr and H. C. Siegmann, *Magnetism: From Fundamentals to Nanoscale Dynamics*, Solid State Sciences, Vol. 75 (Springer, 2006).
- [191] J. Kirz and H. Rarback, *Soft x-ray microscopes.* Rev. Sci. Instrum. **56**, 1 (1985).
- [192] G. Schmahl and D. Rudolph, *Lichtstarke zonenplatten als abbildende systeme für weiche röntgenstrahlung.* Optik **29**, 577 (1969).
- [193] B. Niemann, D. Rudolph, and G. Schmahl, *X-ray microscopy with synchrotron radiation.* Appl. Opt. **15**, 1883 (1976).
- [194] G. Schütz, W. Wagner, W. Wilhelm, P. Kienle, R. Zeller, R. Frahm, and G. Materlik, *Absorption of circularly polarized x rays in iron.* Phys. Rev. Lett. **58**, 737 (1987).
- [195] P. Fischer, G. Schütz, G. Schmahl, P. Guttman, and D. Raasch, *Imaging of magnetic domains with the X-ray microscope at BESSY using X-ray magnetic circular dichroism.* Z. f. Phys. B **101**, 313 (1997).
- [196] P. Fischer, D.-H. Kim, W. Chao, E. H. Liddle, J. Alexander and Anderson, and D. T. Attwood, *Soft x-ray microscopy of nanomagnetism.* Mater. Today **9**, 26 (2006).
- [197] B. P. Tonner and G. R. Harp, *Photoelectron microscopy with synchrotron radiation.* Rev. Sci. Instrum. **59**, 853 (1988).
- [198] F. Nolting, A. Scholl, J. Stohr, J. W. Seo, J. Fompeyrine, H. Siegwart, J.-P. Locquet, S. Anders, J. Luning, E. E. Fullerton, M. F. Toney, M. R. Scheinfein, and H. A. Padmore, *Direct observation of the alignment of ferromagnetic spins by antiferromagnetic spins.* Nature (London) **405**, 767 (2000).
- [199] C. M. Schneider and G. Schönhense, *Investigating surface magnetism by means of photoexcitation electron emission microscopy.* Rep. Prog. Phys. **65**, R1785 (2002).
- [200] F. Kronast, J. Schlichting, F. Radu, S. Mishra, T. Noll, and H. Dürr, *Spin-resolved photoemission microscopy and magnetic imaging in applied magnetic fields.* Surf. Interface Anal. **42**, 1532 (2010).

- [201] S. Eisebitt, J. Luning, W. F. Schlotter, M. Lorgen, O. Hellwig, W. Eberhardt, and J. Stohr, *Lensless imaging of magnetic nanostructures by x-ray spectro-holography*. Nature (London) **432**, 885 (2004).
- [202] H. N. Chapman and K. A. Nugent, *Coherent lensless x-ray imaging*. Nat. Photon. **4**, 833 (2010).
- [203] P. Guttman, C. Bittencourt, S. Rehbein, P. Umek, X. Ke, G. Van Tendeloo, C. P. Ewels, and G. Schneider, *Nanoscale spectroscopy with polarized X-rays by NEXAFS-TXM*. Nat. Photon. **6**, 25 (2012).
- [204] A. McPherson, G. Gibson, H. Jara, U. Johann, T. S. Luk, I. A. McIntyre, K. Boyer, and C. K. Rhodes, *Studies of multiphoton production of vacuum-ultraviolet radiation in the rare gases*. J. Opt. Soc. Am. B **4**, 595 (1987).
- [205] X. F. Li, A. L’Huillier, M. Ferray, L. A. Lompré, and G. Mainfray, *Multiple-harmonic generation in rare gases at high laser intensity*. Phys. Rev. A **39**, 5751 (1989).
- [206] S. Mathias, C. La-O-Vorakiat, P. Grychtol, P. Granitzka, E. Turgut, J. M. Shaw, R. Adam, H. T. Nembach, M. E. Siemens, S. Eich, C. M. Schneider, T. J. Silva, M. Aeschlimann, M. M. Murnane, and H. C. Kapteyn, *Probing the timescale of the exchange interaction in a ferromagnetic alloy*. Proc. Natl. Acad. Sci. USA **109**, 4792 (2012).
- [207] E. Turgut, C. La-o vorakiat, J. M. Shaw, P. Grychtol, H. T. Nembach, D. Rudolf, R. Adam, M. Aeschlimann, C. M. Schneider, T. J. Silva, M. M. Murnane, H. C. Kapteyn, and S. Mathias, *Controlling the competition between optically induced ultrafast spin-flip scattering and spin transport in magnetic multilayers*. Phys. Rev. Lett. **110**, 197201 (2013).
- [208] Lightsources.org, *Light source facility information* (2015).
- [209] C. T. Chen, F. Sette, Y. Ma, and S. Modesti, *Soft-x-ray magnetic circular dichroism at the $l_{2,3}$ edges of nickel*. Phys. Rev. B **42**, 7262 (1990).
- [210] B. T. Thole, P. Carra, F. Sette, and G. van der Laan, *X-ray circular dichroism as a probe of orbital magnetization*. Phys. Rev. Lett. **68**, 1943 (1992).

- [211] P. Carra, B. T. Thole, M. Altarelli, and X. Wang, *X-ray circular dichroism and local magnetic fields*. Phys. Rev. Lett. **70**, 694 (1993).
- [212] J. Stöhr, *X-ray magnetic circular dichroism spectroscopy of transition metal thin films*. J. Elec. Spec. Rel. Phenom. **75**, 253 (1995).
- [213] C. T. Chen, Y. U. Idzerda, H.-J. Lin, N. V. Smith, G. Meigs, E. Chaban, G. H. Ho, E. Pellegrin, and F. Sette, *Experimental confirmation of the x-ray magnetic circular dichroism sum rules for iron and cobalt*. Phys. Rev. Lett. **75**, 152 (1995).
- [214] A. V. Baez, *Fresnel zone plate for optical image formation using extreme ultraviolet and soft x radiation*. J. Opt. Soc. Am. **51**, 405 (1961).
- [215] A. Sakdinawat and Y. Liu, *Soft-x-ray microscopy using spiral zone plates*. Opt. Lett. **32**, 2635 (2007).
- [216] S. Rehbein, S. Heim, P. Guttmann, S. Werner, and G. Schneider, *Ultra-high-resolution soft-x-ray microscopy with zone plates in high orders of diffraction*. Phys. Rev. Lett. **103**, 110801 (2009).
- [217] R. Streubel, P. Fischer, M. Kopte, O. G. Schmidt, and D. Makarov, *Magnetization dynamics of imprinted non-collinear spin textures*. Appl. Phys. Lett. **107**, 112406 (2015).
- [218] J. Stöhr, H. A. Padmore, S. Anders, T. Stammler, and M. R. Scheinfein, *Principles of x-ray magnetic dichroism spectromicroscopy*. Surf. Rev. Lett. **05**, 1297 (1998).
- [219] N. Buckanie, P. Kirschbaum, S. Sindermann, and F.-J. Meyer zu Heringdorf, *Interaction of light and surface plasmon polaritons in Ag islands studied by nonlinear photoemission microscopy*. Ultramicroscopy **130**, 49 (2013).
- [220] L. Gierster, L. Pape, A. A. Ünal, and F. Kronast, *A sample holder with integrated laser optics for an ELMITEC photoemission electron microscope*. Rev. Sci. Instrum. **86**, 023702 (2015).
- [221] T. A. Ostler, J. Barker, R. F. L. Evans, R. W. Chantrell, U. Atxitia, O. Chubykalo-Fesenko, S. El Moussaoui, L. Le Guyader, E. Mengotti, L. J. Heyderman, F. Nolting, A. Tsukamoto, A. Itoh, D. Afanasiev, B. A. Ivanov, A. M. Kalashnikova, K. Vahaplar,

- J. Mentink, A. Kirilyuk, T. Rasing, and A. V. Kimel, *Ultrafast heating as a sufficient stimulus for magnetization reversal in a ferrimagnet*. Nat. Commun. **3**, 666 (2012).
- [222] L. Le Guyader, M. Savoini, S. El Moussaoui, M. Buzzi, A. Tsukamoto, A. Itoh, A. Kirilyuk, T. Rasing, A. V. Kimel, and F. Nolting, *Nanoscale sub-100 picosecond all-optical magnetization switching in GdFeCo microstructures*. Nat. Commun. **6**, 5839 (2015).
- [223] J. Kimling, F. Kronast, S. Martens, T. Böhnert, M. Martens, J. Herrero-Albillos, L. Tati-Bismaths, U. Merkt, K. Nielsch, and G. Meier, *Photoemission electron microscopy of three-dimensional magnetization configurations in core-shell nanostructures*. Phys. Rev. B **84**, 174406 (2011).
- [224] S. Da Col, S. Jamet, N. Rougemaille, A. Locatelli, T. O. Mendes, B. S. Burgos, R. Afid, M. Darques, L. Cagnon, J. C. Toussaint, and O. Fruchart, *Observation of bloch-point domain walls in cylindrical magnetic nanowires*. Phys. Rev. B **89**, 180405 (2014).
- [225] S.-B. Choe, Y. Acremann, A. Schollm, A. Bauer, A. Doran, J. Stöhr, and H. A. Padmore, *Vortex core-driven magnetization dynamics*. Science **304**, 420 (2004).
- [226] M. Donahue and D. Porter, *OOMMF User's Guide, Version 1.0*, Tech. Rep. 6376 (National Institute of Standards and Technology, Gaithersburg, 1999) available at <http://math.nist.gov/oommf/>.
- [227] C. A. Ross, M. Hwang, M. Shima, J. Y. Cheng, M. Farhoud, T. A. Savas, H. I. Smith, W. Schwarzacher, F. M. Ross, M. Redjda, and F. B. Humphrey, *Micromagnetic behavior of electrodeposited cylinder arrays*. Phys. Rev. B **65**, 144417 (2002).
- [228] K. Y. Guslienko, V. Novosad, Y. Otani, H. Shima, and K. Fukamichi, *Magnetization reversal due to vortex nucleation, displacement, and annihilation in submicron ferromagnetic dot arrays*. Phys. Rev. B **65**, 024414 (2001).
- [229] V. Novosad, K. Y. Guslienko, H. Shima, Y. Otani, S. G. Kim, K. Fukamichi, N. Kikuchi, O. Kitakami, and Y. Shimada, *Effect of interdot magnetostatic interaction on magnetization reversal in circular dot arrays*. Phys. Rev. B **65**, 060402 (2002).
- [230] G. Mihajlovic, M. S. Patrick, J. E. Pearson, V. Novosad, S. D. Bader, M. Field, G. J.

- Sullivan, and A. Hoffmann, *Temperature dependent nucleation and annihilation of individual magnetic vortices*. Appl. Phys. Lett. **96**, 112501 (2010).
- [231] K. Maaz, A. Mumtaz, S. K. Hasanain, and M. F. Bertino, *Temperature dependent coercivity and magnetization of nickel ferrite nanoparticles*. J. Magn. Magn. Mater. **322**, 2199 (2010).
- [232] M. P. Sharrock, *Time dependence of switching fields in magnetic recording media (invited)*. J. Appl. Phys. **76**, 6413 (1994).
- [233] P. Gaunt, *Magnetic viscosity and thermal activation energy*. J. Appl. Phys. **59**, 4129 (1986).
- [234] E. P. Wohlfarth, *The coefficient of magnetic viscosity*. J. Phys. F: Met. Phys. **14**, L155 (1984).
- [235] V. Kravchuk, R. Streubel, O. G. Schmidt, P. Fischer, and D. Makarov, *Bessel magnetic vortices in systems with interlayer exchange coupling* (2015), in preparation.
- [236] T. Fischbacher, F. Matteo, G. Bordignon, and H. Fangohr, *A systematic approach to multiphysics extensions of finite-element-based micromagnetic simulations: Nmag*. IEEE Trans. Magn. **43**, 2896 (2007).
- [237] W. Hackbusch, *Hierarchische Matrizen: Algorithmen und Analysis* (Springer, 2009).
- [238] S. Börm, *Efficient Numerical Methods for Non-local Operators: H^2 -Matrix Compression, Algorithms and Analysis*, EMS Tracts in Mathematics, Vol. 14 (European Mathematical Society, 2010).
- [239] Z. Celinski, B. Heinrich, J. F. Cochran, W. B. Muir, A. S. Arrott, and J. Kirschner, *Growth and magnetic studies of lattice expanded Pd in ultrathin Fe(001)/Pd(001)/Fe(001) structures*. Phys. Rev. Lett. **65**, 1156 (1990).
- [240] D. L. R. Santos, P. Venezuela, R. B. Muniz, and A. T. Costa, *Spin pumping and interlayer exchange coupling through palladium*. Phys. Rev. B **88**, 054423 (2013).
- [241] H. Du, W. Ning, M. Tian, and Y. Zhang, *Field-driven evolution of chiral spin textures in a thin helimagnet nanodisk*. Phys. Rev. B **87**, 014401 (2013).

- [242] P. Fischer, M.-Y. Im, S. Kasai, K. Yamada, T. Ono, and A. Thiaville, *X-ray imaging of vortex cores in confined magnetic structures*. Phys. Rev. B **83**, 212402 (2011).
- [243] A. A. Thiele, *Steady-state motion of magnetic domains*. Phys. Rev. Lett. **30**, 230 (1973).
- [244] I. Makhfudz, B. Krüger, and O. Tchernyshyov, *Inertia and chiral edge modes of a skyrmion magnetic bubble*. Phys. Rev. Lett. **109**, 217201 (2012).
- [245] E. Kondorsky, *A mechanism of magnetic hysteresis in heterogeneous alloys*. J. Phys. (Moscow) **II**, 161 (1940).
- [246] F. Schumacher, *On the modification of the kondorsky function*. J. Appl. Phys. **70**, 3184 (1991).
- [247] T. Y. Lee and H. L. Huang, *Remodified kondorsky function and asymmetric wall structure*. J. Appl. Phys. **74**, 495 (1993).
- [248] W. D. Doyle, J. E. Rudisill, and S. Shtrikman, *Angular dependence of torque in anisotropic permalloy films*. J. Appl. Phys. **32**, 1785 (1961).
- [249] X. Fan, Y. S. Gui, A. Wirthmann, G. Williams, D. Xue, and C.-M. Hu, *Electrical detection of microwave assisted magnetization switching in a permalloy microstrip*. Appl. Phys. Lett. **95**, 062511 (2009).
- [250] C. Barbé, J. Bartlett, L. Kong, K. Finnie, H. Lin, M. Larkin, S. Calleja, A. Bush, and G. Calleja, *Silica particles: A novel drug-delivery system*. Adv. Mater. **16**, 1959 (2004).
- [251] D. J. Irvine, *Drug delivery: One nanoparticle, one kill*. Nat. Mater. **10**, 342 (2011).
- [252] A. Jordan, R. Scholz, K. Maier-Hauff, M. Johannsen, P. Wust, J. Nadobny, H. Schirra, H. Schmidt, S. Deger, S. Loening, W. Lanksch, and R. Felix, *Presentation of a new magnetic field therapy system for the treatment of human solid tumors with magnetic fluid hyperthermia*. J. Magn. Magn. Mater. **225**, 118 (2001).
- [253] M. Johannsen, U. Gneveckow, L. Eckelt, A. Feussner, N. WaldÖfner, R. Scholz, S. Deger, P. Wust, S. A. Loening, and A. Jordan, *Clinical hyperthermia of prostate*

cancer using magnetic nanoparticles: Presentation of a new interstitial technique. Int. J. Hyperthermia **21**, 637 (2005).

- [254] L. F. Valadares, Y.-G. Tao, N. S. Zacharia, V. Kitaev, F. Galembeck, R. Kapral, and G. A. Ozin, *Catalytic nanomotors: Self-propelled sphere dimers.* Small **6**, 565 (2010).
- [255] A. A. Solovev, W. Xi, D. H. Gracias, S. M. Harazim, C. Deneke, S. Sanchez, and O. G. Schmidt, *Self-propelled nanotools.* ACS Nano **6**, 1751 (2012).
- [256] W. F. Paxton, K. C. Kistler, C. C. Olmeda, A. Sen, S. K. St. Angelo, Y. Cao, T. E. Mallouk, P. E. Lammert, and V. H. Crespi, *Catalytic nanomotors: autonomous movement of striped nanorods.* J. Am. Chem. Soc. **126**, 13424 (2004).
- [257] R. Dreyfus, J. Baudry, M. L. Roper, M. Fermigier, H. A. Stone, and J. Bibette, *Microscopic artificial swimmers.* Nature (London) **437**, 862 (2005).
- [258] J. R. Howse, R. A. L. Jones, A. J. Ryan, T. Gough, R. Vafabakhsh, and R. Golestanian, *Self-motile colloidal particles: From directed propulsion to random walk.* Phys. Rev. Lett. **99**, 048102 (2007).
- [259] A. A. Solovev, S. Sanchez, M. Pumera, Y. F. Mei, and O. G. Schmidt, *Magnetic control of tubular catalytic microbots for the transport, assembly, and delivery of micro-objects.* Adv. Funct. Mater. **20**, 2430 (2010).
- [260] T. R. Kline, W. F. Paxton, T. E. Mallouk, and A. Sen, *Catalytic nanomotors: Remote-controlled autonomous movement of striped metallic nanorods.* Angew. Chem. Int. Ed. **44**, 744 (2005).
- [261] A. V. Ryzhkova, F. V. Podgornov, and W. Haase, *Nonlinear electrophoretic motion of dielectric microparticles in nematic liquid crystals.* Appl. Phys. Lett. **96**, 151901 (2010).
- [262] G. Loget and A. Kuhn, *Electric field-induced chemical locomotion of conducting objects.* Nat. Commun. **2**, 535 (2011).
- [263] S. J. Ebbens and J. R. Howse, *In pursuit of propulsion at the nanoscale.* Soft Matter **6**, 726 (2010).

- [264] L. Baraban, M. Tasinkevych, M. N. Popescu, S. Sanchez, S. Dietrich, and O. G. Schmidt, *Transport of cargo by catalytic janus micro-motors*. *Soft Matter* **8**, 48 (2012).
- [265] J. Lim, C. Lanni, E. R. Evarts, F. Lanni, R. D. Tilton, and S. A. Majetich, *Magnetophoresis of nanoparticles*. *ACS Nano* **5**, 217 (2011).
- [266] L. W. McKeehan and P. P. Cioffi, *Magnetostriction in permalloy*. *Phys. Rev.* **28**, 146 (1926).
- [267] T. C. Penn and F. G. West, *Magnetostriction and compositional gradients in boat evaporated permalloy films*. *J. Appl. Phys.* **38**, 2060 (1967).
- [268] H. Deng, M. Minor, and J. A. Barnard, *Comparison of mechanical and tribological properties of permalloy and high moment fetan thin films for tape recording heads*. *IEEE Trans. Magn.* **32**, 3702 (1996).
- [269] X. Li, G. Ding, T. Ando, M. Shikida, and K. Sato, *Micromechanical characterization of electroplated permalloy films for mems*. *Microsystem Technologies* **14**, 131 (2008).
- [270] J. Luo, A. Flewitt, S. Spearing, N. Fleck, and W. Milne, *Young's modulus of electroplated ni thin film for MEMS applications*. *Mater. Lett.* **58**, 2306 (2004).
- [271] R. Streubel, D. Köhler, R. Schäfer, and L. M. Eng, *Strain-mediated elastic coupling in magnetoelectric nickel/barium-titanate heterostructures*. *Phys. Rev. B* **87**, 054410 (2013).
- [272] C. Kittel, *Theory of the structure of ferromagnetic domains in films and small particles*. *Phys. Rev.* **70**, 965 (1946).
- [273] T. McGuire and R. Potter, *Anisotropic magnetoresistance in ferromagnetic 3d alloys*. *IEEE Trans. Magn.* **11**, 1018 (1975).
- [274] Persistence of Vision Pty. Ltd., *Persistence of Vision Raytracer v3.7*, <http://povray.org/> (2013).
- [275] J. Lee, D. Makarov, C. Brombacher, B. Dymerska, D. Suess, M. Albrecht, and

- J. Fidler, *Scaling dependence and tailoring of the pinning field in fept-based exchange coupled composite media*. *Nanotechnology* **25**, 045604 (2014).
- [276] J. B. Pendry, *Negative refraction makes a perfect lens*. *Phys. Rev. Lett.* **85**, 3966 (2000).
- [277] J. B. Pendry and S. Anantha Ramakrishna, *Near-field lenses in two dimensions*. *J. Phys. Condens. Matter* **14**, 8463 (2002).
- [278] J. Pendry, *Perfect cylindrical lenses*. *Opt. Express* **11**, 755 (2003).
- [279] Z. Liu, H. Lee, Y. Xiong, C. Sun, and X. Zhang, *Far-field optical hyperlens magnifying sub-diffraction-limited objects*. *Science* **315**, 1686 (2007).
- [280] D. Holzinger, D. Lengemann, F. Göllner, D. Engel, and A. Ehresmann, *Controlled movement of superparamagnetic bead rows for microfluid mixing*. *Appl. Phys. Lett.* **100**, 153504 (2012).
- [281] D. C. Joy, *Handbook of Microscopy*, Vol. 2 (VCH Verlagsgesellschaft Weinheim, 1997).

List of Figures

2.1. Magnetic spin arrangements	6
2.2. Curvature-induced Dzyaloshinskii-Moriya interaction	9
2.3. Magnetochiral effects in nanospheres and nanocaps	11
2.4. Schematics of magnetic spin textures in hemispherical caps	12
2.5. Magnetic cap structures with out-of-plane magnetization	13
2.6. Ultrafast domain wall motion in soft-magnetic cylindrical nanorods	14
2.7. Magnetochiral effects in magnetic nanotubes	15
2.8. Electron holography of soft-magnetic nanorods	16
2.9. Cantilever magnetometry of nanotubes revealing various metastable states	17
2.10. Schematics of magnetic domain patterns in cylindrical surfaces	18
2.11. Schematics of Radon transformation and back projection	19
2.12. Magnetic neutron tomography of macroscopic objects	21
2.13. Electron holography of magnetotactic bacteria	23
2.14. Vector field electron tomography of planar magnetic disks	25
3.1. Structural properties of cap arrays and non-planar honeycomb lattices	28
3.2. Wrinkling and rolling of strained nanomembranes	30
3.3. Down-scaling of rolled-up epitaxial nanomembranes	31
3.4. Fabrication of rolled-up nanomembranes with cylindrical shape	31
3.5. Altering rolling direction due to compensation of strain gradients in hetero- structures	34
4.1. Kerr microscopy on curved magnetic surfaces	38
4.2. Magnetic force microscopy of vortex states in hemispherical caps	39
4.3. X-ray magnetic circular dichroism illustrated at the $L_{2,3}$ edges in Fe metal	42
4.4. Schematics of a transmission X-ray microscope and a X-ray photoemission electron microscope	43

4.5. Stroboscopic relaxation dynamics in non-collinear spin textures visualized with MTXM	44
4.6. Resolving magnetization configuration in core-shell wires with transmission XPEEM	46
4.7. Schematics of contrast origin in transmission XPEEM	47
4.8. Conceptual approach of magnetic X-ray tomography	49
5.1. Shadow contrast and phase diagram of individual hemispherical cap structures	53
5.2. Vortex circulation patterns in closely packed cap arrays	55
5.3. Phase diagram of closely packed soft-magnetic hemispherical caps	57
5.4. Temperature dependence of vortex nucleation and annihilation fields in closely packed caps	60
5.5. Imprint of non-collinear spin textures <i>via</i> interlayer exchange coupling	62
5.6. Experimental observation of imprinted non-collinear spin textures in hemispherical caps	65
5.7. XMCD contrast patterns of donut states with various core sizes	67
5.8. Switching of skyrmion number in imprinted donut states	68
5.9. Angle dependence of magnetic switching fields in cylindrical caps	70
5.10. Magnetic remanent states in soft-magnetic cylindrical caps	71
5.11. Magnetic cap structures as self-propelled micromotors	73
6.1. Magnetic hysteresis loops of planar and rolled-up ferromagnetic nanomembranes	77
6.2. Magnetic domain patterns in magnetostrictive rolled-up nanomembranes	79
6.3. Submicrometer sized magnetic domains in Ni:C rolled-up films	79
6.4. Magnetoresistance of magnetic rolled-up nanomembranes	81
6.5. Magnetization patterns in tightly wound soft-magnetic rolled-up nanomembranes visualized with T-XPEEM	83
6.6. Magnetic domains in loosely wound soft-magnetic rolled-up nanomembranes visualized with T-XPEEM	84
7.1. Angle dependence of 2D projections of circulating magnetization configurations	88
7.2. Modeling 2D projections of azimuthal and helical magnetization textures	89
7.3. Reconstruction of circulating magnetization patterns <i>via</i> correlation with XMCD contrast simulations	90
7.4. Angle dependence of domain widths in XMCD contrast patterns	91

7.5. Magnetic X-ray tomography of radially magnetized tubular architectures	93
7.6. Structural reconstruction of the tubular object using conventional tomography	94
7.7. 3D reconstruction of magnetization texture	96
7.8. Angle dependence of radial domain patterns	98
A.1. Manipulating and transferring cylindrical objects inside a cross-beam work- station	107

List of Tables

3.1. Structural parameters of rolled-up nanomembranes consisting of strained GaAs/InGaAs bilayers	32
3.2. Structural parameters of rolled-up nanomembranes consisting of strained nickel films	33
5.1. Fitting parameters for vortex nucleation and annihilation fields in closely packed caps	60

Acknowledgements

Within the last years, many people have contributed to my thesis, who I would like to acknowledge in the following. Without their support I would have never succeeded in my work.

Prof. Oliver G. Schmidt (IFW Dresden, TU Chemnitz), who offered me a Ph.D. position and provided me access to the facilities at the IFW Dresden.

Dr. Denys Makarov (IFW Dresden) for fruitful discussions on current and future projects, advice in scientific cases and financial support to carry out allocated beam times.

Dr. Peter Fischer (CXRO at LBNL, UC Santa Cruz) for granting me access to his beam line, support and discussions as well as promotion of our mutual research topics.

Dr. Florian Kronast (BESSY II at HZB), who persistently improved his beam line to make it even more user friendly.

Dr. Luyang Han (IFW Dresden) for fruitful discussions and assistance in micromagnetic simulations.

Dr. Dominic J. Thurmer (IFW Dresden), who introduced me to SEM and FIB as well as epitaxially strained semiconductor bilayer systems.

Dr. Ulrich K. Rößler (IFW Dresden) for sharing his enormous theoretical knowledge on non-collinear spin textures.

Dr. Volodymyr P. Kravchuk (BITP Kiev) and Dr. Denis D. Sheka (TS National University of Kiev) for contributions in the analytical treatment of soft-magnetic vortices and micromagnetic simulations.

Dr. Joshua Deutsch (UC Santa Cruz), who joined our research activities to further develop MXT.

Dr. Rudolf Schäfer (IFW Dresden) for granting me access to his Kerr microscopes.

Dr. J. Ingolf Mönch (IFW Dresden), who shared his profound experience with lithography

and etching techniques with me.

Dr. Larysa Baraban (TU Dresden), who gave me an excursion to the biology-inspired side of science.

Dr. Stefan Harazim and Sebastian Seifert (both IFW Dresden) for their support and continuously improving the clean room facility at the IFW Dresden.

Dr. Thomas Mühl and Christopher F. Reiche (both IFW Dresden) for their assistance with the MFM.

Cornelia Krien and Irina Fiering (IFW Dresden), who kindly sputter-deposited samples on demand.

Ronny Engelhard and Rainer Kaltofen (both IFW Dresden) for their technical engagement.

Dr. Anja Wolter-Giraud (IFW Dresden), who provided me access to the SQUID-VSM.

Dr. Mi-Young Im (CXRO at LBNL), Dr. Sergio Valencia and Dr. Ahmet A. Ünal (both BESSY II at HZB) for assistance and interesting discussions during beam times.

Gungun Lin, Daniil Karnaushenko, Michael Melzer, Tobias Kosub and Martin Kopte (all IFW Dresden) for assistance and fruitful discussion on challenges emerging during daily work.

Thanks to all other members of the IIN at the IFW Dresden, who were interested in my topics.

Erklärung

Hiermit versichere ich, dass ich die vorliegende Arbeit ohne unzulässige Hilfe Dritter und ohne Benutzung anderer als der angegebenen Hilfsmittel angefertigt habe. Bestehend aus hauptsächlich bereits veröffentlichten beziehungsweise sich im Veröffentlichungsprozess befindlichen Arbeiten, berücksichtigt sie Verbesserungsvorschläge jeweiliger Koautoren. Die aus fremden Quellen direkt oder indirekt übernommenen Gedanken sind als solche kenntlich gemacht. Die Arbeit wurde bisher weder im Inland noch im Ausland in gleicher oder ähnlicher Form einer anderen Prüfungsbehörde vorgelegt.

Robert Streubel

Chemnitz, 8.5.2015

Curriculum Vitae

Personal Information

Name Robert Streubel
Day of birth 05.10.1987
Place of birth Dippoldiswalde, Germany

Education

since 1.8.2011	Ph.D. student	Institute for Integrative Nanosciences, IFW Dresden Topic: Imaging Spin Textures on Curved Magnetic Surfaces
14.6.2011	Diplom-Physiker	Institute of Applied Physics, TU Dresden Topic: Strain-Mediated Coupling in Magnetoelectric Composite Materials (Final degree 1.2) Supervisor: Prof. Dr. Lukas M. Eng
2006	Abitur	Sächsisches Landesgymnasium St. Afra zu Meißen

Research Activities

since 1.8.2011	PhD student	Institute for Integrative Nanosciences, IFW Dresden
2010 – 2011	Graduate student	Institute of Applied Physics, TU Dresden
2011	Research assistant	Institute for Integrative Nanosciences, IFW Dresden
2009	Research assistant	Institute of Applied Physics, TU Dresden
2008	Research assistant	Helmholtzzentrum Dresden-Rossendorf

Publications

Journal Articles

2015

15. Robert Streubel, Florian Kronast, Peter Fischer, Dula Parkinson, Oliver G. Schmidt, and Denys Makarov: *Retrieving spin textures on curved magnetic thin films with full-field soft X-ray microscopies*, Nat. Commun. 6, 7612 (2015).
14. Robert Streubel, Luyang Han, Mi-Young Im, Florian Kronast, Ulrich K. Rößler, Florin Radu, Radu Abrudan, Gungun Lin, Oliver G. Schmidt, Peter Fischer, and Denys Makarov: *Manipulating Topological States by Imprinting Non-Collinear Spin Textures*, Sci. Rep. 5, 8787 (2015).
13. Robert Streubel, Peter Fischer, Martin Kopte, Oliver G. Schmidt, and Denys Makarov: *Magnetization Dynamics of Imprinted Non-collinear Spin Textures*, Appl. Phys. Lett. 107, 112406 (2015).
12. Robert Streubel, Florian Kronast, Ulrich K. Rößler, Oliver G. Schmidt, and Denys Makarov: *Reconfigurable Large-Area Magnetic Vortex Circulation Patterns*, Phys. Rev. B 92, 104431 (2015).

2014

11. Robert Streubel, Jehyun Lee, Denys Makarov, Mi-Young Im, Daniil Karnaushenko, Luyang Han, Rudolf Schäfer, Peter Fischer, Sang-Koog Kim, and Oliver G. Schmidt: *Magnetic microstructure of rolled-up single-layer ferromagnetic nanomembranes*, Adv. Mater. 26, 316 (2014).
10. Robert Streubel, Luyang Han, Florian Kronast, Ahmet A. Ünal, Oliver G. Schmidt,

and Denys Makarov: *Imaging of Buried 3D Magnetic Rolled-up Nanomembranes*, Nano Lett. 14, 3981 (2014).

2013

9. Robert Streubel, Denny Köhler, Rudolf Schäfer, and Lukas M. Eng: *Strain-mediated elastic coupling in magnetoelectric nickel/barium-titanate heterostructures*, Phys. Rev. B 87, 054410 (2013).
8. Robert Streubel, Denys Makarov, Jehyun Lee, Christian Müller, Michael Melzer, Schäfer Rudolf, Carlos Cesar Bof Bufon, Sang-Koog Kim, and Oliver G. Schmidt: *Rolled-up permalloy nanomembranes with multiple windings*, SPIN 03, 1340001 (2013).
7. Larysa Baraban, Robert Streubel, Denys Makarov, Luyang Han, Dmitriy Karnauschenko, Oliver G. Schmidt, and Gianaurelio Cuniberti: *Fuel-free locomotion of janus motors: Magnetically induced thermophoresis*, ACS Nano 7, 1360 (2013).

2012

6. Robert Streubel, Dominic J. Thurmer, Denys Makarov, Florian Kronast, Tobias Kosub, Volodymyr Kravchuk, Denis D. Sheka, Yuri Gaididei, Rudolf Schäfer, and Oliver G. Schmidt: *Magnetically capped rolled-up nanomembranes*, Nano Lett. 12, 3961 (2012).
5. Robert Streubel, Volodymyr P. Kravchuk, Denis D. Sheka, Denys Makarov, Florian Kronast, Oliver G. Schmidt, and Yuri Gaididei: *Equilibrium magnetic states in individual hemispherical permalloy caps*, Appl. Phys. Lett. 101, 132419 (2012).
4. Robert Streubel, Denys Makarov, Florian Kronast, Volodymyr Kravchuk, Manfred Albrecht, and Oliver G. Schmidt: *Magnetic vortices on closely packed spherically curved surfaces*, Phys. Rev. B 85, 174429 (2012).
3. Larysa Baraban, Denys Makarov, Robert Streubel, Ingolf Mönch, Daniel Grimm, Samuel Sanchez, and Oliver G. Schmidt: *Catalytic janus motors on microfluidic chip: Deterministic motion for targeted cargo delivery*, ACS Nano 6, 3383 (2012).
2. Daniil Karnauschenko, Denys Makarov, Chenglin Yan, Robert Streubel, and Oliver G. Schmidt: *Printable giant magnetoresistive devices*, Adv. Mater. 24, 4518 (2012).

1. Volodymyr P. Kravchuk, Denis D. Sheka, Robert Streubel, Denys Makarov, Oliver G. Schmidt, and Yuri Gaididei: *Out-of-surface vortices in spherical shells*, Phys. Rev. B 85, 144433 (2012).

Invited Conference Talks

4. Robert Streubel: *Imaging Spin Textures on Curved Magnetic Surfaces*, Joint BER II and BESSY II User Meeting, Berlin, Germany, 9.12. – 11.12.2015.
3. Robert Streubel, and Denys Makarov: *Curved Magnetic Nanomembranes*, International Magnetism Conference (Intermag), Beijing, China, 11.5. – 15.5.2015.
2. Robert Streubel: *Controlling Topological Charges by Imprinting Non-Collinear Spin Textures*, Conference on Magnetism and Magnetic Materials (MMM), Honolulu, USA, 3.11. – 7.11.2014.
1. Robert Streubel: *Magnetism on Curved Surfaces*, Joint European Magnetic Symposia (JEMS) 2012, Parma, Italy, 9.9. – 14.9.2012.

Invited Seminar Talks

3. Robert Streubel: *Imaging Spin Textures on Curved Magnetic Surfaces*, Helmholtz-Zentrum Dresden-Rossendorf, Dresden, Germany, 18.06.2015.
2. Robert Streubel: *Towards Magnetic X-ray Tomography*, University of California, Santa Cruz, USA, 14.11.2014.
1. Robert Streubel: *Imaging 3D Spin Textures in Non-planar Architectures*, University of California, Berkeley, USA, 12.8.2014.

Contributed Conference Talks

2015

14. Robert Streubel, Florian Kronast, Ulrich K. Rößler, Oliver G. Schmidt, Peter Fisc-

her, and Denys Makarov: *Imprinting magnetic chiral spin textures*, International Conference on Magnetism (ICM), Barcelona, Spain, 6.7. – 10.7.2015.

13. Robert Streubel, Florian Kronast, Peter Fischer, Oliver G. Schmidt, and Denys Makarov: *Imaging magnetic domain patterns in 3D curved surfaces*, International Conference on Magnetism (ICM), Barcelona, Spain, 6.7. – 10.7.2015.
12. Robert Streubel, Nicolas Perez, Denys Makarov, Daniel T. Pierce, John Unguris, Stefan Pofahl, Rudolf Schäfer, Marcus Schmidt, Michael Baenitz, Florian Kronast, Heribert Wilhelm, and Ulrich K. Rößler: *Surface magnetic order and static defect structure in FeGe*, DMI 2015, Pskov, Russia, 26.5. – 30.5.2015.
11. Robert Streubel, Florian Kronast, Ulrich K. Rößler, Oliver G. Schmidt, Peter Fischer, and Denys Makarov: *Magnetic Chiral Spin Textures by Imprinting*, International Magnetism Conference (Intermag), Beijing, China, 11.5. – 15.5.2015.
10. Robert Streubel, Florian Kronast, Peter Fischer, Oliver G. Schmidt, and Denys Makarov: *Magnetic Soft X-ray Tomography of Magnetic Swiss Roll Architectures*, International Magnetism Conference (Intermag), Beijing, China, 11.5. – 15.5.2015.
9. Robert Streubel, Denys Makarov, Michael Melzer, Daniil Karnaushenko, Gungun Lin, Ingolf J. Mönch, and Oliver G. Schmidt: *Shapeable Magnetic Sensorics*, International Magnetism Conference (Intermag), Beijing, China, 11.5. – 15.5.2015.

2014

8. Robert Streubel, Florian Kronast, Peter Fischer, Oliver G. Schmidt, and Denys Makarov: *Towards Magnetic X-ray Computed Tomography*, Conference on Magnetism and Magnetic Materials (MMM), Honolulu, USA, 3.11. – 7.11.2014.
7. Robert Streubel, Luyang Han, Florian Kronast, Dula Parkinson, Mi-Young Im, Peter Fischer, Rudolf Schäfer, Oliver G. Schmidt, and Denys Makarov: *Imaging of 3D Magnetic Architectures*, International Magnetism Conference (Intermag), Dresden, Germany, 4.5. – 8.5.2014.
6. Robert Streubel, Luyang Han, Mi-Young Im, Florin Radu, Radu Abrudan, Ulrich K. Rößler, Oliver G. Schmidt, Peter Fischer, and Denys Makarov: *Imprinting Non-Collinear Chiral Spin Textures*, International Magnetism Conference (Intermag),

Dresden, Germany, 4.5. – 8.5.2014.

5. Robert Streubel, Denys Makarov, Peter Fischer, Rudolf Schäfer, and Oliver G. Schmidt: *Magnetic Domains in Rolled-Up Ferromagnetic Single-Layer Nanomembranes and Magnetically Capped Tubular Architectures*, DPG Spring Meeting, Dresden, Germany, 30.3. – 4.4.2014.

2013

4. Robert Streubel, Luyang Han, Daniil Karnaushenko, Rudolf Schäfer, Ulrich K. Rößler, Mi-Young Im, Oliver G. Schmidt, Peter Fischer, and Denys Makarov: *Magnetism on curved surfaces*, ALS User Meeting, Berkeley, USA, 7.10. – 9.10.2013.
3. Robert Streubel, Denys Makarov, Florian Kronast, and Oliver G. Schmidt: *Magnetic vortices in non-planar architectures*, 526. Heraeus seminar, Bad Honnef, Germany, 4.3. – 6.3.2013.

2012

2. Robert Streubel, Denys Makarov, Florian Kronast, and Oliver G. Schmidt: *Magnetism on Curved Surfaces*, DPG Spring Meeting, Berlin, Germany, 25.3. – 30.3.2012.

2011

1. Robert Streubel, Denny Köhler, Oliver Mieth, Rudolf Schäfer, Anja Wolter, Rudolf Groß, and Lukas M. Eng: *Strain-mediated Coupling in Magnetoelectric Heterostructures*, DPG Spring Meeting, Dresden, Germany, 13.3. – 18.3.2011.

Patent Application

- Robert Streubel, Denys Makarov, Larysa Baraban, Gianauelio Cuniberti, and Oliver G. Schmidt: *Magnetically capped objects for self-propulsive target drug delivery driven by thermophoresis*.